NOVA SCHOOL OF SCIENCE & TECHNOLOGY

DEPARTAMENT OF CHEMISTRY

TYRE4REECYCLE

RECOVERY OF RARE EARTH ELEMENTS FROM NDFEB MAGNETS BY USING POROUS CARBONS PRODUCED FROM RUBBER OF SPENT TYRES

MIGUEL FILIPE DA COSTA NOGUEIRA

Master in Renewable Energy Engineering

DOCTORATE IN SUSTAINABLE CHEMISTRY

NOVA University Lisbon

October, 2024

DEPARTAMENT OF
CHEMISTRY

TYRE4REECYCLE

RECOVERY OF RARE EARTH ELEMENTS FROM NDFEB MAGNETS BY USING POROUS CARBONS PRODUCED FROM RUBBER OF SPENT TYRES

MIGUEL FILIPE DA COSTA NOGUEIRA

Master in Renewable Energy Engineering

Adviser: Nuno Carlos Lapa dos Santos Nunes
Assistant Professor, NOVA School of Science and Technology, NOVA University Lisbon

Co-advisers: Inês Alexandra Morgado do Nascimento Matos
Principal Investigator, NOVA School of Science and Technology, NOVA University Lisbon

Maria Filomena de Jesus Pinto
Principal Investigator, LNEG – National Laboratory of Energy and Geology

Examination Committee:

Chair: Ana Isabel Nobre Martins Aguiar de Oliveira Ricardo
Full Professor, NOVA School of Science and Technology, NOVA University Lisbon

Rapporteurs: Margarida Maria João de Quina
Associate Professor with Aggregation, Faculty of Science and Technology, University of Coimbra

José Eduardo dos Santos Félix Castanheiro
Associate Professor with Aggregation, School of Science and Technology, University of Évora

Adviser: Inês Alexandra Morgado do Nascimento Matos
Principal Investigator, NOVA School of Science and Technology, NOVA University Lisbon

Members: Isabel Maria de Figueiredo Ligeiro da Fonseca
Retired Associate Professor, NOVA School of Science and Technology, NOVA University Lisbon

Maria Eduarda da Cunha Pereira
Associate Professor, University of Aveiro

Ana Isabel Nobre Martins Aguiar de Oliveira Ricardo
Full Professor, NOVA School of Science and Technology, NOVA University Lisbon

DOCTORATE IN SUSTAINABLE CHEMISTRY

NOVA University Lisbon
October, 2024

Tyre4REEcyle
Recovery of Rare Earth Elements from NdFeB Magnets by Using Porous Carbons Produced from Rubber of Spent Tyres

Para os meus Avós,

Para o Durão

ACKNOWLEDGMENTS

I would like to thank the Fundação para a Ciência e Tecnologia (**FCT**) for funding my Ph.D. fellowship (doi.org/10.54499/SFRH/BD/147601/2019), and **LAQV/REQUIMTE** for providing the resources and facilities that enabled the development of my project. A special thanks to **ValorPneu** for supporting my project and financing this work (RObUST-Valorpneu-FCT_NOVA/23-24 and the Inov.Ação 2019 Award).

A very special thanks to **Professor Doctor Nuno Lapa**, my supervisor, for giving me this opportunity, for his patience in dealing with me, for all the knowledge and wisdom he has shared, and for guiding me throughout this journey.

To **Doctor Inês Matos**, my co-supervisor, for all her assistance, brainstorming, teachings, debates, and for leading me throughout this Ph.D.

To **Doctor Filomena Pinto**, my co-supervisor, for the production of the chars, the use of LNEG's equipment, and for her constant availability and support.

To **Professor Doctor Ana Aguiar Ricardo**, for enabling me to enroll in the Doctoral Program in Sustainable Chemistry (PDQS), and for always being available to support me whenever needed.

To **Professor Doctor Isabel Fonseca**, for allowing me to use her laboratories and equipment, for her valuable knowledge, insights, ideas, and for her support.

To **Doctor Maria Bernardo**, my informal honorary co-supervisor, for all her help, guidance during lab work, deep expertise in adsorption and chars, brainstorming sessions, and conversations.

To **Doctor Márcia Ventura**, for her support, debates, knowledge, and our valuable discussions.

To **Professor Doctor João Carlos Lima**, for providing me access to the photochemistry labs and all the required equipment for the photocatalysis assays, and his expertise and input.

To **Doctor Sandra Gago**, for helping to idealise the photocatalysis assays, for guiding and teaching me during the lab work, for the reviews, for her knowhow, and for helping me explore a very interesting part of this thesis.

To **Professor Doctor Luís Tarelho** for the usage of the semi-continuous pyrolysis reactor and the installations at Universidade de Aveiro, and for his expertise and inputs.

To the lab technicians, **Carla Rodrigues** and **Nuno Costa**, for all their help, analyses, discussions, and for sharing their expertise in the techniques I used throughout this work.

To the assistant technicians, **Dona Palminha**, **Dona Idalina**, **Dona Rita**, and **Dona Rosa**, for all their support in the lab.

To all the **PDQS teachers**, for their support and the knowledge they provided.

To all my Ph.D. colleagues, for their friendship and camaraderie.

To my **friends** (GT, B3K, Centurion), for being always present, for the many laughs and great banter.

To my **parents**, for their emotional, spiritual, and financial support throughout this journey, and for shaping me into the person I am today.

To my brothers, **Hugo**, **Pedro**, and **Paulo**, with a special thanks to **João**, for being my best friend, always being there for me, and helping me unwind when things were tough.

To my grandparents, for instilling in me the drive to pursue my dreams, to dream big, to believe in myself, and to always strive to improve both myself and those around me.

And finally, to **Carolina**, who has been my rock, always supporting my decisions, providing much-needed stability in my life, picking me up when I was feeling down, being a constant source of happiness, and most importantly, for all the love she has given me. You make me look forward to coming back to our home every day.

ABSTRACT

This thesis explores the recovery of rare earth elements, specifically Neodymium and Dysprosium, from NdFeB magnets through adsorption using porous carbon materials derived from spent tyre rubber. The increasing disposal of end-of-life tyres and the scarcity of rare earth elements in technological applications present significant environmental and economic challenges. By utilizing tyre pyrolysis, this research converts waste into valuable porous carbons that serve as effective adsorbents for rare earth elements recovery.

Porous carbons were produced via pyrolysis of spent tyre rubber, followed by physical activation of the resulting chars. These materials were characterized and tested for their adsorption capacity toward rare earth elements under both batch and dynamic conditions. Single-component and competitive adsorption studies were conducted to evaluate the interactions between Neodymium and Dysprosium ions. In addition, real magnet leachates were utilized to simulate real-world applications of these materials. The findings revealed substantial adsorption capacities for both rare earth elements, with physically activated chars exhibiting superior performance, attributable to their enhanced properties. Beyond rare earth elements recovery, the rare earth-loaded porous carbons were assessed for their catalytic activity in photocatalytic hydrogen production. The successful incorporation of rare earth elements and porous carbons derived from spent tyre rubber as catalysts in hydrogen evolution further closed the waste valorisation loop, demonstrating the dual functionality of the materials.

This thesis provides a novel approach to the circular economy by addressing two waste streams - spent tyre rubber and electronic waste - while developing sustainable materials for critical raw material recovery. The findings highlight the potential of this process for industrial applications and contribute to the advancement of green chemistry and sustainable engineering in resource recovery.

Keywords: Rare Earth Elements; Spent Tyre Rubber; E-Waste; Adsorption; Photocatalysis

RESUMO

Esta tese explora a recuperação de elementos de terras raras, especificamente neodímio e disprósio, a partir de magnetos NdFeB através da adsorção utilizando materiais de carbono poroso derivados de borracha de pneus usados. A crescente quantidade de pneus em fim de vida e a escassez de elementos de terras raras disponíveis para aplicações tecnológicas representam desafios ambientais e económicos significativos. Ao utilizar a pirólise de pneus, esta investigação converte os resíduos em materiais de carbono porosos que servem como adsorventes para a recuperação de elementos de terras raras.

Os materiais de carbono porosos foram produzidos através da pirólise de borracha de pneus usados, seguida da ativação física dos materiais resultantes. Estes materiais foram caracterizados e testados quanto à sua capacidade de adsorção de terras raras em condições dinâmicas e em batch. Foram realizados estudos de adsorção mono-componente e de adsorção competitiva de forma a avaliar as interações entre os iões de neodímio e disprósio. Posteriormente, foram utilizados lixiviados de ímanes reais para simular aplicações reais destes materiais. Os resultados revelaram capacidades de adsorção substanciais para ambas as terras raras, com os carvões ativados a exibirem um desempenho superior. Além da recuperação de terras raras, os carvões porosos carregados com terras raras foram avaliados quanto à sua atividade catalítica para a produção de hidrogénio. A incorporação de terras raras e de carbonos porosos derivados da borracha de pneus como catalisadores em reações de evolução de hidrogénio fecha o ciclo de valorização dos resíduos, demonstrando a dupla funcionalidade dos materiais.

Esta tese fornece uma abordagem nova à economia circular, tratando dois fluxos de resíduos - borracha de pneus usada e resíduos eletrónicos - ao mesmo tempo que desenvolve materiais sustentáveis para a recuperação de matérias-primas críticas. Os resultados destacam o potencial deste processo para aplicações industriais e contribuem para o avanço da química verde e da engenharia sustentável na recuperação de recursos.

Palavras chave: Elementos de Terras Raras; Borracha de Pneus Usados; Resíduos Eletrónicos; Adsorção; Fotocatálise

CONTENTS

LIST OF FIGURES

LIST OF TABLES

ACRONYMS

AC	Activated Carbon
BET	Brunauer–Emmett–Teller
CAC	Commercial Activated Carbon
CHNS	Carbon Hydrogen Nitrogen Sulfur
CNT	Carbon Nano-Tube
CRM	Critical Raw Material
DGO	Diglycolylester
EDS	Energy Dispersive X-Ray Spectroscopy
EDTA	Ethylenediaminetetraacetic Acid
EoL	End-of-Life
EU	European Union
FCT	Faculdade De Ciências E Tecnologia
FCT	Fundação para a Ciência e a Tecnologia
FTIR	Fourier Transform Infrared Spectroscopy
GC	Gas Chromatography
GHG	Green House Gas
GO	Graphene Oxide
HDD	Hard-Disk Drive
ICP-AES	Inductively Coupled Plasma Atomic Emission Spectroscopy
IUPAC	International Union of Pure and Applied Chemistry
LAQV	Laboratório Associado para a Química Verde
LCA	Life-Cycle Assessment
LED	Light-Emitting Diode
MCE	Mixed Cellulose Esters
MS	Mass Spectrometry
NMR	Nuclear Magnetic Resonance
PAM	Polyacrylamide

PAN	Polyacrylonitrile
PC	Porous Carbon
PFO	Pseudo-First-Order
pH_{PZC}	pH at Point of Zero Charge
PSD	Particle Size Distribution
PSO	Pseudo-Second-Order
PVC	Polyvinyl Chloride
REE	Rare Earth Element
SEM	Scanning Electron Microscopy
STR	Spent Tyre Rubber
TCD	Thermal Conductivity Detector
TGA	Thermo-Gravimetric Analysis
UK	United Kingdom
USA	United States of America
WEEE	Waste from Electrical and Electronic Equipment
XPS	X-Ray Photoelectron Spectroscopy
XRPD	X-Ray Powder Diffraction

SYMBOLS

A405	Char from Rubber A pyrolyzed at 405 °C
A405CO2	Activated carbon from A405 with CO2
A450	Char from Rubber A pyrolyzed at 450 °C
A900	Char from Rubber A pyrolyzed at 900 °C
A900Dy	Char A900 after Dy adsorption
A900Nd	Char A900 after Nd adsorption
A_{BET}	Brunauer–Emmett–Teller (BET) surface area measurement
B405	Char from Rubber B pyrolyzed at 405 °C
B405CO2	Activated carbon from B405 with CO2
B450	Char from Rubber B pyrolyzed at 450 °C
B900	Char from Rubber B pyrolyzed at 900 °C
C_0	Initial concentration
Ce	Cerium
CH_4	Methane
CO	Carbon Monoxide
CO_2	Carbon Dioxide
COO	Carboxylate group
COOH	Carboxyl group
Dy	Dysprosium
Er	Erbium
Eu	Europium
Gd	Gadolinium
H	Hydrogen (element)
H_2	Hydrogen (gas)
H_2O	Water
H_2O_2	Hydrogen peroxide
H_2S	Hydrogen sulphide
H_2SO_4	Sulfuric acid

H_3BO_3	Boric acid
H_3PO_4	Phosphoric acid
HF	Hydrofluoric acid
HNO_3	Nitric acid
Ho	Holmium
K	Potassium (element)
K_2CO_3	Potassium carbonate
K_F	Freundlich constant
K_L	Langmuir constant
$KMnO_4$	Potassium permanganate
KOH	Potassium hydroxide
La	Lanthanum
Lu	Lutetium
MJ	Megajoule
N_2	Nitrogen (gas)
Nd	Neodymium
NdFeB	Neodymium-Iron-Boron (magnet)
NH_3	Ammonia
NO	Nitric oxide
NO_2	Nitrogen dioxide
NO_3	Nitrate ion
O	Oxygen (element)
O_2	Oxygen (gas)
O_3	Ozone
OH	Hydroxyl group or hydroxide ion
P	Phosphorus (element)
Pm	Promethium
Pr	Praseodymium
R^2	Coefficient of determination
S_{BET}	Specific surface area measured by BET method
Sc	Scandium
SI	Silicon
Sm	Samarium
SO	Sulfur monoxide
SO_4^{2-}	Sulphate ion
Tb	Terbium
Tm	Thulium
WO_4^{2-}	Tungstate ion
Y	Yttrium

Yb Ytterbium

1

INTRODUCTION

1.1 Background and motivation

The disposal of spent tyres (ST) represents a major environmental threat worldwide. Valorpneu (Portuguese Company of the Integrated Management System for Used Tyres) reported that in 2021, 93 234 tons [1] of tyres were disposed of in Portugal, while in Europe this value reached 3.4 million tons. High percentages (25,2% in Portugal [1]) of these wastes are sent for energetic valorisation (combustion), which implies the loss of material, as well as the emission of toxic compounds and Greenhouse Gases (GHG). In this context, ST recycling must be strengthened with new technological solutions. Pyrolysis (also known as chemical recycling) demonstrates to be a viable route for ST valorisation, as it effectively converts wastes into high added-value products, such as liquid products that may be used as fuels or as raw materials, and porous carbon (PC) materials that can be used in different industries [2–4].

Among the many applications of PC, their unique properties make them highly efficient as adsorbents and catalysts support for synthesizing valuable compounds [5–7]. Recognizing this problem, Valorpneu decided to create the "INOV.AÇÃO" award, whose primary objective was to stimulate the efficient use of resources and the concept of circular economy around the topic of management and sustainable destination of used tyres. The supervision team of this Ph.D. work plan won this award in 2018 with the project entitled "RObUST – Economia Circular Aplicada à Borracha de Pneus: Valorização Material, Química e Energética".

Wastes of electric and electronic equipment (WEEE) are a rising problem in technological societies. The current recycling pathways are characterised by technological difficulties and economic constraints. Nevertheless, they are a source of rare earth elements

(REEs), which are critical raw materials for technological industry in Europe and worldwide [8]. REEs show excellent physical and chemical properties, playing an important role in today's technologies. REEs are present in permanent magnets, phosphors, batteries, catalysts, alloys, electric engines, generators, and wind turbines [9–12].

This Ph.D. thesis aimed:

(i) To produce optimized porous carbons from the rubber of ST;
(ii) To recover and recycle two REEs (Neodymium (Nd) and Dysprosium (Dy)) from the permanent magnets of computers' hard drives. This Ph.D. thesis included a proof-of-concept in which the (a) porous carbons were used in the recovery of Nd/Dy from magnets and (b) catalytic porous carbons were used in photocatalytic reactions.

The current literature review indicates that ST rubber is an adequate feedstock to produce chars through pyrolysis [13–17]. Literature also suggests that these chars are valid precursors for high-value activated carbons (AC) [2–4], under a wide range of activation conditions.

Adsorption of Nd and Dy trivalent ions is scarcely reported in the literature. Specifically, adsorption studies of these metals onto porous carbon materials are even rarer with only a few available papers [12,18–21]. Concerning the competitive adsorption, as well as the dynamic adsorption of these metals, there are even fewer reports [22]. This is one of the major innovative aspects of the present Ph.D. thesis.

The full cycle became complete with the proof-of-concept, which was tested through the (i) recovery of the REEs from EoL NdFeB (neodymium-iron-boron) magnet leachates and (ii) application of the carbon materials enriched with Nd as catalysts in the photocatalytic production of H_2.

1.2 Research objectives

This Ph.D. thesis had two major objectives:

a) The valorisation of spent tyre rubber through the production of high-value and high-efficiency porous carbons.
b) The recovery of REEs (Nd and Dy) from end-of-life (EoL) electronic waste.

The production of porous carbons enabled a new pathway for the valorisation of spent tyre rubber, which will promote tyre recycling in the context of the Circular Economy where new products for innovative applications will be produced. On the other hand, electronic

wastes currently have no viable large-scale recycling and/or valorisation routes, as such, this Ph.D. thesis provided insights into a possible recycling pathway for REEs found in EoL magnets from e-wastes.

Trying to merge the valorisation of these two wastes, this Ph.D. thesis aimed to recover Neodymium (Nd) and Dysprosium (Dy) from EoL magnets, by adsorption using porous carbons obtained from spent tyre rubber.

To achieve these two main objectives, the following specific objectives were defined:

1. **Spent Tyre Pyrolysis for Char Production.**
   1.1. Optimization of pyrolysis conditions to maximize char yield.

2. **Porous Carbon Production, Optimization, and Characterization.**
   2.1. Physical and chemical activation of ST chars.
   2.2. Textural, physical, and chemical characterization of obtained PCs and their precursors.

3. **Nd and Dy Competitive Adsorption Studies.**
   3.1. Batch studies and optimization of single component and multi-component competitive adsorption.
   3.2. Dynamic fixed-bed column studies and optimization of single component and multi-component competitive adsorption.

4. **Rare Earth Elements Recovery from EoL Magnets.**
   4.1. NdFeB magnet leaching.
   4.2. Nd and Dy recovery from magnet leachates using ST carbons.
   4.3. Application of recovered REEs as photocatalysts for H_2 production.

5. **Dissemination**
   5.1. Publication of scientific papers in international journals referenced in WoS and/or Scopus.
   5.2. Communications in international scientific conferences.
   5.3. A Ph.D. thesis comprising all the gathered information.

1.3 Literature Review

To structure and design the laboratory work conducted in this thesis, as well as to assess the scientific relevance and innovation of the present study, an extensive literature review was undertaken. To ensure a representative review, a systematic search of the available literature was performed. The search covered publications from 2000 until 2024, using key terms such as: (i) Rare earth elements; (ii) carbon-based materials, (iii) REE adsorption, (iv) REE recovery; (v) chars; (vi) biochar; (vii) activated carbon; (viii) spent tyre rubber, (ix) pyrolysis, (x) recycling, and (xi) photocatalysis. The consulted databases were: (i) Scopus; (ii) Web of Science; (iii) Google Scholar; (iv) PubMed.

By addressing these objectives, this literature review section seeks to underline the potential of carbon-based materials in contributing to a sustainable solution for REE recovery and to encourage further research in this field. This review focused on the four major topics of the thesis:

(i) Spent Tyres Rubber
(ii) Rare Earth Elements
(iii) Adsorption of Neodymium and Dysprosium
(iv) Photocatalysis for H_2 Production

Part of this review was published, partially or completely, in the following scientific publication:

- M. Nogueira, M. Bernardo, M. Ventura, I. Matos, F. Pinto and N. Lapa, (2024) Opportunities and Constraints of the Adsorption of Rare Earth Elements onto Pyrolytic Carbon-Based Materials: A Mini-Review, *Processes*, 12, 2257, doi.org/10.3390/pr12102257

1.3.1 Spent Tyre Rubber

One waste stream that demands the creation of sustainable management and valorisation pathways is spent tyre (ST), more specifically, the rubber of ST. The disposal of ST represents a major environmental threat worldwide and the forecast is the continuous growth of this problem as more tyres are being produced and consequentially disposed of each year. The production rate shows a steep increase, due to the growing demand from developing countries [2].

The same proprieties that make them desirable to be used as tyres, mainly durability and high mechanical resistance, have the consequence of making their disposal and valorisation harder. They are also resistant to biological degradation.

Current estimations show that around 1.5 billion tyres are produced each year, resulting in 17 million tons of spent tyres being disposed of yearly, a number that will continue to grow as time passes, further highlighting the need to find a solution to this problem [23]. The main disposal routes for this waste are landfilling, stockpiling, and to a lesser extent, the energetic valorisation through combustion, all of which imply the loss of the material, as well as the production of highly toxic compounds and the emission of green-house gasses (GHG) [2,3]. Taking into account the aforementioned, ST recycling and valorisation should be strengthened with new solutions and optimization of the current management policies and processes. Pyrolysis demonstrates to be a viable route for ST valorisation, as it effectively converts wastes into high added-value products, such as liquid products that may be used as fuels or as raw materials, and porous carbon (PC) materials that can be used in different industries [4,7]. Among the many applications of PC, their unique properties make them highly efficient as adsorbents and ideal supports for catalysts to synthesize valuable compounds [5,6]. Tyre waste is an ever-growing problem that requires new, efficient, and environmentally friendly routes for its recycling. Transformation of tyre waste into high added-value materials provides a way to ensure the re-use and valorisation of the rubber material.

Spent tyre rubber composition varies depending on the application they were designed for, nevertheless they are mainly composed of different types of rubber (natural, butyl, and styrene-butadiene), carbon black, and a mineral fraction constituted primarily of sulfur and zinc, as well as magnesium and calcium. They are also characterised by a high energy content (around 30 $MJ.kg^{-1}$) [2].

The pyrolysis of spent tyres has proved to be a promising pathway for tyre recycling due to the ability to transform a high volume of waste material into added-value products with low emissions and low energy demand [3,7]. The resulting products from the pyrolysis of spent tyres (oil, char, and gas) can be used to create a large variety of goods like carbon black, activated carbon, fine chemicals, solvents, fuels, and electricity amongst others. Spent tyre pyrolysis char is a sub-product that is exceptionally useful, as it can be used in its state as an adsorbent or as fuel. It can also be further processed into products such as syngas through gasification, or converted into higher-value carbonaceous materials such as activated carbon or recycled carbon black [2,6,8] that can be used in plastics, tonners, or as recycled carbon black to be re-introduced in new tyres (recent concept of green tyres). Spent tyre pyrolysis char is characterized by high carbon content, low water percentages, high mineral ratios (mainly

represented by sulfur and zinc), and relatively low surface areas, all of this make them suitable contenders for activated carbon production. The usage of the char fraction to produce activated carbons is considered one of the most favourable routes of valorisation as it requires less processing while producing a material with a higher value and more demand when compared to its other usages (fuel or carbon black) [7]. This approach deems it a more circular economy-driven, cleaner, and both an economical and environmentally sustainable pathway for valorisation.

Activated carbon (AC) is a type of carbon-based material characterized by high porosity, large surface areas, high surface reactivity, elevated surface functional groups, low density, high mechanical strength, and high adsorption capacity and kinetics [4,5,7]. These proprieties coupled with the easy production on an industrial scale make ACs a favourable material for application in adsorption processes [4,6].

The use of industrial wastes as precursors for the manufacture of activated carbon is a topic that has been gaining some traction in recent years. This group of wastes, in which spent tyres may be included, generally show properties that are desirable in precursors for ACs such as high carbon and low inorganic contents, as well as high availability at a low price, but above all, the fact that they are promoting circular economy [4,5,8].

AC is generally produced by thermo-chemical processes such as pyrolysis or gasification of carbon-containing materials such as biomass, polymers, plastics, and mineral charcoal [4,5,9]. The production of AC consists of two steps: (i) the carbonization of the precursor raw material under an inert atmosphere with temperatures up to 800 ^{o}C, where the resulting product is called char (carbonized material); (ii) afterward, the char is subjected to an activation step which can either be physical or chemical, depending on the used process. The activation step is responsible for the further development of the porous structure of the material (higher surface areas), the additional fixation of carbon, and the introduction of functional groups or hetero-atoms to the surface of the material which will enhance its adsorptive characteristics. Physical activation of carbons involves the exposure of the carbonaceous material to elevated temperatures (upwards of 800 ^{o}C) in the presence of oxidizing gases such as carbon dioxide, steam, air, pure oxygen, or a mixture of these. Chemical activation consists in mixing the char with chemical activating agents such as dehydrating compounds and/or oxidants while the material is exposed to relatively high temperatures (around 600 ^{o}C). This last method has a constraint, which is the need to wash out the chemical agents before the use of the AC in its target application.

Pyrolysis (also known as chemical recycling) has been demonstrated to be a viable route for waste and by-product valorisation, as it effectively converts wastes into high added-value products, such as chars, activated carbons, and other materials, that can be used in

different industries in a wide range of applications. Among the possible applications for chars and activated carbon, their singular properties turn them into low-cost and sustainable potential adsorbents for the removal of pollutants and/or contaminants from water, and the recovery of high-interest compounds [10,11].

1.3.2 Rare Earth Elements

Rare earth elements (REEs) are a group of seventeen metallic elements with chemical similarities, which include the lanthanide series (La, Ce, Pr, Nd, Pm, Sm, Eu, Gd, Tb, Dy, Ho, Er, Tm, Yb, and Lu) as well as Sc and Y. These elements are critical raw materials (CRM) for the technological industry in Europe and worldwide [21,24,25].

In its latest report on Critical Raw Materials for the European Union (EU), the European Commission identified REEs as the most critical group (Figure 1), due to the highest supply risk [24]. This was also recognized by the United States Department of Energy in their Critical Materials Strategy [21,25]. The most critical REEs are dysprosium (Dy), europium (Eu), neodymium (Nd), terbium (Tb), and yttrium (Y) [18].

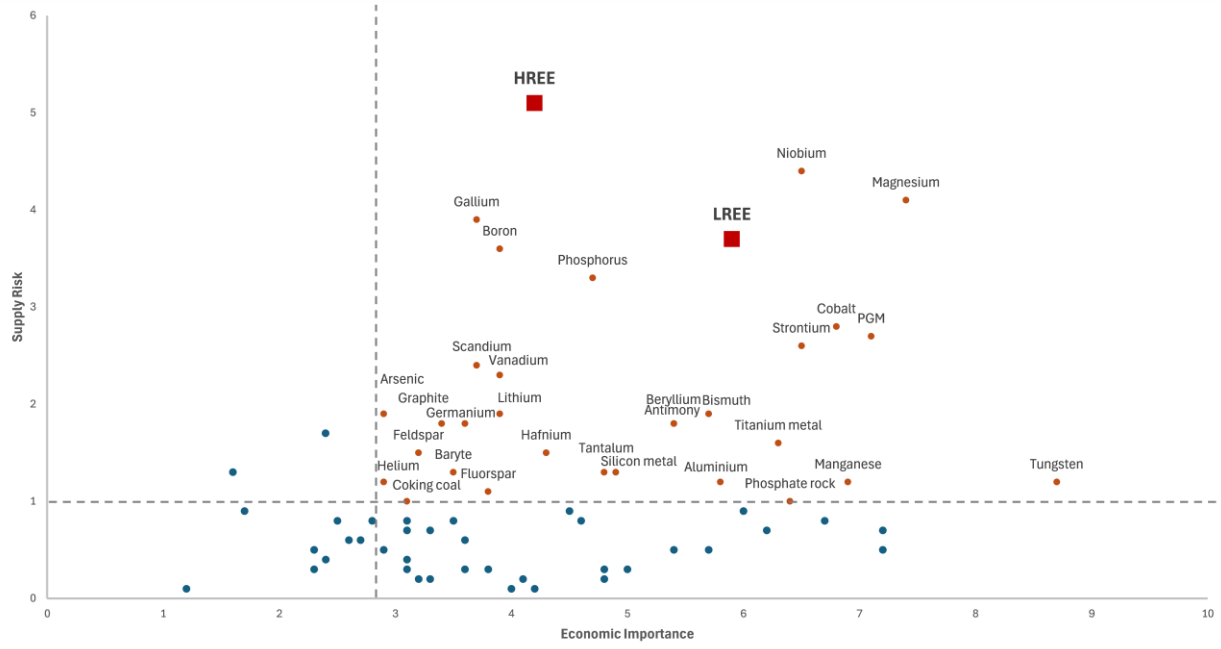

Figure 1 - Economic importance and supply risk of CRM; REEs highlighted by red square markers; source [24,26]

REEs do not occur in nature as individual native metals due to their reactivity but instead exist together in various ores and minerals, typically as minor constituents. Although REEs can be found in a wide variety of minerals and ores, they are confined to specific

geological environments. This creates a problem for the supply risk level, as most REEs' deposits are concentrated in a small group of countries including China, Brazil, Vietnam, Russia, India, and Australia [27]. Other reserves are scattered globally but account for less than 1% of total world reserves. Currently, China produces nearly 80% of the global REE demand, followed by Australia with 15%, reinforcing the supply risk in Europe and the USA, as 95% of production is met by just these two countries [18,20,27].

Table 1 highlights the importance of REEs due to their wide applicability in different technologies and industrial sectors.

Table 1 - Overview of major REE applications by industrial sector

Industrial sector	Applications
Technology	Permanent magnets, lasers, optical glass, fibre optics, masers, radar detection devices, nuclear fuel rods, mercury vapor lamps, highly reflective glass, computer memory, nuclear batteries, high-temperature superconductors
Electronics	TV screens, computers, cell phones, silicon chips, monitor displays, long-life rechargeable batteries, camera lenses, light-emitting diodes (LEDs), compact fluorescent lamps (CFLs), scanners, propulsion systems
Medical sector	Portable X-ray machines, X-ray tubes, magnetic resonance imagery, contrast agents, nuclear medicine imaging, cancer treatment applications, genetic screening tests
Renewable energy	Hybrid automobiles, wind turbines, rechargeable batteries, biofuel catalysts, hydrogen storage, fuel cells
Diverse manufacturing sectors	High-strength magnets, metal alloys, stress gauges, ceramic pigments, colorants, chemical oxidizing agents, polishing powders, polymer production, metal alloy strengthening-additive, automotive catalytic converters

Adapted and sourced from [24,27,28]

REEs play an increasingly vital role in the transition to a sustainable, low-carbon, and low-environmental impact economy due to their unique magnetic, catalytic, and phosphorescent properties. These properties make them critical resources for a wide range of high-technology industries (Table 1) such as cell phones, televisions, and lamp phosphors, as well as wind turbines and electric vehicles [20,27,29]. In terms of REE usage by application, Table 2 displays the percentage of REEs used yearly by each application, where it is possible to perceive that the magnet and catalyst markets are the biggest customers of REEs, each consuming 20% of the total used REEs.

Table 2 - Distribution of REE usage (%) by application

Magnets	**Batteries**	**Metallurgy**	**Catalysts**	**Polishing**	**Glass**	**Phosphors**	**Ceramics**	**Others**
20	8	11	20	15	7	9	3	6

Adapted and sourced from [28–30]

The EU has identified CRMs as materials of high economic and strategic importance for its economy, with significant supply risks. CRMs are not considered critical due to scarcity, but rather for their economic importance in key sectors, high supply risk due to the EU's reliance on foreign sources, and the absence of viable substitutes due to their unique properties and applications. The EU's list of 51 CRMs includes REEs, highlighting their critical nature [24].

To secure a sustainable supply of REEs, the EU must ensure a steady flow of these materials and support high-tech industries and research centres in finding solutions [29–31]. This can be achieved through several approaches: diversifying and globalizing supply chains, establishing new bilateral trade agreements, planning strategic reserves, adopting more sustainable and economical extraction methods, increasing resource efficiency, and promoting research initiatives [32]. In this context, developing pathways to recycle and reuse CRMs, such as extracting precious materials from Waste Electrical and Electronic Equipment (WEEE), is of particular relevance [24,29–31,33].

WEEE, also known as e-waste, is the end-of-life and unusable electrical equipment such as computers, smartphones, electric circuits, lamps and phosphors, magnets, wind turbines and generators, and electrical motors and batteries, i.e., every apparatus using electricity.

In today's society, increasingly dependent on technology combined with the increase in population, record amounts of WEEE are being produced, which will lead to various environmental and ecological problems. In Europe, it is estimated that 12 M tons of these types of wastes have been produced in 2020 alone, while worldwide production has reached 52 M

tons by 2021 [21]. The economic value of these wastes was appraised at 55 billion euros in 2016 [21,26,34]. This makes WEEE the fastest-growing waste stream, which unfortunately is characterized by poor management. Worldwide, today's response to this problem is based on unsustainable and un-ecological methods such as (i) exporting to developing countries for dismantling, (ii) disposal in landfills, and (iii) incineration. All these approaches are associated with large health and environmental issues [21,28,30].

Landfill and incineration of these residues are associated with air and water contamination due to the leaching and volatilization of hazardous compounds and metals. WEEE releases many toxic residues to the environment, such as PVC, mercury, lead, chromium, cadmium, gallium arsenide, and other toxic compounds and chemical elements. The shipment of these wastes to other countries does not solve the problem, it only transfers this issue to another geographical location and further contributes to other problems in different places, and mostly, it is promoting the exploration of new raw materials that will eventually lead to resource scarcity.

WEEE recycling has proven to have a positive impact due to various reasons such as (i) recovery of critical materials, (ii) energy savings, (iii) waste reduction, (iv) reduction of the dependency on foreign countries for CRM supply [21,27,28,30].

Although some rudimentary solutions are already applied, today's most applied WEEE recycling methods such as hydro and pyrometallurgy routes and the manual disassembly of the devices have proven to be inefficient and are characterized by big economic and environmental constraints. As such, society should seek alternatives, and new sustainable recycling solutions should be developed to help face these problems and promote the concept of the circular economy. This is where green chemistry and sustainable engineering come into play. Applying these concepts, methodologies, and principles in the development of new responses will enable the creation of sustainable pathways for waste management, as well as provide new routes for the production of new high added-value products from a stream of wastes.

One of the most promising candidates for WEEE recycling is REE containing permanent magnets. Neodymium-Iron-Boron (NdFeB) magnets have been identified as a key waste flow, with a high potential for the recovery of two REEs: neodymium (Nd) and dysprosium (Dy) [20]. NdFeB magnets are made of a $Nd_2Fe_{14}B$ matrix phase, enveloped in a neodymium-rich grain boundary phase where Dy is added to increase the magnets' temperature stability and magnetization capacity [35]. Computers' hard-disk drives (HDD) are one of the major applications of these types of magnets, and as such, have been appointed as a highly potential source for REE recovery [20,35,36].

Currently, no commercial methods to recycle Nd and Dy from HDDs are available, which leads to the most economically viable route to obtain these raw materials being the acquisition from primary sources (newly extracted metals) [19,37]. Several techniques have been proposed to recover REEs from HDDs, namely: (i) hydrometallurgical processing, and (ii) pyrometallurgical extraction, amongst others. Although various processes and routes have been proposed, their feasibility is hindered by several constraints, mainly related to economical aspects and more importantly, their ecological footprint [19,27,29]. As such, more sustainable and green-oriented research is mandatory to develop a pathway to recycle these materials that is feasible and sustainable in all aspects.

A current literature review suggests that the hydrometallurgical route for the recycling and recovery of REEs has the potential to be the most economically and environmentally safe pathway [21,37]. This route of recycling is comprised of several steps: (i) the dismantlement of the HDD and the separation of the magnet from the other compounds; (ii) the dissolution and/or leaching of the metals from the magnet; (iii) and finally, the separation of each REE from the solution. Though several methods have been proposed, they all have big environmental restraints associated with at least one of the steps described above. In the second step, the main constraint is the type of solvent and/or acid that are used for the dissolution of metals. Typically, sulfuric acid, nitric acid, or hydrochloric acid is used, which have a high ecological footprint, as such, new alternatives are being studied to offer more suitable substitutes. The biggest challenge lies within the third step: the separation of the REEs from the solution. Several methods have been proposed for this step: (i) liquid-liquid extraction; (ii) chemical precipitation; (iii) ion-exchange; (iv) and lately, adsorption. Of all these methods, adsorption has been identified as one of the most promising methods due to its simplicity, high efficacy, and wide range of accessible adsorbents.

Carbon-based materials have surfaced as highly promising adsorbents for the recovery of REEs from secondary raw materials, attributed to their specific properties, versatility, and cost-effectiveness [28,29]. These materials, in which activated carbon, chars, and biochars are included, possess high surface areas, abundant pore structures, and a wide array of functional groups that promote the adsorption of REEs [28,38]. The porous structure of these materials allows for a higher contact area that can interact with REE ions, increasing their adsorption capacity [39]. Moreover, these adsorbents can be derived from a variety of low-cost and sustainable sources, for instance, wastes, biowastes, biomass, and other industrial by-products, which promote these materials as environmentally and economically sustainable options for large-scale applications [7,17,40].

Activated carbons are produced by the pyrolysis of carbonaceous matrices followed by an activation step (either physical or chemical) in which the morphology of the structure is

further developed resulting in increased surface areas [41]. They have been widely studied for their excellent adsorption capacities [42]. Similarly, biochar and chars, which are yielded through the pyrolysis of biomass under inert atmosphere conditions, offer potential advantages due to their environmental benefits and lower production costs [17,43,44]. The presence of functional groups on these adsorbents' surface, such as carboxyl, hydroxyl, and phenolic groups, as well as their mineral content, play a pivotal part in the adsorption of REE ions [43,45–48]. These materials not only sequester carbon but also provide a sustainable method for waste management through their economic added-value.

1.3.3 Rare Earth Elements Adsorption Using Pyrolytic Carbon-Based Materials

The adsorption of REEs is scarcely reported in the literature [28,39,48]. Specifically, studies on the adsorption of these metals onto porous carbon materials are even rarer, with only a few available papers addressing this topic. Reports on the competitive adsorption and dynamic adsorption of these lanthanides are even fewer.

Given the critical need for resource recovery and the practical challenges associated with the production and application of carbon materials, this section of the literature review focuses on the adsorption of REEs using chars, activated carbons, and other simpler carbon materials. "Simpler carbon materials" refer to those that are more readily available and cost-effective, typically derived from wastes, biomass or other inexpensive precursors and require less complex production processes compared to advanced materials like carbon nanotubes (CNT), fullerenes, and graphene. This focus aligns better with the objectives of sustainable resource recovery, emphasizing practical and scalable solutions for REE recovery. By excluding more complex and harder-to-produce materials, the review ensures broader applicability and feasibility in industrial processes. Nevertheless, some of these advanced materials will be analysed for comparison purposes. Beyond carbon-based materials, other types of adsorbents have been studied in the context of REE recovery or adsorption. Examples of these materials include metal-organic frameworks, zeolites, clays, ion-exchange resins, and composite materials [28,39,49]. Research on these materials offers alternative insights into adsorption processes, with each being investigated for REE recovery in specialized applications.

This section of the review aims to provide a comprehensive overview of the current state of research on the adsorption of REEs onto carbon-based materials. Specifically, it will: (i) Evaluate the types of carbon-based adsorbents used for REE recovery, including activated carbon, chars, and biochar; (ii) Analyse the adsorption mechanisms and factors influencing

adsorption efficiency; (iii) Compare adsorption capacities of different carbon-based materials; (iv) Highlight the challenges and limitations in current research, especially the variability in experimental conditions and the scarcity of real-world application studies; (v) Suggest future research directions to enhance the practical applicability of carbon-based adsorbents for sustainable and efficient REE recovery.

Table 3 presents a summary of the current progress made toward the adsorption of REEs using carbon-based materials. This review highlights the importance of these materials in promoting sustainable resource recovery, providing insights into their adsorption capacities and practical applications.

Table 3 - Adsorption of REEs using carbon-based materials

Adsorbent	Type of adsorption assay	Tested REE	Max. adsorption capacity ($mg.g^{-1}$)	Recovery capacity (%)	S_{BET} ($m^2.g^{-1}$)	pH	Temperature (K)	Ref.
Functionalized Lignin Activated Carbon	Batch	Nd	335.5	100	837	2, 4, 6	Room	[50]
Functionalized Lignin Activated Carbon		Dy	344.6	100	837			
Spent Coffee Physical Activated Carbon	Batch	Dy	33.52	100	2330	3 - 5	303, 318, 333	[51]
Spent Coffee Chemical Activated Carbon			31.26	100	982			
Commercial Activated Carbon	Batch	Nd	36.65	73	980	-	293	[52]
Multi-Wall Carbon Nanotubes from Crystalline Nano Cellulose	Batch	Dy	48.14	100	-	2 - 7	290, 298, 208	[53]
Sawdust Biochar	Batch	Nd	8.0	40	4.7	3	Room	[54]
		Sc	7.5	38				
Commercial Activated Carbon (CAC)		Nd	8.8	44	912			
		Sc	8.5	42				
Carbon Black from Recycled Tires	Batch	Nd	0.54	-	57	-	298, 313, 333, 353	[55]
		La	0.34					
		Ce	0.70					
		Sm	0.55					
		Y	0.46					
Commercial Activated Carbon (CAC)	Batch	Nd	19.1	-	711	5	293	[56]
Oxidized CAC			50.8		761			
EDTA Functionalized Oxidized CAC			71.4		741			
Oxidized Carbon nanofibers	Column	La	18.1	-	-	1 - 7	-	[57]
		Eu	17.6					
		Gd	14.2					
		Yb	19.1					

PAN Grafted Carbon Nanotubes-Silica	Batch	La Sc Y	103.5 112.7 84.1	-	107	1 - 6	296, 318	[58]
Carbon Xerogel-Chitosan Composite	Batch	-	163.9	-	275	0.5 - 6	298	[59]
Carbon Nanoparticles	Batch	Nd La	0.45 0.51	99 99	1800	3	293	[60]
PAM-Activated Carbon Composite	Batch	Nd Ce Gd	9.88 9.61 9.26	-	-	-	298	[61]
Commercial Activated Carbon	Batch	La Yb Lu Eu Y Sc La	0.048 0.053 0.052 0.038 0.057 0.069 0.071	-	381	2 - 8	298	[62]
$KMnO_4$ Modified Commercial Activated Carbon		Yb Lu Eu Y Sc	0.084 0.075 0.097 0.089 0.121	-	346			
Oligo-Grafted Synthetic Mesoporous Carbon	Batch	Lu Dy La	9.57 38.27 52.15	-	-	-	-	[63]
Commercial Activated Carbon	Batch	Eu	20.0	-	-	2 - 11	298	[64]
Graphene Oxide Nanosheets			161.3		120			
Commercial Activated Carbon	Batch	Sc	2.1	-	405	1 - 6	Room	[65]
Carbon Nanotubes			37.9		227			
Graphite Oxide			36.5		175			
Apricot Stone Char	Batch	Eu	17.8	-	100	2 - 8	293, 313, 333	[47]
Activated Carbon (H_3PO_4 activation)			29.3		554			
Activated Carbon (KOH activation)			28.4		98			
Schiff's Base Modified Activated Carbon	Batch	La	144.8	-		1 - 7	Room	[46]
CMK-8 (Ordered Mesoporous Carbon)	Batch	Sm	3.31	-	914	2.6	-	[45]
Oxidized CMK-8			22.3		933			
DGO grafted CMK-8			9.83		439			
Spent Tire Rubber Char (A450)	Batch	Nd Dy	10.0 11.7	-	74	-	Room	[38]
Spent Tire Rubber Char (B450)		Nd Dy	12.5 13.1		73			
Spent Tire Rubber Char (A900)		Nd Dy	32.8 34.3		75			

Spent Tire Rubber Char (B900)		Nd	28.2		73			
		Dy	32.8					
Commercial Activated Carbon		Nd	12.8		1030			
		Dy	10.8					
Mesoporous Carbon	Batch	La	2.0	-	594	-	-	[66]
		Dy	1.8					
		Lu	1.6					
Carboxylated Mesoporous Carbon		La	4.3		438			
		Dy	6.0					
		Lu	6.5					
Soybean Pod Activated Carbon	Batch	Ce	107.7	-	614	1 - 6	298, 308, 318, 328	[67]
		La	127.2					
Wood Waste Biochar	Batch	Ce	327.9	-	8.8	1 - 7	298, 308, 318, 328	[68]

The adsorption of Nd and Dy using functionalized lignin AC was investigated by Saha *et al.* The study reported adsorption capacities of 335.5 mg.g^{-1} for Nd and 344.6 mg.g^{-1} for Dy, which were attributed to the increased number of binding sites introduced by the functionalization. Despite the material's S_{BET} of 837 m².g^{-1}, the improved adsorption performance was primarily driven by the enhanced surface chemistry resulting from the functional groups added during modification [50].

The use of AC derived from spent coffee grounds, activated through physical and chemical methods, was explored for Dy removal by Alcaraz *et al.* The physically activated AC exhibited an adsorption capacity of 33.52 mg.g^{-1} with an S_{BET} of 2330 m².g^{-1}, while the chemically activated AC demonstrated an adsorption capacity of 31.26 mg.g^{-1} with an S_{BET} of 982 m².g^{-1}. These findings highlight the impact of activation methods on adsorption performance, despite the differences in surface area [51].

The adsorption of Nd using commercial AC was examined by Qadeer, who reported a maximum uptake capacity of 36.65 mg.g^{-1} under the tested conditions. The material's S_{BET} was measured at 980 m².g^{-1}, suggesting that the adsorption performance was influenced by both the surface area and the inherent properties of the commercial AC used in the study [52].

The use of multi-wall CNTs derived from crystalline nanocellulose for the adsorption of Dy was investigated by Zheng *et al.* Their study reported an adsorption capacity of 48.14 mg.g^{-1} [53].

Komnitsas *et al.* studied the adsorption of Nd and Sc using sawdust biochar with an S_{BET} of 4.7 m².g^{-1}. The adsorption capacities were found to be 8.0 mg.g^{-1} for Nd and 7.5 mg.g^{-1} for Sc [54].

Smith *et al.* explored the adsorption of various REEs using carbon black derived from recycled tires with a surface area of 57 $m^2.g^{-1}$. The adsorption capacities were 0.54 $mg.g^{-1}$ for Nd, 0.34 $mg.g^{-1}$ for La, 0.70 $mg.g^{-1}$ for Ce, 0.55 $mg.g^{-1}$ for Sm, and 0.46 $mg.g^{-1}$ for Y [55].

The adsorption of Nd using various forms of commercial activated carbons (CAC) was investigated by Babu *et al.* The unmodified CAC showed an adsorption capacity of 19.1 $mg.g^{-1}$ with an S_{BET} of 711 $m^2.g^{-1}$. When oxidized, the adsorption capacity increased to 50.8 $mg.g^{-1}$ with an S_{BET} of 761 $m^2.g^{-1}$. The highest adsorption capacity was observed with EDTA-functionalized oxidized CAC (EDTA - Ethylenediaminetetraacetic acid), which achieved 71.4 $mg.g^{-1}$ with an S_{BET} of 741 $m^2.g^{-1}$. This progression indicates the significant impact of surface modification and functionalization on adsorption performance [56].

Chen *et al.* used oxidized carbon nanofibers for the adsorption of La, Eu, Gd, and Yb. The adsorption capacities were 18.1 $mg.g^{-1}$ for La, 17.6 $mg.g^{-1}$ for Eu, 14.2 $mg.g^{-1}$ for Gd, and 19.1 $mg.g^{-1}$ for Yb [57].

The adsorption of La, Sc, and Y using PAN (Polyacrylonitrile) grafted CNT-silica composites was investigated by Ramasamy *et al.* The adsorption capacities were 103.5 $mg.g^{-1}$ for La, 112.7 $mg.g^{-1}$ for Sc, and 84.1 $mg.g^{-1}$ for Y, with an S_{BET} of 107 $m^2.g^{-1}$, highlighting the effectiveness of surface grafting [58].

Haggag *et al.* developed a carbon xerogel-chitosan composite for the adsorption of REEs. The adsorption capacity was 163.9 $mg.g^{-1}$, with an S_{BET} of 275 $m^2.g^{-1}$ [59].

Younis *et al.* investigated the adsorption of Nd and La using carbon nanoparticles with an S_{BET} of 1800 $m^2.g^{-1}$. The adsorption capacities were 0.45 $mg.g^{-1}$ for Nd and 0.51 $mg.g^{-1}$ for La [60].

The adsorption of Nd, Ce, and Gd using PAM-activated carbon composite (PAM – Polyacrylamide) was studied by El-Masry *et al.* The adsorption capacities were 9.88 $mg.g^{-1}$ for Nd, 9.61 $mg.g^{-1}$ for Ce, and 9.26 $mg.g^{-1}$ for Gd [61].

The adsorption of various REEs onto CAC modified with potassium permanganate ($KMnO_4$) was investigated by Kano *et al.*, revealing that the $KMnO_4$ modification enhanced the adsorption capacities compared to unmodified CAC. For instance, the adsorption capacity for Sc increased from 0.069 $mg.g^{-1}$ to 0.121 $mg.g^{-1}$. Similarly, enhancements were observed for other REEs such as La, Yb, Lu, Eu, and Y, demonstrating the effectiveness of $KMnO_4$ modification in improving adsorption performance [62].

Gismondi *et al.* explored the adsorption of La, Dy, and Lu using oligo-grafted synthetic mesoporous carbon. The adsorption capacities were 52.15 $mg.g^{-1}$ for La, 38.27 $mg.g^{-1}$ for Dy, and 9.57 $mg.g^{-1}$ for Lu [63].

Sun *et al.* investigated the adsorption of REEs using graphene oxide (GO) nanosheets, achieving an adsorption capacity of 161.3 $mg.g^{-1}$ [64].

Kilian *et al.* conducted a comparative study on the sorption of Sc onto various carbon-based materials. The adsorption capacity of CAC for Sc was found to be 2.1 $mg.g^{-1}$ with an S_{BET} of 405 $m^2.g^{-1}$. Additionally, the study included CNTs and GOs, which showed significantly higher adsorption capacities of 37.9 $mg.g^{-1}$ and 36.5 $mg.g^{-1}$, respectively, although these materials were not the primary focus due to their production complexities [65].

The factors affecting the sorption/desorption of Eu using various ACs were explored by Gad and Awwad. The apricot stone char exhibited an adsorption capacity of 17.8 $mg.g^{-1}$, while activated carbons with H_3PO_4 and KOH activation showed capacities of 29.3 $mg.g^{-1}$ and 28.4 $mg.g^{-1}$, respectively. These findings underscore the importance of activation methods in enhancing the adsorption performance of carbon materials [47].

Marwani *et al.* studied the adsorption of La using Schiff's base-modified AC, reaching an adsorption capacity of 144.8 $mg.g^{-1}$ [46].

The adsorption of Sm using CMK-8, an ordered mesoporous carbon, was investigated by Perreault *et al.* The adsorption capacity was 3.31 $mg.g^{-1}$ with an S_{BET} of 914 $m^2.g^{-1}$. Oxidized CMK-8 had an adsorption capacity of 22.3 $mg.g^{-1}$ with an S_{BET} of 933 $m^2.g^{-1}$, and DGO (diglycolylester) grafted CMK-8 had an adsorption capacity of 9.83 $mg.g^{-1}$ with an S_{BET} of 439 $m^2.g^{-1}$ [45].

The use of carbon-based adsorbents derived from spent tire rubber for the recovery of Nd and Dy was explored by Nogueira *et al.* Their study investigated different char types produced at various temperatures. The spent tire rubber char (A450) exhibited adsorption capacities of 10.0 $mg.g^{-1}$ for Nd and 11.7 $mg.g^{-1}$ for Dy, while char (B450) showed slightly higher capacities of 12.5 $mg.g^{-1}$ for Nd and 13.1 $mg.g^{-1}$ for Dy. Chars produced at higher temperature, such as A900 and B900, demonstrated significantly enhanced adsorption capacities, with A900 adsorbing 32.8 $mg.g^{-1}$ of Nd and 34.3 $mg.g^{-1}$ of Dy, and B900 adsorbing 28.2 $mg.g^{-1}$ of Nd and 32.8 $mg.g^{-1}$ of Dy. These findings highlight the influence of pyrolysis temperature on the adsorption performance of carbon materials derived from waste rubber [38].

Saha *et al.* studied the adsorption performance of mesoporous carbon and a carboxylated version of the same material and observed that the carboxylated material adsorbed 2 to 4 times the quantities of REEs when compared with its pristine version. This investigation emphasized that although the carboxylated material had lower surface areas and pore volumes than the pristine mesoporous carbon, the enhancement of REE uptake was undoubtedly caused by the carboxylate functionalization. They further evaluated the recovery of REEs from coal fly ashes leachates [66].

Pinheiro *et al.* studied the adsorption of Ce and La onto soybean pod AC. The material they produced was able to achieve maximum uptake capacities of 107.7 and 127.2 $mg.g^{-1}$ for

Ce and La respectively. They also evaluated the recovery of these REEs from phosphogypsum leachate [67].

A wood waste biochar produced by hydrothermal carbonization of *Prunus serrulata* bark was studied for the adsorption of Ce by Reis *et al.* [68]. Although the material has a very low surface area (8.8 $m^2.g^{-1}$), it was able to reach uptake capacities of 327.9 $mg.g^{-1}$ due to surface precipitation resulting from the REE interaction with -OH and -COOH functional groups, as well as surface complexation with hydroxyl groups on the biochar's surface. The material was also assayed for the recovery of Ce from phosphogypsum leachate [68].

The maximum adsorption capacities of REEs on various carbon-based adsorbents fluctuate greatly depending on the surface area of the material, their mineral composition, the surface chemistry and the presence of grafted or added compounds [49,69]. Functionalized lignin-activated carbon exhibits the highest adsorption capacities for Nd and Dy, with values of 335.5 $mg.g^{-1}$ and 344.6 $mg.g^{-1}$, respectively, and an S_{BET} of 837 $m^2.g^{-1}$. This high performance can be attributed to phosphorus functionalization, which enhances the binding sites available for REEs, leading to superior adsorption performance [50,63].

In comparison, spent coffee AC also shows high adsorption capacities, particularly when physically activated, with an adsorption capacity of 33.52 $mg.g^{-1}$ for Dy and an exceptionally high S_{BET} of 2330 $m^2.g^{-1}$. However, the chemically activated version, while still effective with a capacity of 31.26 $mg.g^{-1}$ for Dy, has a significantly lower S_{BET} of 982 $m^2.g^{-1}$. This demonstrates that higher surface area alone does not necessarily correlate with higher adsorption capacity, as the type of activation and presence of functional groups play crucial roles [51].

Carbon materials with specific modifications or grafting often show enhanced adsorption capacities. For instance, PAN-grafted CNT-silica composites show high capacities (103.5 $mg.g^{-1}$ for La and 112.7 $mg.g^{-1}$ for Sc) with an S_{BET} of 107 $m^2.g^{-1}$, illustrating the significant impact of grafting on adsorption performance despite a relatively lower surface area [58].

Carbon xerogel-chitosan composites and GO nanosheets also highlight the importance of functionalization [59,64]. The xerogel-chitosan composite has an adsorption capacity of 163.9 $mg.g^{-1}$ with an S_{BET} of 275 $m^2.g^{-1}$, while GO nanosheets, with an S_{BET} of 120 $m^2.g^{-1}$, achieve an adsorption capacity of 161.3 $mg.g^{-1}$. These examples underscore that specific functional groups such as hydroxyl, and oxygen-containing groups, as well as composite structures such as the ones found in chitosan composites, can dramatically enhance adsorption capacities, sometimes even more than materials with larger surface areas but without such chemical modifications.

Conversely, materials like carbon black from recycled tires, with an S_{BET} of 57 $m^2.g^{-1}$, show much lower adsorption capacities (0.54 $mg.g^{-1}$ for Nd). This indicates that without functionalization, grafting, or intrinsic mineral content, materials with lower surface areas tend to have reduced adsorption capabilities [55]. Comparatively, chars from spent tire rubber, with similar low surface areas (74 $m^2.g^{-1}$) exhibit higher adsorption capacities (32.8 $mg.g^{-1}$ for Nd) due to the presence of metals in their matrix [38] which can participate in the ion exchange mechanism. Similarly, the ordered mesoporous carbon (CMK-8) shows a significant increase in adsorption capacity when oxidized (22.3 $mg.g^{-1}$) compared to its non-oxidized form (3.31 $mg.g^{-1}$), despite a minor increase in surface area (from 914 $m^2.g^{-1}$ to 933 $m^2.g^{-1}$) [45].

In summary, while surface area is a critical factor in determining the adsorption capacity of carbon-based materials for the adsorption of REEs, the presence of functional groups, grafted compounds, or mineral content often plays a more pivotal role in the adsorption mechanisms. Materials with lower surface areas but significant functionalization or grafting can outperform those materials with higher surface areas but no modifications, highlighting the importance of chemical modifications in enhancing adsorption performance.

1.3.3.1 Adsorption Mechanisms and Influencing Factors

The adsorption of REEs onto carbon-based materials involves several mechanisms (Figure 2), each contributing to the overall adsorption capacity and efficiency [28,48,69]. Understanding these mechanisms is crucial for optimizing the design and application of adsorbents. The primary adsorption mechanisms include:

i. Physical Adsorption: Physical adsorption, also known as physisorption, is driven by Van der Waals forces and other weak bonds. It occurs when REE ions are attracted to the surface of the carbon-based adsorbent without any chemical bonding. This type of adsorption is usually reversible and depends on the surface area and pore structure of the adsorbent [27,28].

ii. Electrostatic Interactions: Electrostatic interactions involve the formation of strong chemical bonds between REE ions and the functional groups on the surface of the carbon material. This process is usually irreversible and results in a stronger attachment of the REEs to the adsorbent. Functional groups such as carboxyl, hydroxyl, and phenolic groups play a crucial role in electrostatic interactions, enhancing the adsorption capacity by providing specific binding sites for REEs [50,51,63].

iii. Ion Exchange: Ion exchange is a process where REE ions in solution replace other ions on the surface of the adsorbent. This mechanism is highly dependent on the

pH of the solution and the presence of ionizable functional groups on the adsorbent. Ion exchange is particularly effective in materials such as modified activated carbons, chars, and biochars that have been functionalized to enhance their ion exchange capacities or are rich in mineral content that can perform ionic exchange [38,56,57].

iv. Complexation: Complexation involves the formation of coordination complexes between REE ions and functional groups on the adsorbent surface. This mechanism is influenced by the type and availability of functional groups, such as amino, carboxyl, and phosphonic groups. Complexation often leads to the formation of stable REE-ligand complexes, significantly enhancing the adsorption capacity of the material [50,51,56].

v. Precipitation: Precipitation occurs when REE ions react with functional groups or counter-ions present on the adsorbent surface, leading to the formation of insoluble REE compounds that deposit onto the adsorbent. This mechanism is typically influenced by factors such as pH, ion concentration, and the presence of specific anions, which can form insoluble REE salts. Precipitation can enhance the overall adsorption efficiency by reducing the concentration of REE ions in solution, particularly under conditions that favour the formation of stable precipitates [70,71].

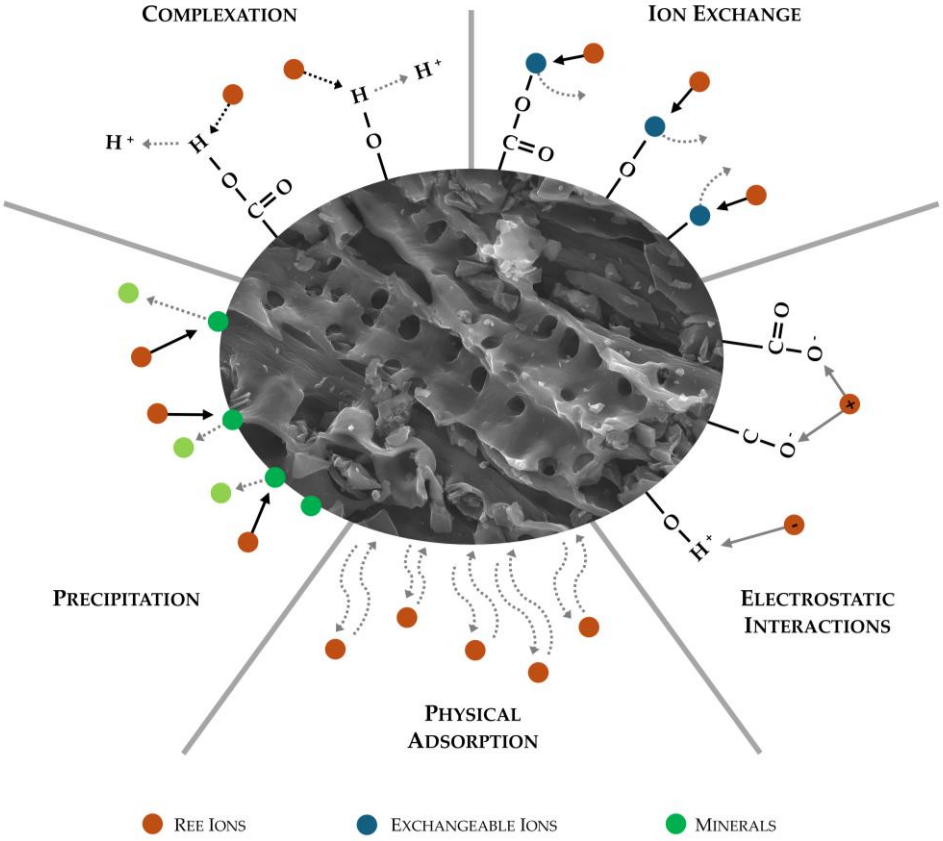

Figure 2 - Schematic of the main adsorption mechanisms of REEs onto pyrolytic carbon-based adsorbents; adapted from [70,72]

Several factors affect the efficiency of REE adsorption onto carbon-based materials. These factors include:

i. Surface Area: The surface area of the adsorbent is a critical factor influencing adsorption capacity. Materials with higher surface areas usually provide more adsorption sites, leading to greater adsorption capacities [60,64].

ii. Pore Size Distribution: The pore size distribution of the adsorbent affects the accessibility of REE ions to the adsorption sites. Micropores (pores < 2 nm) contribute to high adsorption capacities by providing a large surface area, while mesopores (2-50 nm) and macropores (> 50 nm) facilitate the diffusion of REE ions into the interior of the adsorbent. Optimal pore size distribution ensures efficient utilization of the adsorbent's surface area [54,55].

iii. Functional Groups: The presence and type of functional groups on the surface of the adsorbent materials characterize the chemical nature of the surface and are crucial for their adsorption capacity. Functional groups such as carboxyl, hydroxyl, and amino groups enhance adsorption capacity through chemisorption, ion

exchange, and complexation mechanisms. Recent studies have demonstrated that surface functionalization of carbon materials can significantly improve adsorption performance by introducing or increasing these functional groups [70,71,73]. Modifications such as the addition of oxygen-containing groups (e.g., carboxyl, hydroxyl), nitrogen-containing groups (e.g., amine, imine), and phosphorus-containing groups (e.g., phosphonate) have been shown to enhance adsorption by providing more active and selective binding sites for REEs [56,58]. Carboxyl (-COOH) groups enhance ion exchange and complexation by ionizing in aqueous solutions, particularly at neutral to alkaline pH. The resulting R-COO^- attracts REE ions via electrostatic interactions, and can form coordination bonds that can improve adsorption capacities. Hydroxyl (-OH) groups contribute to adsorption by forming hydrogen bonds and deprotonating in alkaline conditions, allowing strong interactions with REE ions. They boost adsorption of metals ions by facilitating surface complex formation and increasing adsorbent hydrophilicity. Nitrogen-containing groups such as amino (-NH_2) and imine (-C=NH) groups enhance adsorption through coordination bonds, where nitrogen donates electrons to form stable complexes with REEs. Phosphonate (-PO_3H_2) groups offer multiple binding sites, forming stable chelate complexes with metal ions. Other functional groups such as carbonyl (-C=O) and ether (-C-O) groups also enhance metal adsorption by forming surface complexes. Functionalization of carbon materials with these groups not only increases the adsorption capacity but also improves selectivity in the presence of competing metal ions. Molecular-level studies indicate that these modifications enhance the coordination environment for REEs, leading to stronger and more stable adsorption. Furthermore, advanced surface modifications, such as grafting ligands or chelating agents onto carbon-based adsorbents, can further boost adsorption efficiency by creating highly selective binding sites for REEs [56,58].

iv. pH: The pH of the solution influences the ionization state of both the REE ions and the functional groups on the adsorbent. At low pH, hydrogen ions compete with REE ions for adsorption sites, reducing adsorption efficiency. Conversely, at higher pH, the functional groups are more ionized, enhancing their ability to bind REE ions. Optimal pH conditions must be determined for each adsorbent-REE system to maximize adsorption efficiency [59,62].

v. Temperature: Temperature affects the kinetics and equilibrium of the adsorption process. Higher temperatures typically increase the diffusion rate of REE ions into the pores of the adsorbent, potentially enhancing adsorption capacity, particularly

for endothermic adsorption processes where heat absorption facilitates ion interaction and binding [74]. However, extreme temperatures can also disrupt the stability of adsorbent-REE interactions, particularly in chemisorption and complexation processes [64,65]. Conversely, in exothermic adsorption processes, where heat is released, higher temperatures can disrupt the stability of adsorbent-REE interactions and decrease adsorption capacity [75]. Therefore, the effect of temperature on adsorption efficiency depends on whether the adsorption process is exothermic or endothermic, with each mechanism exhibiting distinct behaviours under varying thermal conditions.

vi. Presence of Competing Ions: The presence of other ions in solution can compete with REE ions for adsorption sites, affecting the selectivity and capacity of the adsorbent. For example, the presence of common metal ions like calcium and magnesium can reduce the adsorption efficiency of REEs. Understanding the competitive adsorption behaviour is essential for developing selective adsorbents for REE recovery from complex matrices [38,47,62].

By optimizing these factors, the adsorption efficiency of carbon-based materials for REEs can be significantly enhanced, contributing to more effective and sustainable recovery processes.

1.3.3.2 Batch *versus* Dynamic Adsorption Assays

Batch adsorption assays are based on mixing a known mass of adsorbent with a solution containing specific concentrations of adsorbate. The mixture is then agitated for a determined time, allowing the adsorbate to interact with the adsorbent until the adsorption equilibrium is reached. Afterward, the adsorbate concentration remaining in the solution is quantified and the adsorption capacities of the materials are determined this way [76–79]. The majority of the studies on the adsorption of REEs onto carbon-based materials are performed in batch conditions, as evidenced by Table 3.

The benefits of applying batch conditions to these assays are:

i. Simplicity and convenience: These assays are very straightforward to perform, requiring only basic equipment such as a vessel to hold the mixture, a means to agitate or shake the mixture, and a system to separate the adsorbent from the mixture after the equilibrium is reached (filtration or centrifugation).

ii. Controlled conditions: The factors that control the adsorption processes, such as pH, temperature, and initial adsorbate concentrations can be easily controlled and

adjusted, facilitating the comprehension of their effects on the adsorption processes.

iii. Basic kinetic and isotherm data: This type of adsorption assay allows obtaining basic kinetic and isotherm data that provide a fundamental understanding of the adsorption process.

iv. Cost-effectiveness: The batch mode is relatively inexpensive when compared to dynamic assays, as it requires less equipment, as well as lower quantities of adsorbent and adsorbate.

Nevertheless, batch adsorption studies also suffer from some limitations such as:

i. Equilibrium limitations: Batch assays assume equilibrium conditions, which may not correctly reflect the dynamic nature of the adsorption process under industrial scale processes.

ii. Limited information: They provide limited information on the complex dynamics of the adsorption processes over time. For example, diffusional constraints cannot be assessed through batch assays.

iii. Scale-up challenges: The results obtained from batch assays rarely correlate to large-scale and/or industrial processes, which hinders the upscaling of the application of these materials into real-streams scenarios. Only in very limited situations, the industrial processes are running in completely-mixed systems as occurs in batch adsorption assays.

On the other hand, dynamic adsorption assays, also known as column assays, rely on circulating the adsorbate solution through a column filled with adsorbent materials [80]. The effluent is then collected at the output of the column, over time, and the adsorbate concentration is then quantified to determine the adsorption capacities and kinetics [76,77,79,81]. The available literature in which dynamic assays were performed is very scarce concerning REEs' adsorption, with only one study in this literature review, as can be seen in Table 3.

The major advantages of dynamic assays are:

i. Realistic conditions: Column assays simulate continuous flow conditions, which provide a more realistic representation of industrial processes while providing better insights into real-world applications.

ii. Kinetic information: These dynamic studies offer detailed information on adsorption kinetics, breakthrough performances, and mass transfer characteristics.

iii. Scalability: Contrary to batch studies, dynamic assays have a higher correlation with industrial processes, facilitating the scale-up and design of large-scale adsorption systems.

The limitations of the application of dynamic adsorption assays are:

i. Complexity: This type of adsorption assay requires more sophisticated equipment, such as columns, pumps, piping, and collectors, resulting in more complex setups that are harder to implement.
ii. Higher costs: Following the previous point, these more complex systems are more expensive and incur higher operating costs due to the need for continuous operation and larger quantities of adsorbates.
iii. Operational challenges: With higher complexity comes more opportunities for operation problems to appear and hinder the success of these assays. Factors such as column clogging, channelling, development of preferable pathways, and pressure drops can affect the performance and accuracy of dynamic assays.

Both batch and dynamic adsorption assays have their distinct advantages and limitations [79]. Batch assays are ideal for preliminary studies and understanding basic adsorption characteristics under controlled conditions. In contrast, dynamic assays are essential for investigating the practical applicability of adsorbents in continuous systems, providing insights into adsorption kinetics and scalability. For the adsorption of REEs onto carbon-based materials, employing both batch and dynamic assays can offer a comprehensive understanding of the involved processes. Initial batch studies can identify promising adsorbents and optimal conditions, while dynamic assays can validate these findings under continuous flow conditions, simulating real-world applications.

Incorporating both batch and dynamic adsorption assays in research provides a more suitable approach to evaluate the performance of carbon-based adsorbents for REE recovery. Future studies should aim to bridge the gap between laboratory-scale experiments and real-world applications, ensuring the development of economically and environmentally sustainable adsorption processes.

1.3.3.3 Adsorption Isotherms, Kinetic, and Breakthrough Models

The articles reviewed employ various adsorption isotherm and kinetic models to describe and analyse the adsorption behaviour of REEs onto carbon-based materials. As stated in the previous section, most studies only performed batch assays, resulting in only batch models

being applied. The most used models include the Langmuir and Freundlich isotherm models [82–85], as well as pseudo-first-order and pseudo-second-order kinetic models [46,84,86–88]. These models contributed to the understanding of adsorption mechanisms and the efficiency of different adsorbents.

1.3.3.3.1 Batch Isotherm Models

The Langmuir isotherm model assumes monolayer adsorption onto a surface with a finite number of identical sites [83–85,89]. It is described by the equation 1:

$$q_e = \frac{q_m \cdot K_L \cdot C_e}{1 + K_L \cdot C_e} \quad \text{(Eq. 1)}$$

where q_e is the amount of adsorbate adsorbed per unit mass of adsorbent (mg.g^{-1}), q_m is the maximum adsorption capacity (mg.g^{-1}), K_L is the Langmuir constant related to the affinity of binding sites (L.mg^{-1}), and C_e is the equilibrium concentration of adsorbate (mg.L^{-1}).

The Freundlich isotherm model, on the other hand, is an empirical model that assumes adsorption on heterogeneous surfaces [83–85,90]. It is described by the equation 2:

$$q_e = K_F \cdot C_e^{1/n} \quad \text{(Eq. 2)}$$

where K_F (mg.g^{-1})(mg.L^{-1})^n and n (adimensional) are the Freundlich constants indicative of adsorption capacity and adsorption intensity, respectively, and C_e is the equilibrium concentration of adsorbate (mg.L^{-1}).

More advanced and mechanistic batch isotherm models also exist, such as the Sips isotherm model, although no study present in this review applied it. The Sips isotherm model is a hybrid model that combines the Langmuir and Freundlich isotherms, useful for predicting heterogeneous adsorption systems at high adsorbate concentrations [91]. It is described by the equation 3:

$$q_e = \frac{q_{\mathrm{m}} \cdot (K_S \cdot C_e)^{1/n}}{1 + (K_S \cdot C_e)^{1/n}} \quad \text{(Eq. 3)}$$

where q_m is the maximum adsorption capacity (mg.g^{-1}), C_e is the equilibrium concentration of adsorbate (mg.L^{-1}), K_S (mg.L^{-1}) is the Sips constant, and n (adimensional) is the heterogeneity factor.

1.3.3.3.2 Batch Kinetic Models

The pseudo-first-order kinetic model is based on the assumption that the rate of occupation of adsorption sites is proportional to the number of unoccupied sites [84,86–88,92]. It is represented by the equation 4:

$$q_t = q_e \cdot \left[1 - e^{-k_f \cdot t}\right] \quad \text{(Eq. 4)}$$

where q_t is the amount of adsorbate adsorbed at time t (mg.g^{-1}), q_e is the amount of adsorbate adsorbed at equilibrium (mg.g^{-1}), and k_f is the rate constant of the pseudo-first-order adsorption (min^{-1}).

The pseudo-second-order kinetic model assumes that the rate of adsorption is proportional to the square of the number of unoccupied sites [86–88,93]. It is described by the equation 5:

$$q_t = \frac{k_s \cdot q_e^2 \cdot t}{1 + q_e \cdot k_s \cdot t} \quad \text{(Eq. 5)}$$

where k_s is the rate constant of the pseudo-second-order adsorption (g.mg^{-1}.min^{-1}).

The Elovich, the Weber-Morris intra-particle diffusion, and the Avrami kinetic models offer additional advanced ways to model the experimental data obtained from the adsorption assays but where not applied in the studies present in this review. The Elovich kinetic model describes the kinetics of chemisorption processes, particularly for systems with heterogeneous surfaces [94,95]. It is described by the equation 6:

$$\frac{dq_t}{dt} = \alpha \cdot e(-\beta \cdot q_t) \quad \text{(Eq. 6)}$$

where q_t is the amount of adsorbate adsorbed at time t (mg.g^{-1}), and α (mg.g^{-1}.min^{-1}) and β (g.mg^{-1}) are constants.

The Weber-Morris intra-particle diffusion model is used to identify the rate-controlling steps in the adsorption process by considering intra-particle diffusion [96,97]. It is described by the equation 7:

$$q_t = k_{id} \cdot t^{0.5} + C \quad \text{(Eq. 7)}$$

where q_t is the amount of adsorbate adsorbed at time t (mg.g^{-1}), k_{id} (mg.g^{-1}.min$^{-0.5}$) is the intra-particle diffusion rate constant, and C (mg.g^{-1}) is the intercept, which represents the boundary layer effect.

The Avrami kinetic model describes the kinetics of phase change processes and can be adapted for adsorption kinetics [98]. It is described by the equation 8:

$$q_t = q_{\mathrm{m}} \cdot (1 - e(-k_A \cdot t^n)) \qquad \text{(Eq. 8)}$$

where q_t is the amount of adsorbate adsorbed at time t (mg.g^{-1}), q_m is the maximum adsorption capacity (mg.g^{-1}), k_A (min^{-n}) is the Avrami rate constant, and ^{n} is the Avrami exponent.

1.3.3.3.3 Breakthrough Models

Dynamic adsorption studies normally revolve around column assays and use different models to describe the breakthrough curves and the mass transfer processes. The most commonly used models are the Thomas model, the Yoon-Nelson model, and the Bohart-Adams model. The Thomas model assumes plug flow behaviour in the column and uses pseudo-first-order reaction kinetics to describe the adsorption process [79,99,100]. It is described by the equation 9:

$$\ln\left(\frac{C_0}{C_t} - 1\right) = k_{Th} \cdot q_0 \cdot W - k_{Th} \cdot C_0 \cdot t \qquad \text{(Eq. 9)}$$

where C_0 is the influent adsorbate concentration (mg.L^{-1}), C_t is the effluent adsorbate concentration (mg.L^{-1}) at time t, k_{Th} is the Thomas rate constant (L.mg^{-1}.min^{-1}), k_A is the maximum solid-phase concentration (mg.g^{-1}), and W is the mass of adsorbent (g).

The Yoon-Nelson model simplifies the adsorption process by assuming that the probability of adsorbate breakthrough is proportional to the adsorbed amount [81,101,102]. It is described by the equation 10:

$$\ln\left(\frac{C_t}{C_0 - C_t}\right) = k_{YN} \cdot t - \tau \qquad \text{(Eq. 10)}$$

where C_0 is the influent adsorbate concentration (mg.L^{-1}), C_t is the effluent adsorbate concentration (mg.L^{-1}) at time t, k_{YN} is the rate constant (min^{-1}), and τ is the time required for breakthrough (min).

The Bohart-Adams model assumes that adsorption is controlled by the surface reaction between the adsorbate and adsorbent [81,103,104]. It is described by the equation 11:

$$\ln\left(\frac{C_t}{C_0}\right) = k_{BA} \cdot C_0 \cdot t - k_{BA} \cdot N_0 \cdot Z \qquad \text{(Eq. 11)}$$

where C_t is the effluent adsorbate concentration (mg.L^{-1}) at time t, C_0 is the influent adsorbate concentration (mg.L^{-1}), k_{BA} is the rate constant (L.mg^{-1}.min^{-1}), N_0 is the adsorption capacity per unit of volume (mg.L^{-1}), and Z is the bed depth (cm).

1.3.3.3.4 Model Comparisons and Data Fitting

Table 4 presents the isotherm and kinetic model data that better fitted the experimental data from the works studied in this review.

Table 4 - Kinetic and isotherm model data

Adsorbent	Tested REE	Isotherm Model	Isotherm Constant Value		Kinetic Model	Kinetic Constant Value		Ref.
Functionalized Lignin Activated Carbon	Nd	-	-		PSO	1.14 × 10^{-4}	g.mg^{-1}.min^{-1}	[50]
					IDM	24	mg.g^{-1}.min$^{-1/2}$	
Functionalized Lignin Activated Carbon	Dy				PSO	3.39 × 10^{-4}	g.mg^{-1}.min^{-1}	
Spent Coffee Physical Activated Carbon	Dy	Langmuir	6.42	L.mg^{-1}	PSO	1.017	· 10^{-3}	[51]
Spent Coffee Chemical Activated Carbon			10.50			1.232		
Commercial Activated Carbon	Nd	Langmuir	3.49	L.g^{-3}	PFO	0.138	min^{-1}	[52]
Multi-Wall Carbon Nanotubes from Crystalline Nano Cellulose	Dy	Langmuir	0.64	L.g^{-3}	PSO	0.093	g.mg^{-1}.min^{-1}	[53]
Sawdust Biochar	Nd	Freundlich	-		PSO	0.875	g.mg^{-1}.min^{-1}	[54]
	Sc					2.723		
Commercial Activated Carbon (CAC)	Nd					2.258		
	Sc					13.79		
Carbon Black from Recycled Tires	Nd	Langmuir	18.8	L.mol^{-1}	PSO	0.136	g.mg^{-1}.min^{-1}	[55]
	La		51.4			0.111		
	Ce		30.2			0.516		
	Sm		19.3			0.098		
	Y		6.1			0.107		
Commercial Activated Carbon (CAC)	Nd	Langmuir	-	L.mg^{-1}	PSO	-	g.mg^{-1}.min^{-1}	[56]
Oxidized CAC			-			-		
EDTA Functionalized Oxidized CAC			0.130			0.042		
Oxidized Carbon nanofibers	La	-	-		-	-		[57]
	Eu							

	Gd Yb							
PAN Grafted Carbon Nanotubes-Silica	La Sc Y	Langmuir	-		PSO	-		[58]
Carbon Xerogel-Chitosan Composite	-	Freundlich	25.2	$L.mg^{-1}$	PSO	1.35×10^{-4}	min^{-1}	[59]
Carbon Nanoparticles	Nd La	-	-		-	-		[60]
PAM-Activated Carbon Composite	Nd Ce Gd	-	-		PSO	0.312 0.315 0.147	$g.mg^{-1}.min^{-1}$	[61]
Commercial Activated Carbon	La	Langmuir	0.291	$L.\mu g^{-1}$	PSO	0.776	$10^{-2}.g.\mu g^{-1}.min^{-1}$	[62]
	Yb		0.250			0.126		
	Lu		0.257			0.236		
	Eu		0.378			0.378		
	Y		0.182			0.471		
	Sc		0.330			0.942		
$KMnO_4$ Modified Commercial Activated Carbon	La		1.110			1.560		
	Yb		0.612			1.800		
	Lu		1.780			1.990		
	Eu		1.760			2.410		
	Y		0.601			1.630		
	Sc		1.220			1.900		
Oligo-Grafted Synthetic Mesoporous Carbon	Lu Dy La	-	-		-	-		[63]
Commercial Activated Carbon	Eu	Langmuir	0.398	$L.mg^{-1}$	-	-		[64]
Graphene Oxide Nanosheets			0.185					
Commercial Activated Carbon	Sc	-	-		IDM	0.32	$10^{-2}.g.mg^{-1}.min^{-1}$	[65]
Carbon Nanotubes						0.27		
Graphite Oxide						0.22		
Apricot Stone Char	Eu	Langmuir	-	$L.mg^{-1}$	-	-	$g.mg^{-1}.min^{-1}$	[47]
Activated Carbon (H_3PO_4 activation)			0.034		PSO	0.034		
Activated Carbon (KOH activation)			-		-	-		
Schiff's Base Modified Activated Carbon	La	Langmuir	0.1	$L.mg^{-1}$	PSO	0.004	$g.mg^{-1}.min^{-1}$	[46]
CMK-8 (Ordered Mesoporous Carbon)	Sm	Langmuir	0.480	$L.mg^{-1}$	PSO	368.25	$g.mg^{-1}.min^{-1}$	[45]
Oxidized CMK-8			0.080			2.89		
DGO grafted CMK-8			0.660			9.26		

Spent Tire Rubber Char (A450)	Nd	Langmuir	0.937	L.mg^{-1}	PSO	0.003	g.mg^{-1}.min^{-1}	[38]
	Dy		0.147			0.032		
Spent Tire Rubber Char (B450)	Nd		0.948			0.006		
	Dy		0.232			0.013		
Spent Tire Rubber Char (A900)	Nd		0.763			0.073		
	Dy		0.656			0.049		
Spent Tire Rubber Char (B900)	Nd		0.254			0.020		
	Dy		0.317			0.022		
Commercial Activated Carbon	Nd		0.155			1.070		
	Dy		0.256			0.758		
Mesoporous Carbon	La	-	-		-	-		[47]
	Dy							
	Lu							
Carboxylated Mesoporous Carbon	La							
	Dy							
	Lu							
Soybean Pod Activated Carbon	Ce	Langmuir	0.224	L.mg^{-1}	PSO	0.006	g.mg^{-1}.min^{-1}	[48]
	La		0.226			0.005		
Wood Waste Biochar	Ce	Langmuir	0.660	L.mg^{-1}	PFO	0.037	min^{-1}	[49]

PFO: Pseudo-First-Order, PSO: Pseudo-Second-Order, IDM: Intraparticle Diffusion Model

Many studies, such as those by Alcaraz *et al.* [51], found that the Langmuir isotherm model provided a better fit to their experimental data, suggesting monolayer adsorption on a homogeneous surface. For instance, Alcaraz *et al.* [51] reported high correlation coefficients (R^2) for the Langmuir model, indicating that spent coffee activated carbons absorb REEs in a monolayer fashion. This fit reflects the high adsorption capacities observed for Dy (33.52 and 31.26 mg.g^{-1}).

Conversely, some studies, such as those by Komnitsas *et al.* [54] using sawdust biochar, found that the Freundlich isotherm model better described their adsorption data, indicating adsorption on a heterogeneous surface with varying affinities. This model fit correlates with the lower adsorption capacities (8.0 mg.g^{-1} for Nd and 7.5 mg.g^{-1} for Sc), as it reflects a more diverse range of adsorption sites with differing strengths.

Regarding kinetic models, the pseudo-second-order model generally provided a better fit for the adsorption processes studied, as seen in Table 4. The superior fit of this model suggests that chemisorption, involving valence forces through the sharing or exchange of electrons between adsorbent and adsorbate, is the rate-limiting step. For example, the high adsorption capacities of 335.5 mg.g^{-1} for Nd and 344.6 mg.g^{-1} for Dy on functionalized lignin

activated carbon [50] align well with the pseudo-second-order model, reflecting the strong chemical interactions between the adsorbate and the functionalized adsorbent.

Concerning breakthrough models applied to the adsorption of REEs onto carbon-based materials, no data is available, as the only dynamic study present in this literature review, the one performed by Chen *et al.* [57], did not model the experimental data they obtained in the performed assays.

The fit of these models to experimental data is crucial for understanding the adsorption mechanisms and predicting adsorption performance. Materials that align well with the Langmuir model, such as functionalized lignin-activated carbon and phosphorus-functionalized nanoporous carbon, tend to exhibit high adsorption capacities due to the uniform and high-affinity binding sites. In contrast, materials described by the Freundlich model, like sawdust biochar, demonstrate lower capacities, indicating more variable site affinities and less efficient adsorption.

The use of the pseudo-second-order kinetic model in many studies highlights the importance of chemical interaction in achieving high adsorption capacities. Adsorbents that exhibit strong chemical interactions with REEs, facilitated by functional groups, grafting, or mineral content, tend to show higher adsorption capacities and better fit this kinetic model.

Understanding the models used in batch and dynamic adsorption studies is crucial for interpreting experimental data and optimizing adsorption processes [85,105]. Batch models like Langmuir, Freundlich, and advanced models such as Sips, Elovich, Weber-Morris, and Avrami provide insights into the adsorption capacity and surface characteristics of adsorbents. Kinetic models help in understanding the rate-controlling steps of the adsorption process. Dynamic models, on the other hand, are essential for designing and scaling up adsorption systems for real-world applications. Models like Thomas, Yoon-Nelson, and Bohart-Adams provide valuable information on the breakthrough behaviour and mass transfer processes in fixed-bed columns.

Incorporating both batch and dynamic models in research allows for a comprehensive evaluation of carbon-based adsorbents for REEs' recovery. This approach not only helps in identifying the best adsorbents under controlled conditions but also validates their performance in continuous flow systems, paving the way for practical and scalable adsorption processes. By integrating these models, researchers can develop more efficient and economically viable methods for the recovery of REEs.

1.3.3.4 Post-Adsorption Processes for Rare Earth Elements on Carbon-Based Materials

Following the adsorption of REEs onto carbon-based materials, the most common pathway is desorption assays, which are used to assess the efficiency and feasibility of the recovery process.

Desorption involves the removal of the adsorbed REEs from the carbon materials, typically achieved through chemical treatments or changes in solution conditions such as pH, ionic strength, or temperature [49,106].

For instance, Gad and Awwad conducted desorption studies on Eu using AC, demonstrating that the desorption efficiency is significantly influenced by the choice of desorbing agent and the operational parameters such as pH and contact time [47]. Similarly, Babu *et al.* studied the desorption of REEs on EDTA functionalized ACs to desorb REEs using HCl solutions (0.01 M to 1 M), showcasing the potential for multiple adsorption-desorption cycles without significant loss in capacity [56].

Also, Marwani *et al.* studied the desorption of La using HCl solutions, reporting that higher HCl concentrations would improve the amount of REE desorbed from the carbon materials [46]. Perreault *et al.* evaluated the efficiency of REE desorption using oxalate solutions ($(NH_4)_2C_2O_4$) and found that this method was able to desorb around 80% of the REEs from the carbon material and after 5 cycles, the adsorption efficiency decreased by 10% [45]. Haggag *et al.* investigated seven different chemical compounds (HCl, H_2SO_4, HNO_3, Na_2CO_3, NaCl, Na_2SO_4, and CH_3COONa) for REEs' desorption and their results showed that HCl was the best desorption agent with a REE desorption efficiency of 98.2% [59].

Another pathway for the utilization of carbon-based materials loaded with REEs, at the post-adsorption, is the repurposing of these materials as catalysts for various chemical reactions [107,108]. The unique properties of REEs, such as their redox behaviour and ability to stabilize high oxidation states, make them excellent candidates for catalytic processes [107,108]. For example, Gong *et al.* studied a REE-loaded AC as a catalyst for selective catalytic reduction of NO with NH_3, leveraging the catalytic capabilities of REEs to enhance reaction rates and efficiencies [109]. El-Khouly *et al.* also studied the photocatalytic properties of a REE-loaded AC. This study focused on Ce-loaded peach stone AC as a catalyst for the photodegradation of Maxilon Red dye. The authors reported that the REE-loaded AC improved the catalytic performance owing to its wide band gap energy and redox reactions [110]. Chu *et al.* reported that REE-loaded carbon black was an efficient electrocatalyst for oxygen reduction reaction in proton exchange membrane fuel cells due to their high stability and activity [111].

Carbon materials loaded with REEs can also be utilized in environmental remediation [112]. These materials can serve as adsorbents for further purification of water and air,

capturing additional contaminants through a synergistic adsorption process. The REE-loaded carbon materials, such as those investigated by Yu *et al.*, where a Ce-loaded AC was studied for the removal of arsenate and arsenite from wastewaters, suggest that these materials have the potential to be applied for water decontamination [113].

In summary, after the adsorption of REEs onto carbon-based materials, several post-adsorption processes such as desorption assays, catalytic applications, environmental remediation, and regeneration are employed to maximize the utility and sustainability of the materials. These processes not only enhance the recovery of valuable REEs but also extend the functional lifespan of the carbon-based adsorbents.

1.3.3.5 Future Directions: Synthetic Solutions *versus* Real Leachates

Most studies investigating the adsorption of REEs onto carbon-based materials have utilized synthetic solutions, as evidenced by this literature review, where controlled concentrations of individual REEs or mono-component solutions are prepared in the laboratory. These synthetic solutions provide a simplified and controlled environment that allows researchers to isolate and examine the adsorption capacities, kinetics, and isotherm models of specific adsorbents without interference from other compounds. For example, Saha *et al.* [63], Alcaraz *et al.* [51], and Nogueira *et al.* [38] conducted their experiments using synthetic solutions of Nd and Dy, which helped in precisely determining the adsorption capacities of the functionalized lignin-activated carbon, spent coffee activated carbon, and spent tire chars, respectively.

While synthetic solutions are valuable for fundamental research, they do not fully replicate the complexities of real-world scenarios [27,29,114]. In practical applications, REEs are typically found in mixed waste streams, such as industrial effluents, mining leachates, and electronic waste leachates, which contain a variety of other metals, organic compounds, and competing ions [29,114]. These additional components can significantly influence the adsorption behaviour and efficiency of the adsorbents [38].

To bridge the gap between laboratory research and real-world applications, future studies should focus on evaluating the performance of carbon-based adsorbents using real leachates or mixed solutions containing REEs. Real leachates present a more challenging and realistic environment, where multiple factors such as pH variations, the presence of competing ions, and organic matter can affect the adsorption process. Understanding how these factors impact the adsorption capacities and mechanisms will be crucial for developing effective and scalable technologies for REE recovery.

For instance, real leachates from electronic waste or mining operations typically contain a complex mixture of metals and other contaminants [20,27,32,114]. Adsorbents that

perform well in synthetic solutions might exhibit reduced efficiency or selectivity in such environments. Therefore, it is essential to test these materials in conditions that closely mimic actual waste streams to evaluate their true potential and identify any necessary modifications or enhancements.

Conducting adsorption studies using real leachates will also provide insights into the regeneration and reuse of adsorbents, a critical factor for the economic viability of REE recovery processes. Adsorbents need to maintain high adsorption capacities over multiple cycles of adsorption and desorption in the presence of complex mixtures. Research in this area will help in optimizing the operational parameters and improving the sustainability of the adsorption processes.

The most recent studies on the adsorption of REEs by Saha *et al.* (2023), Pinheiro *et al.* (2023), and Reis *et al.* (2023) applied the produced carbon-based materials in real leachates, underscoring that the application in real leachates is important and indeed a needed process in these types of studies. Saha *et al.* studied the recovery of REEs from coal fly ash leachates (HNO_3 leaching) using a carboxylated mesoporous carbon, achieving 80-90% recovery of sixteen REEs from the coal fly ash leachates, although the REE concentration in the leachates was in the ppb range [66]. Pinheiro *et al.* used soybean pod AC for the recovery of Ce and La from a real phosphogypsum leachate, a waste by-product of phosphate fertilizer or phosphoric acid production. They were able to achieve adsorption capacities of 67.6 and 33.7 $mg.g^{-1}$ for Ce and La respectively on the real leachates [67]. Reis *et al.* also applied their produced biochar for the recovery of REEs from a phosphogypsum leachate, with their wood waste biochar being able to recover 86% of the Ce present in the leachate [68].

In conclusion, while studies using synthetic solutions have provided valuable foundational knowledge, the next step is to focus on real leachates to ensure that the developed adsorption technologies are robust, efficient, and applicable to real-world scenarios. This focus will help in advancing the field towards practical and scalable solutions for the sustainable recovery of REEs from various waste streams.

1.3.3.6 Challenges and Gaps in Current Research

Despite the promising attributes of carbon-based materials for REEs' adsorption, several challenges and gaps remain in current research. One of the primary challenges is the variability in adsorption performance due to differences in the physicochemical properties of the adsorbents. Factors such as surface area, pore size distribution, and the nature and density of functional groups can vary significantly depending on the source material and production methods. This variability complicates the comparison of results across different studies and

makes it difficult to identify the most effective adsorbent materials and optimal production conditions [28,48].

Another significant gap is the limited understanding of the adsorption mechanisms at a molecular level [38,48,115]. While it is known that various functional groups on carbon-based materials interact with REE ions, the precise nature of these interactions and the relative contributions of different mechanisms are not fully elucidated. Advanced analytical techniques and theoretical modelling studies are needed to provide deeper insights into these mechanisms and to guide the design of more effective adsorbents [28].

Moreover, most studies on REE adsorption using carbon-based materials have been conducted under controlled laboratory conditions with synthetic solutions [48]. These conditions often do not accurately reflect the complexity of real-world scenarios, where REEs are present in mixtures with other metals and organic compounds, and where pH, temperature, and ionic strength can vary widely. Consequently, there is a scarcity of research involving real e-waste leachates or industrial effluents, which limits the practical applicability of the findings. Addressing this gap requires more field studies and pilot-scale experiments to validate the performance of carbon-based adsorbents in diverse and realistic environments for REEs' adsorption.

Finally, the economic feasibility and environmental impact of using carbon-based materials for REEs' recovery need to be assessed comprehensively [29,115]. While these materials are generally low-cost and sustainable, the costs associated with their production, regeneration, and disposal, as well as their life cycle environmental impacts, must be considered. Future research should focus on developing integrated processes that combine REEs' recovery with other waste treatment or resource recovery operations to enhance overall sustainability and economic viability [38,114].

By addressing these challenges and gaps, future studies can advance the development of carbon-based materials as efficient, scalable, and sustainable solutions for the recovery of REEs, contributing to the secure supply of these critical materials and the advancement of green technologies.

1.3.3.7 Conclusions on Rare Earth Elements Adsorption Using Carbon-Based Materials

The adsorption of rare earth elements onto carbon-based materials offers a promising pathway for the recovery and recycling of these critical resources. Through this literature review, it is evident that various types of activated carbons, biochars, and simpler carbon materials have demonstrated significant potential in adsorbing REEs from aqueous solutions. The high adsorption capacities reported for functionalized lignin-activated carbon and spent coffee-

activated carbon highlight the effectiveness of utilizing waste-derived materials and functionalization techniques to enhance adsorption performance.

While synthetic solutions have provided valuable insights into the adsorption capacities and mechanisms, it is crucial for future studies to test these materials with real leachates. Real-world applications involve complex mixtures with competing ions and contaminants, which can significantly influence adsorption efficiency. Understanding how these carbon-based adsorbents perform in such environments will be essential for optimizing their use in industrial applications and ensuring their practical applicability.

The literature review also underscores the importance of employing various adsorption isotherm and kinetic models to analyse adsorption behaviour. Models such as the Langmuir and Freundlich isotherms, along with pseudo-first-order and pseudo-second-order kinetics, have been instrumental in elucidating the adsorption mechanisms and fitting the experimental data. These models not only help in understanding the interactions between adsorbents and adsorbates but also in predicting the performance of the adsorbents in different conditions.

Given the high supply risk and the critical importance of REEs in modern technology, developing efficient and sustainable methods for their recovery is imperative. The use of more readily available and cost-effective carbon materials, as opposed to complex nanomaterials, aligns well with the objectives of resource recovery and sustainability. These materials offer a practical and scalable solution, making them suitable for broader industrial applications.

The integration of carbon-based adsorbents into the recovery process of REEs supports the principles of a circular economy, where materials are reused, recycled, and recovered to create a closed-loop system. By focusing on functionalized and waste-derived carbons, researchers can develop more sustainable and economically viable solutions. This not only addresses the supply risks associated with REEs but also promotes the efficient use of resources, reducing waste and environmental impact. In doing so, we can support the transition to a low-carbon and high-technology economy that is resilient and sustainable.

In conclusion, advancing the research on carbon-based adsorbents for REE recovery, particularly in the context of real leachates and industrial waste streams, will be crucial for addressing the supply risks associated with these elements. By aligning these efforts with the principles of a circular economy, we can ensure a more sustainable and resilient supply chain for REEs, contributing to a more sustainable future.

1.3.4 Photocatalysis for H_2 Production

Photocatalysis has recently emerged as a promising and sustainable pathway for hydrogen (H_2) production, revealing itself as a process crucial for addressing both energy generation and environmental sustainability. As a clean energy carrier, hydrogen holds significant potential in a myriad of applications, including fuel cells and energy storage systems, which are vital for the transition to a low-carbon economy. The development of sustainable hydrogen production technologies is therefore critical in reducing dependency on fossil fuels and mitigating climate change. Recent research efforts have focused on enhancing the efficiency of photocatalysts by exploring a variety of materials and compounds, including carbon-based materials and rare earth elements, which have shown considerable promise in improving photocatalytic performances [116–121].

Carbon-based materials, recognized for their high surface area, chemical stability, and superior electron conductivity, have been identified as potential photocatalyst carriers, as their integration into photocatalytic systems can significantly enhance H_2 production efficiency [122]. The roles that carbon-based materials play in photocatalytic systems are: (i) their high surface area awards the system with a greater ability to adsorb compounds in solution, leading to higher concentrations on the surface of the photocatalyst, which is crucial for improving photocatalytic reaction rates; (ii) the intermediate products of these reactions can be adsorbed by the carbon-based materials, facilitating successive degradation cycles; (iii) the combination of carbon-based materials with photocatalysts can suppress the recombination of photogenerated electron-hole pairs, resulting in enhanced activity of these photocatalytic systems [123,124].

Known for their unique electronic and catalytic properties, REEs have also been investigated for their role in enhancing photocatalytic systems. Their inclusion can improve light absorption, charge separation, and overall catalytic efficiency. REEs are considered excellent contenders for photocatalysts due to their unique electronic structures, which allow them to absorb and utilize a wide range of light wavelengths, including visible light, more effectively than many other materials. Their f-orbitals configuration enables strong light absorption and provide numerous electronic states that can promote efficient charge separation and transfer processes, crucial for effective photocatalysis. Additionally, REEs can be easily incorporated into various matrices, such as carbon-based materials, enhancing the overall photocatalytic activity by modifying the band gap and improving the material's ability to generate reactive species under light irradiation. Their chemical stability and resistance to photodegradation also makes them durable, long-lasting photocatalysts capable of maintaining performance over extended cycles, which is essential for practical applications.

These attributes collectively make REEs novel and highly promising catalysts for advancing the efficiency and effectiveness of photocatalytic processes [125,126].

In photocatalytic H_2 production assays, sacrificial agents are often employed to boost reaction efficiency by preventing the recombination of photogenerated electron-hole pairs, thus increasing hydrogen yield. The use of Na_2S and Na_2SO_3 mixtures as sacrificial agents in photocatalytic hydrogen production is widely recognized for its effectiveness in enhancing the overall efficiency of the process. These compounds act as electron donors, preventing the recombination of photogenerated electron-hole pairs by readily donating electrons to the photocatalyst. This helps to maintain a continuous flow of electrons, increasing the production of hydrogen. Na_2S and Na_2SO_3 are particularly advantageous because they form a redox couple that efficiently scavenges holes, ensuring that the electrons are available for the reduction reactions necessary for hydrogen evolution. Additionally, this mixture is relatively stable under photocatalytic conditions and does not degrade the photocatalyst, making it a reliable choice for sustaining long-term photocatalytic reactions. Their use is especially common in systems where other sacrificial agents might lead to photocatalyst deactivation or where enhanced reaction kinetics are required to maximize hydrogen output. The selection of sacrificial agents is critical, as it directly impacts reaction kinetics and overall system efficiency, making it an essential factor in optimizing H_2 production processes. [127,128]

The advancement of photocatalysts, particularly those based on carbon materials and rare earth elements, represents significant progress in hydrogen production technology. These processes also enable a novel and promising pathway for the application and further valorisation of carbon materials after the adsorption of REEs. These developments are crucial for advancing sustainable hydrogen production, which is essential for reducing dependence on fossil fuels and facilitating the transition to a clean energy economy. Future research will be vital in integrating these materials into highly efficient systems that fully harness the potential of photocatalysis in addressing global energy challenges.

2

METHODS AND METHODOLOGY

This section outlines the experimental procedures and methodologies employed in this research to achieve the dual objectives of producing optimized porous carbons from spent tyre rubber and recovering REEs from NdFeB magnets. The methodologies are designed to systematically investigate the pyrolysis of spent tyres, the activation of resulting chars, and the subsequent adsorption processes for REE recovery. Detailed descriptions of sample preparation, experimental setups, and analytical techniques are provided to ensure reproducibility and to establish a solid foundation for interpreting the results presented in later sections.

Part of this section was published, partially or completely, in the following scientific publications:

- M. Nogueira, I. Matos, M. Bernardo, L. Tarelho, A.M. Ferraria, A.M.B. Rego, I. Fonseca., and N. Lapa; Recovery of rare earth elements (Nd^{3+} and Dy^{3+}) by using carbon-based adsorbents from spent tire rubber; *Waste Management*; 2024; doi: 10.1016/j.wasman.2023.12.025
- M. Nogueira, I. Matos, M. Bernardo, F. Pinto, I. Fonseca., and N. Lapa; Recovery of Nd^{3+} and Dy^{3+} from E-Waste using Adsorbents from Spent Tyre Rubbers: Batch and Column Dynamic Assays; *Molecules*; 2024; doi: 10.3390/molecules30010092
- Bernardo M., Lapa N., Pinto F., Nogueira M., Matos I., Ventura M., Ferraria A.M., do Rego A.M.B., Fonseca I.M. (2023) Valorisation of spent tire rubber as carbon adsorbents for Pb(II) and W(VI) in the framework of a Circular Economy. *Environmental Science and Pollution Research*, 30 (30), 74820 – 74837. DOI: https://doi.org/10.1007/s11356-023-27689-5

2.1 Rubber Samples

The STR samples used in this work were supplied by two different companies that provide recycling services for end-of-life (EoL) tires. Both samples consist solely of the rubber fraction, as the fabric liner and steel reinforcement were removed during the companies' recycling processes. Current EoL tire processing involves the following steps: (i) shredding the EoL tires into smaller fractions, followed by magnetic separation of the metal fraction; (ii) further milling to achieve smaller particle sizes, which facilitates the separation of the tire fabric liner from the rubber fraction. Textile fibre liners are typically lighter than STR, allowing for separation using air classifiers or gravity-based separators. These devices blow air through the material, causing the lighter fibres to rise and be collected separately. Thus, the rubber samples used in this work were obtained after the final step described above.

Rubber A (particle size range: 0.18 to 0.60 mm) was supplied by Recipneu, Lda, a company that utilizes a cryogenic process for STR recycling, primarily from passenger vehicles. Recipneu, based in Sines, Portugal, has an installed processing capacity of 25,000 tons of EoL tires per year. The company exports 70% of its production, with 90% of its products being used for filling synthetic sports and recreation floors.

Rubber B (particle size range: 0.60 to 0.80 mm) was sourced from Biogoma, Lda, a company specializing in the mechanical recycling of EoL tires from both passenger and heavy vehicles. Biogoma, operating from Santarém, Portugal, has an installed processing capacity of 2.5 tons per hour and has processed 8.8 million tires since the start of operations in 2008. The two products they sell are recycled rubber granulates and recycled rubber powder, mainly used for insulation or flooring purposes.

2.2 Pyrolysis Assays

Two different pyrolysis assays (batch and semi-continuous pyrolysis) were performed under optimized conditions for char production, following previous works [16,129–133] in which products' yields were studied. The aim was to evaluate the influence of both processes on the properties and characteristics of the resulting materials. The chars obtained from both processes were used either as adsorbents or precursors, and as photocatalysts in this thesis.

The nomenclature for the resulting materials followed this rule: the rubber sample used, followed by the carbonization temperature. For example, rubber A carbonized at 405 ^{o}C was designated as A405, while rubber B carbonized at 900 ^{o}C was designated as B900.

2.2.1 Batch Pyrolysis

Batch pyrolysis was performed in a 5.5 L *Parr Instruments* reactor with continuous stirring (Figure 3). After being loaded with 200 g of either rubber sample A or B separately, the reactor was sealed, purged, and pressurized with N_2 at 0.6 MPa. A heating rate of 5 $^{o}C.min^{-1}$ was applied up to a maximum temperature of 405 ^{o}C, with a holding time of 30 minutes. After cooling to room temperature, the solid fraction (chars), which was mixed with the liquid fraction (pyrolysis oils) was decanted. The obtained chars (**A405** and **B405)** were extracted in a Soxhlet apparatus using hexane and acetone sequentially and then washed with deionized water. The char yield after extraction was obtained from equation 12:

$$\eta_{char} = \frac{m_{char}}{m_{tyre}} \cdot 100 \qquad \text{(Eq. 12)}$$

where, η_{char} is the char yield (%), m_{char} is the obtained char mass (g), and m_{tyre} is the initial STR mass (g).

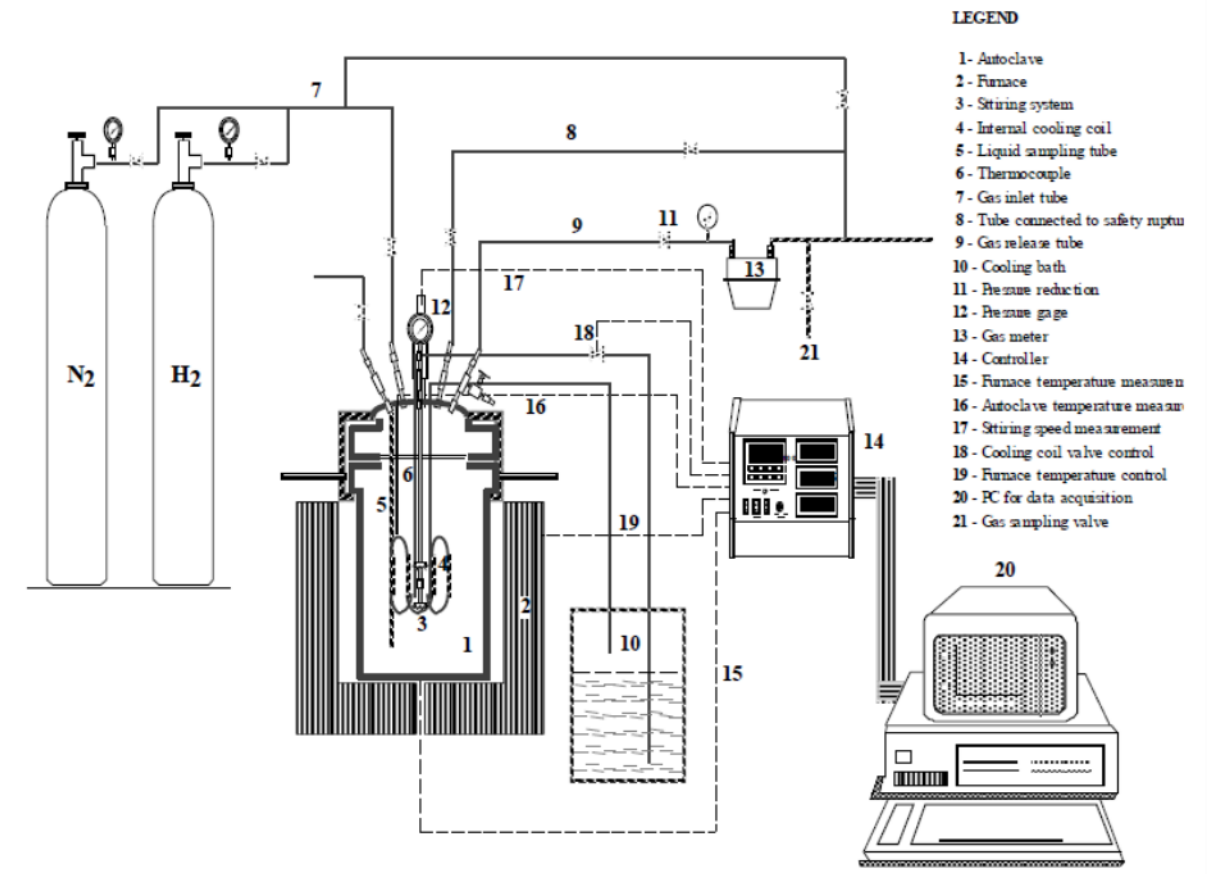

Figure 3 - Schematic representation of the experimental bench-top apparatus with batch pyrolysis reactor

2.2.2 Semi-continuous Pyrolysis

Semi-continuous pyrolysis assays were developed in a bench-scale apparatus (Figure 4) consisting of a horizontal tubular oven with a 35 cm long and 2 cm inner diameter (2 mm wall thickness) quartz reactor. The reactor inlet was connected to a pressurized N_2 feed controlled by a rotameter, while the outlet was connected to 6 gas washing bottles in series submerged in an ice bath for pyrolysis oil condensation and collection.

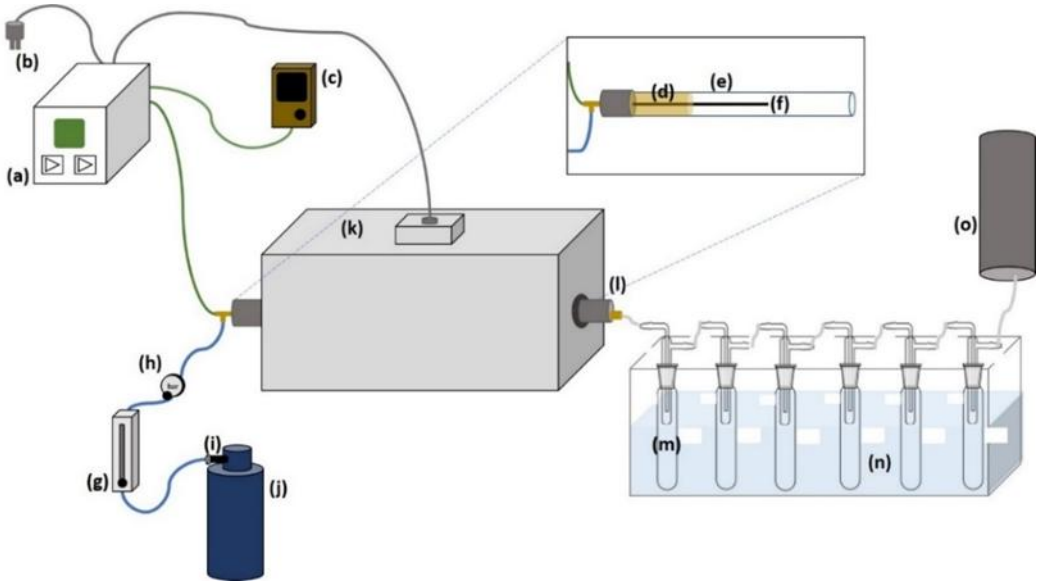

Figure 4 - Schematic representation of the experimental bench-top apparatus with fixed-bed pyrolysis reactor.

(a) temperature controller; (b) power inlet; (c) data logger testo 176T4; (d) ceramic wool; (e) quartz reactor (l = 35 cm, d = 2 cm); (f) thermocouple; (*g*) rotameter; (*h*) valve; (*i*) flowmeter; (*j*) pressurized N_2 bottle; (*k*) tubular oven; (*l*) gas outlet; (*m*) condensers; (*n*) ice bath; (*o*) gas exhaust.

After loading with 10 g of either rubber sample A or B, the reactor was purged with N_2 and then heated up to the desired temperatures at a heating rate of 5 $^{o}C.min^{-1}$. Two process temperatures were studied, 450 ^{o}C and 900 ^{o}C, with a hold time of 30 minutes for both. The temperatures were chosen based on the results of thermogravimetric analysis (TGA) analysis of the rubber samples. A constant N_2 flow of 100 $mL.min^{-1}$ was maintained during all the experiments, to purge the reactor and avoid the entering of air. After the hold time of 30 minutes, the quartz tube reactor was immediately removed from the tubular furnace and left at atmospheric conditions to cool down. The resulting char materials were removed from the reactor and denominated **A450** and **A900** from rubber A obtained at 450^{o}C and 900^{o}C, respectively, and **B450** and **B900** according to the same reasoning. Triplicate assays were performed.

The mass balance of the process is made following equation 13:

$$m_{tire} = m_{char} + m_{oil} + m_{gas} \quad \text{(Eq. 13)}$$

In which m_{tire} is the mass of tire rubber inserted in the pyrolysis reactor, m_{char} is the mass of produced char (solid fraction after pyrolysis), m_{oil} is de mass of produced oil (liquid fraction resulting from pyrolysis vapours condensation), and m_{gas} is the mass of gas produced, which was obtained by difference since it was not measured.

The char, oil and gas yields were determined using equation 14.

$$\eta_X = \frac{m_X}{m_{tire}} \cdot 100 \qquad \text{(Eq. 14)}$$

where X stands for char, oil or gas.

2.3 Activated Carbon Production

Activation of chars was employed to significantly enhance the properties of these adsorbents, focusing on the development of a well-defined pore structure and the improvement of the materials' morphological characteristics. These modifications are crucial for increasing the surface area and accessibility of adsorption sites, which in turn enhances the overall adsorption capacities of the activated carbons. For this work, chars A405 and B405 were selected as precursors for the production of ACs. These chars were subjected to physical activation using CO_2 and chemical activation using potassium carbonate (K_2CO_3), as detailed in the following subsections.

2.3.1 Physical Activation

Physical activation of chars was performed in a bench-scale fluidized bed reactor under CO_2 atmosphere. A selected amount of char was loaded onto the reactor which was then purged with N_2. A heating rate of 5 °C.min^{-1} was applied until 800 °C. At this point, the N_2 flow (150 mL.min^{-1}) was changed to CO_2 (150 mL.min^{-1}), and the sample was activated for 8 hours. The resulting activated chars (AC) were coded **A405-CO2** and **B405-CO2**, according to the char used as precursor.

2.3.2 Chemical Activation

Chemical activation of the chars was performed with K_2CO_3 (1:3 ratio of char to activation agent) following the dry impregnation method. Briefly, 2 g of either char was mixed with 6 g of K_2CO_3 and then loaded into a bench-scale fluidized bed reactor. Under N_2 flow (100 mL.min^{-1}), a heating rate of 5 °C.min^{-1} was applied until the temperature of 800 °C was reached, followed by a holding step of 1 hour. Afterward, the reactor was allowed to cool down to room temperature over 1 hour. The resulting activated carbons (ACs) were then

washed with deionized water until no further changes in pH were observed. The resulting materials were named A405-K2CO3 and B405-K2CO3, according to the char used as precursor.

Unfortunately, setbacks in handling this material led to the discontinuation of these ACs from further assays due to their hazardous nature. During the high-temperature activation process at 800°C under a N_2 atmosphere, the char likely facilitated the reduction of K_2CO_3 to metallic potassium (K). This reduction is plausible given the reducing environment provided by the carbon matrix. Metallic potassium, known for its high reactivity, especially with water, was subsequently present in the ACs. Upon exposure to water during the washing process, the metallic potassium reacted vigorously, producing potassium hydroxide (KOH) and hydrogen gas (H_2). This resulted in a material that displayed dangerous properties, evidenced when mixed with water. The metallic potassium present in the materials reacted violently with water vapours, leading to the spontaneous combustion of the carbon material and a small explosion while the particles were airborne. The rapid generation of hydrogen gas, coupled with its spontaneous ignition in the presence of moisture or water vapor, likely caused the observed spontaneous combustion of the carbon material. This unexpected behaviour aligns with similar observations in the literature where potassium-based activation agents, under high-temperature conditions, form reactive metallic potassium [134,135].

This unexpected behaviour rendered these ACs too dangerous to be handled safely in laboratory assays.

2.4 Material Characterization

The ST rubber samples used in this thesis were characterized by: (i) Elemental analysis; (ii) Ash content; and (iii) Thermogravimetric analysis (TGA).

The physical and textural properties of the chars and ACs were evaluated by: (i) Adsorption of N_2 at 77 K; (ii) Scanning Electron Microscopy-Energy Dispersive Spectroscopy (SEM-EDS); and (iii) Particle size distribution (PSD). Thermal stability was analysed by TGA. The chemical characterization comprised: (i) Elemental analysis; (ii) Ash content; (iii) Determination of mineral content by microwave assisted acidic digestion; (iv) Determination of the pH at point of zero charge (pH_{PZC}); (v) X-ray powder diffraction (XRPD); (vi) X-ray photoelectron spectroscopy; and (vii) Fourier-transform infrared spectroscopy (FTIR).

The magnet samples used in this work were characterized by TGA, and their composition determined by inductively coupled plasma atomic-emission spectroscopy (ICP-AES).

The detailed description of each characterization technique is as follows:

i. Elemental Analysis and Ash Content

Elemental analysis (CNHS) was quantified in a Thermo Finnigan-CE Instruments Flash EA 1112 CHNS Analyzer following the standards ASTM D5373 (C, H, N) and ASTM D4239 (S).

Ash content was determined by the gravimetric method. The residue obtained after combustion at 750 ^{o}C (5 °C min^{-1}), for 3 h in a muffle furnace was considered to be the ashes.

ii. Mineral Content

Mineral content was determined in two steps following standard EN-15290 [136] : (i) microwave-assisted acid digestion (Milestone Ethos 1600 Microwave Labstation) with 3 mL H_2O_2 (30 % v/v), 8 mL HNO_3 (65% v/v) and 2 mL HF (40% v/v), followed by a neutralization step with 20 mL of H_3BO_3 (4% w/v).; (ii) quantification of metals and metalloids on the acidic eluates by inductively coupled plasma atomic-emission spectroscopy (ICP-AES) (Horiba Jobin-Yvon Ultima).

iii. Thermogravimetric Analysis (TGA)

For the rubber samples, chars and activated chars, TGA was performed in a Setaram Labsys instrument, EVO model, with a 20 $cm^3.min^{-1}$ Argon flow and a heating rate of 5 ^{o}C.min^{-1} up to 900 °C. For the magnet samples, the same apparatus was used, but the maximum temperature was 1000 °C and atmospheric air was used.

iv. pH at Point of Zero Charge (pH_{PZC})

The pH at the point of zero charge was calculated by the point drift method [137]: (i) 0.1 M NaCl solutions with pH values between 2 and 12 were prepared (NaOH and HCl were used for pH adjustments); (ii) 0.1 g of either char or AC was added to the previous solutions; (iii) the solutions were then stirred at 300 rpm for 24 h; (iv) The solutions were filtered and the final pH of each was measured. The pH_{PZC} value of each material corresponds to the plateau of the curve pH_{final} *vs* $pH_{initial}$.

v. Textural Analysis

To evaluate the textural properties of the carbon samples, N_2 adsorption-desorption isotherms at 77 K were acquired and the following parameters were quantified: (i) Apparent surface area (S_{BET}) by using Brunauer–Emmett–Teller (BET) equation; (ii) Total pore volume (V_{total}) determined by the amount of nitrogen adsorbed at the relative pressure P/P_o = 0.99; (iii) Micropore volume (V_{micro}) using the t-plot method; (iv) and Mesopore volume (V_{meso}) by the difference between V_{total} and V_{micro}.

vi. Scanning Electron Microscopy-Energy Dispersive Spectroscopy (SEM-EDS)

Surface structure and morphology were analysed by SEM-EDS using JEOL 7001F with Oxford light elements EDS detector and EBSD detector equipped with a Field Emission Gun with Schottky emission equipped with secondary and backscattered electron detectors.

vii. X-Ray Powder Diffraction (XRPD)

The XRPD diffractograms were acquired using a benchtop x-ray diffractometer (Rigaku MiniFlex II) with a Cu X-ray tube (30 kV/15 mA) by continuous scanning from 15° to 80° (2θ) with a step size of 0.01° and a scan speed of $2°.min^{-1}$.

viii. Particle Size Distribution (PSD)

PSD was determined using a Retsch AS 200 Digit vibratory shaker, using sieves with meshes of 50, 100, 200, 500, 1000, and 2000 μm. Each fraction was then weighed on a digital scale (Kern ABS 220-4N) and PSD determined by mass balance.

ix. X-Ray Photoelectron Spectroscopy (XPS)

Char surface was chemically characterized by XPS using a XSAM800 dual anode spectrometer from Kratos, before and after adsorption assays. The Al Kα radiation (hυ=1486.6 eV) was selected.

Spectrometer operation conditions, TOA, pressure and temperature of analysis were as described in Rego *et al.* [138]. Spectra (with a step of 0.1 eV) were collected by the software Vision 2 for Windows, Version 2.2.9 from KRATOS. Data processing was performed using the freeware XPSPeak 4.1. Shirley backgrounds and Gaussian-Lorentzian products were used for curve fitting. No flood gun was used for neutralizing charge accumulation. The shift due to charge accumulation was corrected using, as reference, the binding energy (BE) of a mixture of C 1s sp3 and sp2 set to 284.7 eV [139,140]. For quantification purposes, the sensitivity factors (SF) used were those furnished by the equipment library: 0.278 for C 1s, 0.78 for O 1s, 0.668 for S 2p, 0.328 for Si 2p, 3.726 for Zn $2p_{3/2}$, 2.474 for Dy 4d and 2.457 for Nd 4d.

x. Fourier-Transform Infrared Spectroscopy (FTIR)

FTIR spectra were acquired using a Cary 630 FTIR spectrometer (Agilent Technologies) equipped with diamond attenuated reflectance (ATR) over the range of 400-4000 cm^{-1}, at room temperature, with a resolution of 1 cm^{-1}.

2.5 Magnet Dissolution

For the recovery of REEs from a real waste stream, NdFeB magnets from EoL HDDs were used. As suggested by the literature review, these magnets are promising candidates for WEEE recycling as they are composed by up to 22% of REEs by mass [19,35,36,141–143]. The chosen methods for the dissolution and leaching of the magnets followed optimized process obtained from literature review [114,144–150].

2.5.1 Magnet Samples

The NdFeB magnets used in this research were obtained from end-of-life computer hard disk drives provided by the IT department of NOVA School of Sciences and Technology (NOVA FCT, Portugal). Manual disassembly of the EoL HDDs followed by separation of the magnets from inside the hard disk drives was performed (Figure 5). The magnets were then demagnetized by applying temperature above their curie-point (heating rate of 10 °C.min^{-1} until 400 °C with a hold time of 1 hour, in an N_2 atmosphere) [151]. Afterwards, they were manually grounded to reduce their particle size. Subsequently, they were roasted to convert the metal species into their oxides. The temperatures and roasting times were based on thermogravimetric analysis (Setaram Labsys EVO). Briefly, 25 g of magnets were heated up until 800 °C, at a heating rate of 10 °C.min^{-1}, and held for 3 hours. This process was performed in atmospheric air. After roasting, the magnets registered a 12.3% increase in mass due to oxide formation. The roasting processes is crucial as it alters the chemical structure of the magnets, making the REEs more accessible and easier to extract. The roasting process converts the neodymium and other rare earths into oxides, which are more soluble in acidic solutions, thus enhancing the efficiency of subsequent leaching and dissolution steps.

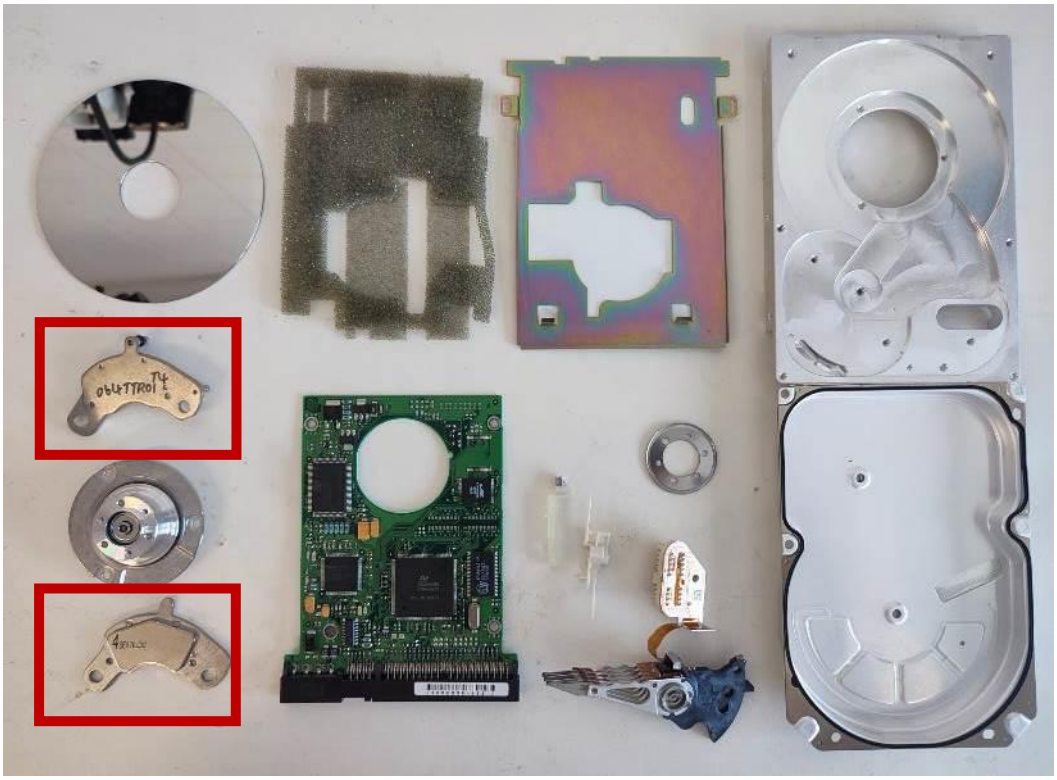

Figure 5 - Disassembled EoL HDDs; NdFeB magnets highlighted by red rectangles

2.5.2 Magnet Leaching

Magnet leaching was performed in a two-neck round bottom flask with reflux, inside a silicon bath with temperature control and magnetic stirring. Two different leaching assays were performed:

(i) *Aqua regia* leaching until full dissolution of the magnet was observed, to acquire the full composition of the material. 100 mg of powdered magnets were inserted into the flask and 60 mL of *aqua regia* (HNO_3:HCl = 1:3 m/m) (HNO_3 65% and HCl 37%) was added. The mixture was then heated at 60 °C until complete dissolution of the magnet (40 hours);

(ii) HNO_3 3M leaching for a set time to emulate a less demanding process in terms of energy, time, and acid. Briefly, 100 mg of powdered magnets were inserted into the flask and 60 mL of HNO_3 3M was added. The mixture was then heated at 60 °C for 6 h. Afterwards, the solution was filtered using ashless MCE membranes (0.22 µm). The concentrations of Al, B, Co, Dy, Fe, Nd, Ni, and Pr in both leachates were determined by ICP-AES.

2.6 Adsorption Assays

For the evaluation of potential REE recovery using the chars and ACs produced in this work, adsorption studies with Nd^{3+} and Dy^{3+} were conducted. These studies began with single-component, synthetic solution batch assays, progressed to multi-component studies, and ultimately developed into dynamic fixed-bed column studies. Finally, to assess the performance of these adsorbents in real-life scenarios, the adsorption of REEs from NdFeB magnet leachates was investigated.

Chars A405, A450, A900, B405, B450, and B900, as well as ACs A405-CO2 and B405-CO2, were studied under batch conditions using Nd^{3+}/Dy^{3+} synthetic solutions. Initially, single-component studies were conducted using either Nd^{3+} or Dy^{3+}, followed by multi-component studies with both REEs present.

AC B405-CO2, which demonstrated superior adsorptive performance, was then selected for further studies in dynamic fixed-bed column assays. These studies began with single-component assays using synthetic solutions and advanced to multi-component assays. The culmination of this work was the successful evaluation of AC B405-CO2 with real magnet leachates, representing a significant advancement in the application of these materials for REE recovery.

A commercial activated carbon (CAC) was used for benchmarking purposes.

2.6.1 Batch Adsorption

2.6.1.1 Nd^{3+} and Dy^{3+} synthetic solutions

Nd^{3+} stock solution (1000 $mg.L^{-1}$) was prepared by dissolution of Neodymium(III) nitrate hexahydrate salts ($Nd(NO_3)_3 \cdot 6H_2O$ 99.9% purity, Sigma-Aldrich) in ultrapure water (Millipore, Milli Q Academic). Dy^{3+} stock solution (1000 $mg.L^{-1}$) was prepared using Dysprosium(III) nitrate hydrate salts ($Dy(NO_3)_3 \cdot xH_2O$ 99.9% purity, Sigma-Aldrich) in ultrapure water. Lower concentrations were obtained by diluting the stock solutions as needed with ultrapure water.

2.6.1.2 Single component batch adsorption assays

All Nd^{3+} and Dy^{3+} individual adsorption assays were performed in batch conditions, in 20 mL sealed vials, on a magnetic stirrer (Velp Scientifica 15-point magnetic multi-stirrer) at 300 rpm, and temperature of 25±1 ^{o}C. The solutions were vacuum filtered using 0.22 µm mixed cellulose

esters (MCE) membranes. The final pH was registered using a Hanna Edge pH sensor. Nd^{3+} and Dy^{3+} concentrations were determined by ICP-AES.

Nd^{3+} and Dy^{3+} recovery efficiency, η (%), and char uptake capacity, q_{exp} (mg.g^{-1}), were calculated using equations 15 and 16, respectively:

$$\eta = \frac{(C_0 - C_f)}{C_0} \cdot 100 \quad \text{(Eq. 15)}$$

$$q_{exp} = \frac{(C_0 - C_f)}{m} \cdot V \quad \text{(Eq. 16)}$$

where C_0 is the initial Nd^{3+} or Dy^{3+} concentrations (mg.L^{-1}), C_f is the final Nd^{3+} or Dy^{3+} concentrations (mg.L^{-1}), m is the char mass (g), and V is the volume of either Nd^{3+} or Dy^{3+} solution (L).

2.6.1.3 Kinetic study

The experimental conditions for the kinetic study were the same for both Nd^{3+} and Dy^{3+} and were as follows:

(i) Initial Nd^{3+} or Dy^{3+} concentration: 100 mg.L^{-1};
(ii) Adsorbent/Solution ratio (Solid/liquid ratio): 5 or 2 g.L^{-1};
(iii) Contact time: between 0.08 (5 minutes) and 72 hours;
(iv) Agitation: 300 rpm in a magnetic stirrer.

The experimental results were modelled through pseudo-first-order [93] (Eq. 17) and pseudo-second-order kinetic models [93] (Eq. 18).

$$q_t = q_e \cdot \left[1 - e^{-k_f \cdot t}\right] \quad \text{(Eq. 17)}$$

$$q_t = \frac{k_s \cdot q_e^2 \cdot t}{1 + q_e \cdot k_s \cdot t} \quad \text{(Eq. 18)}$$

where q_t is the uptake capacity of Nd^{3+} or Dy^{3+} in time t (mg.g^{-1}), q_e is the uptake capacity in equilibrium (mg.g^{-1}), k_f is the pseudo-first-order constant (h^{-1}), k_s is the pseudo-second order constant (g.mg^{-1}.h^{-1}), and t is the contact time (h).

2.6.1.4 Equilibrium studies – Adsorption isotherms

To acquire the adsorption isotherms, the following experimental conditions were used:

(i) Initial concentrations: 10 - 500 mg.L^{-1};

(ii) S/L ratios: 2 and 5 g.L^{-1};

(iii) Contact time: 72 h;

(iv) Agitation: 300 rpm in a magnetic stirrer

The acquired data were fitted to Langmuir's model [89] (Eq. 19) and Freundlich's model [90] (Eq. 20):

$$q_e = \frac{q_m \cdot K_L \cdot C_e}{1 + b \cdot C_e} \quad \text{(Eq. 19)}$$

$$q_e = K_F \cdot C_e^{1/n} \quad \text{(Eq. 20)}$$

where q_e is the Nd^{3+} or Dy^{3+} uptake capacity in equilibrium (mg.g^{-1}), q_m is the monolayer uptake capacity (mg.g^{-1}), K_L is the Langmuir's constant (L mg^{-1}), C_e is the Nd^{3+} or Dy^{3+} concentration in equilibrium (mg.L^{-1}), K_F is the Freundlich's constant which represents the relative uptake capacity ((mg.g^{-1})(mg.L^{-1})^n), and n is the adsorption intensity (dimensionless).

2.6.1.5 Modelling

The kinetic and adsorption isotherm data were fitted to the chosen models by using the SOLVER function of MS EXCEL. The adjustments were performed through the minimization of the sum of least squares (Eq. 21):

$$\sum Least\ squares = \sum (q_{exp} - q_{calc})^2 \quad \text{(Eq. 21)}$$

where q_{exp} is the experimental Nd^{3+} or Dy^{3+} uptake capacity (mg.g^{-1}) and q_{calc} is the modelled Nd^{3+} or Dy^{3+} uptake capacity (mg.g^{-1}).

2.6.1.6 Multi component batch adsorption assays

The char with the best performance on the single component adsorption studies was selected to be tested with Nd/Dy binary mixtures, by using the optimized adsorbent dosage and equilibrium time. The Nd:Dy concentrations ratio studied were: 100:100, 50:50, 100:50, 100:25,

25:100 and 50:100. Uptake capacities obtained in these studies were compared with the ones obtained in the single component studies.

2.6.1.7 Ionic Exchange Assays

To assess if ion exchange mechanism had a role in the removal of Nd^{3+} and Dy^{3+}, the release of Ca, Fe, Mg, and Zn ions from A450 and A900 chars was determined after single adsorption assays. These tests were performed with 20 mg of A450 char and 50 mg of A900 chars, mixed for 72 h with 10 mL of Nd and Dy solutions with a concentration of 100 $mg.L^{-1}$. A blank test with the chars and ultra-pure water was performed. Cation concentrations were determined by ICP-AES.

2.6.2 Dynamic Adsorption Assays

Building on the insights gained from batch adsorption assays, which established the equilibrium behaviour of Nd and Dy adsorption onto porous carbons, this section advances the study to dynamic adsorption assays. Unlike batch assays, dynamic systems better simulate the continuous flow conditions typical of industrial processes. This section focuses on evaluating the performance and breakthrough characteristics of the adsorbent B405-CO2 under these more realistic conditions, providing critical data for their potential application in the recovery of rare earth elements.

The solution containing the adsorbate was introduced into the fixed bed column (height: 10.0 cm; diameter: 0.5 cm) via an ascending flow. A peristaltic pump (Heidolph pumpdrive 5001) with multichannel was used to pump the solution into the fixed bed column. The adsorbent was fixed by placing layers of HCl-washed silica sand and polyurethane foam at both the top and bottom. Samples were collected over time from the top end of the column. Control assays were performed to ensure that the capping materials did not adsorb any of the REEs. The performance of the adsorbents was evaluated by studying the effluent concentration over time. The resulting data was represented in a breakthrough curve, expressed as the ratio of C_t/C_0, representing the ratio of the adsorbate concentration in the outflow (C_t) and inflow (C_0) of the column, over time. The following parameters were analysed for each assay:

(i) Breakthrough time (t_b) – The time taken (min) for the adsorbate concentration in the outflow to reach 5% of the inflow concentration ($C_t/C_0 = 0.05$).

(ii) Saturation time (t_s) – Defined as the duration (min) when the concentration of the adsorbate in the outflow equals 95% of its concentration in the inflow ($C_t/C_0 = 0.95$).

(iii) Adsorbate mass retained (m_{ads}) – The total mass (mg) of adsorbate retained up to the saturation time is reached, which is calculated by using Eq. 22:

$$m_{ads} = \frac{Q \cdot C_0}{1000} \cdot \int_0^{t_s} \left(1 - \frac{C_t}{C_0}\right) dt \quad \text{(Eq. 22)}$$

where Q signifies the flow rate of adsorbate's solution (mL.min^{-1}), C_0 represents the initial concentration of the adsorbate in the inflowing solution (mg.L^{-1}), and C_t stands for the concentration of the adsorbate in the outflow at time t (mg.L^{-1}).

(iv) Removal efficiency (η) – The ratio between the total mass of adsorbate retained by the adsorbent and the total mass of adsorbate inserted into the column, expressed as a percentage (Eq. 23):

$$\eta = \frac{m_{ads}}{m_{total}} \cdot 100 \quad \text{(Eq. 23)}$$

where m_{total} is the total mass (mg) of adsorbate inserted into the column (Eq. 24) and m_{ads} has the same meaning and unit as for the previous equation (Eq. 22).

$$m_{total} = \frac{Q \cdot C_0 \cdot t_s}{1000} \quad \text{(Eq. 24)}$$

where the variables have the same meaning and units as for the previous equations.

(v) Total uptake capacity (q_{total}) – Refers to the maximum amount of adsorbate removed by the adsorbent inside the column, within the saturation time (t_s) (Eq. 25):

$$q_{total} = \frac{m_{ads}}{m_{AC}} \quad \text{(Eq. 25)}$$

where m_{AC} is the total mass of adsorbent (mg) inside the column.

2.6.2.1 Mono-component dynamic adsorption assays

Mono-component dynamic adsorption assays were performed with either Nd^{3+} or Dy^{3+} synthetic solutions, using B405-CO2 or CAC as adsorbents. The experimental conditions were as follows:

(i) 100 mg of adsorbent (m_{AC});
(ii) Flow rate (Q) of 1.5 mL.min^{-1};
(iii) Running time (t) of 180 minutes;
(iv) Temperature of 23 °C;
(v) Initial concentrations of Nd^{3+} or Dy^{3+} (C_0) of 10 and 2.5 mg.L^{-1} for B405-CO2 and 2.5 mg.L^{-1} for CAC.

2.6.2.2 Bicomponent dynamic adsorption assays

Bicomponent dynamic adsorption assays were performed using a mixture of both Nd^{3+} and Dy^{3+} synthetic solutions, using B405-CO2 or CAC as adsorbents. The experimental conditions were as follows:

(i) 100 mg of adsorbent (m_{AC});
(ii) Flow rate (Q) of 1.5 mL.min^{-1};
(iii) Running time (t) of 180 minutes;
(iv) Temperature of 23 °C;
(v) Initial concentrations (C_0) of both Nd^{3+} and Dy^{3+} (C_{0_Nd}+C_{0_Dy}): 2.5+2.5 and 1.25+1.25 mg.L^{-1}.

2.6.2.3 Real magnet leachate dynamic adsorption assays

To evaluate the adsorbents performance on real leachate, the HNO_3 3M magnet leachate (Section 2.5.2) was used. Before the dynamic adsorption assays, the leachate was treated as follows:

(i) pH adjustment to 5.1 with NaOH 6M to precipitate iron;
(ii) Filtration using ashless MCE membranes (0.22 µm);
(iii) Dilution with Milli-Q water until the desired concentration of 1.25 mg Nd^{+3}.L^{-1}.

The experimental conditions used during this assay were the following:

(i) 100 mg of adsorbent (m_{AC});
(ii) Flow rate (Q) of 1.5 mL.min^{-1};
(iii) Running time (t) of 210 minutes;
(iv) Temperature of 23 °C;

(v) Initial concentrations of Nd (C_{0_Nd}) 1.25, Al (C_{0_Al}) 0.02, B (C_{0_B}) 0.13, Co (C_{0_Co}) 0.08, Dy (C_{0_Dy}) 0.10, Fe (C_{0_Fe}) <0.001, Ni (C_{0_Ni}) <0.007, and Pr (C_{0_Pr}) <0.01 mg.L^{-1}.

2.6.2.4 Breakthrough modelling

The breakthrough data was fitted to Thomas' nonlinear model [85] (Eq. 26):

$$\frac{C_t}{C_0} = \frac{1}{1 + e^{\left(k_{th} \cdot q_0 \cdot \frac{m_{AC}}{Q}\right) - (k_{th} \cdot C_0 \cdot t)}} \quad \text{(Eq. 26)}$$

where, C_t (mg.L^{-1}) represents the concentration of the adsorbate in the column outflow at time t (min), while C_0 (mg.L^{-1}) is the concentration of the adsorbate in the column inflow. k_{th} (mL.min^{-1}.mg^{-1}) is the Thomas rate constant, q_0 (mg.g^{-1}) is the maximum uptake capacity of the adsorbent, m_{AC} (g) denotes the mass of the adsorbent in the column, and Q (mL.min^{-1}) is the flow rate of the adsorbate's solution.

The model fitting was performed using the SOLVER plugin for MS Excel using the minimum sum of the least-square method (Eq. 27):

$$Min\left[\sum Least\ squares\right] = Min\left[\sum \left(q_{exp} - q_{teo}\right)^2\right] \quad \text{(Eq. 27)}$$

where q_{exp} is the experimental uptake capacity (mg.g^{-1}) and q_{teo} is the theoretical uptake capacity (mg.g^{-1}) calculated from Thomas' model.

2.7 Photocatalysis for H_2 Production Assays

In this thesis, the investigation of photocatalytic hydrogen production using the produced STR chars and ACs was a logical extension of the efforts to further valorise waste materials and the recovery of REEs.

The decision to explore the photocatalytic properties of the chars and ACs, both pre- and post-REE adsorption, was driven by the presence of semiconductors within the carbon matrix, which were hypothesized to possess photocatalytic properties. Additionally, the observed ability of these adsorbents to immobilize REEs, known for enhancing photocatalytic processes due to their unique electronic configurations and stability, further motivated this investigation. The materials were evaluated for their hydrogen production capabilities to

determine whether their photocatalytic properties could be further valorised post-adsorption, thereby contributing to the circular economy and sustainable energy solutions.

The materials subjected to this evaluation were char B405, AC B405-CO_2, and Nd-loaded char Nd@B405 (char B405 post-Nd adsorption). A custom photocatalytic reactor system was designed specifically for this purpose, with a sodium sulphide/sodium sulphite (Na_2S/Na_2SO_3) mixture selected as the sacrificial solution. This combination was chosen for its proven efficacy in preventing the recombination of photogenerated electron-hole pairs, thereby maximizing hydrogen yield [152–154]. Furthermore, a reference catalyst ZnCdS (Zn:Cd 1:2) was synthesized to benchmark the performance of the produced chars and ACs. This reference photocatalyst was selected due to its well-documented activity in similar photocatalytic systems, providing a reliable standard for comparison [155–158].

The following sections detail the synthesis of the reference catalyst, the preparation of the sacrificial solution, the characterization of the photocatalytic system, and the subsequent photocatalysis assays conducted to assess the hydrogen production potential of the prepared materials.

2.7.1 Catalyst Synthesis

The reference photocatalyst ZnCdS (Zn:Cd 1:2) was synthesized using a co-precipitation method reported in the literature. Zinc nitrate tetrahydrate ($Zn(NO_3)_2 \cdot 4H_2O$) and cadmium nitrate tetrahydrate ($Cd(NO_3)_2 \cdot 4H_2O$) were employed as the precursors for zinc and cadmium, respectively. Sodium sulphide nonahydrate ($Na_2S \cdot 9H_2O$) was used as the sulphide source.

Initially, 0.6028 g (2.31 mmol) of $Zn(NO_3)_2 \cdot 4H_2O$ and 1.43 g (4.62 mmol) of $Cd(NO_3)_2 \cdot 4H_2O$ were dissolved in 40 mL of ultrapure water. The resulting solution was heated to 70°C under constant stirring to ensure complete dissolution and homogeneity. In a separate vessel, 1.66 g (6.9 mmol) of $Na_2S \cdot 9H_2O$ was dissolved in 40 mL of ultrapure water to prepare the sulphide solution. This solution was then added dropwise to the previously prepared metal nitrate solution while maintaining continuous stirring at 70°C. The addition rate was carefully controlled to avoid rapid precipitation and ensure uniform particle formation.

After the complete addition of the sulphide solution, the reaction mixture was maintained at 70°C with continuous stirring for an additional 30 minutes to promote particle growth and crystallization.

The resulting precipitate was collected by filtration and subsequently washed three times with ultrapure water to remove any residual soluble species. The filtered product was then dried overnight at 90°C to obtain the final reference photocatalyst.

2.7.2 Sacrificial Solution

The sacrificial solution used in the photocatalytic H_2 production assays was prepared by dissolving 15.377 g of sodium sulphide (Na_2S) and 22.048 g of sodium sulphite (Na_2SO_3) in 500 mL of ultrapure water, resulting in a 0.35M Na_2SO_3 + 0.25M Na_2S solution.

The solid reagents were weighed, and each compound was added sequentially to a beaker containing ultrapure water. The mixture was then stirred continuously at room temperature until complete dissolution of the salts was achieved, resulting in a clear sacrificial solution.

This solution was freshly prepared prior to each photocatalytic experiment to ensure optimal performance and was stored in a sealed container to prevent any contamination or degradation.

2.7.3 Photocatalysis assays

Photocatalysis assays were performed using char B405, AC B405-CO2, the neodymium loaded char Nd@B405, and the reference catalyst ZnCdS (Zn:Cd) for benchmarking purposes. A custom reactor system adapted from literature [159] was employed (Figure 6), consisting of a glass vessel equipped with a custom-made, two-headed top. The top featured a rubber septa for gas sampling and a connection to a volumetric pipette for measuring gas production by volume displacement.

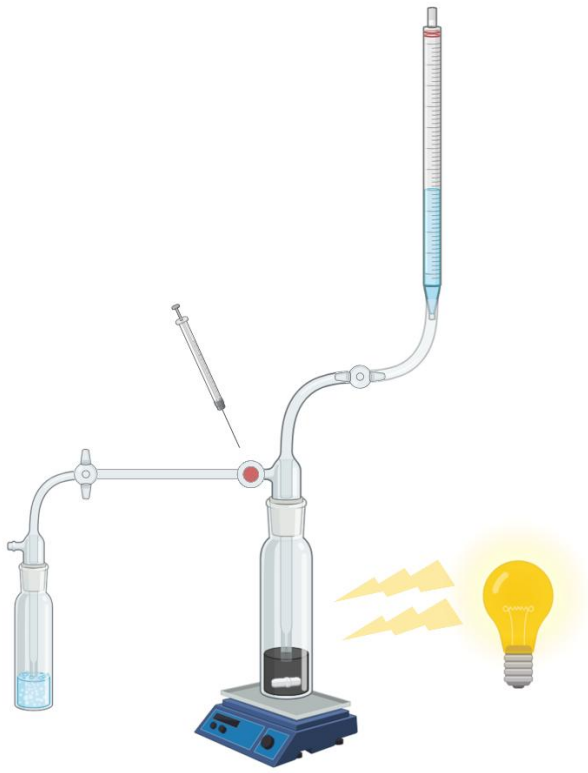

Figure 6 - Schematic of the photocatalytic reactor used in H_2 production assays

Given the finely powdered and hydrophobic nature of the photocatalysts, the catalyst-solution mixture was subjected to ultrasonication in an ultrasound bath for 15 minutes to ensure thorough dispersion. Prior to the initiation of the photocatalytic reaction, the entire reactor system was purged with N_2 gas for 30 minutes to eliminate residual air and oxygen, thereby creating an inert atmosphere. To evaluate the reusability of the photocatalysts, each assay was repeated for three consecutive cycles using the same photocatalyst. After each cycle, the photocatalyst system was stored in the dark, and the assay was repeated under identical conditions the following day. At the conclusion of each assay cycle, the evolved hydrogen was sampled using a gas-tight syringe. The purity of the hydrogen gas was then analysed using a Gas Chromatography-Thermal Conductivity Detector (GC-TCD) system (Thermo Trace CG Ultra) to accurately quantify the hydrogen production and assess its quality.

The operating parameters for the photocatalytic H_2 production assays were as follows:

(i) Photocatalyst mass (m_{CAT}) of 50 mg;
(ii) Sacrificial solution volume (V_{sac}) of 90 mL;
(iii) Run time (t) of 180 minutes;
(iv) Light source was a 300 W Xe lamp;
(v) Three photocatalysis cycles.

2.7.4 Photocatalytic system characterisation

2.7.4.1 Actinometry

An actinometric assay was conducted using potassium ferrioxalate to quantify the light intensity during photocatalytic experiments [160]. A solution of 14.138 g of potassium ferrioxalate was prepared in a 250 mL volumetric flask with the addition of 0.69 mL of concentrated sulfuric acid (H_2SO_4). The solution was then irradiated with a light source for varying durations (0 s, 30 s, 60 s, 90 s, and 120 s).

After irradiation, 1 mL of the irradiated solution was mixed with 1 mL of 1,10-phenanthroline and 0.5 mL of ammonium acetate buffer solution. The formation of the Fe^{2+}-phenanthroline complex was monitored using UV-Vis spectrophotometry by measuring absorbance at 510 nm.

The absorbance data corresponding to the different exposure times were used to calculate the concentration of Fe^{2+}, which was then employed to determine the light intensity during the photocatalytic assays. The quantum yield for the ferrioxalate photoreaction was used to convert the Fe^{2+} concentration to the number of absorbed photons, thereby providing a quantitative measure of the light intensity during the experiments.

2.7.4.2 Diffuse Reflectance and Absorption Spectra

The diffuse reflectance spectra were acquired using a Shimadzu YV-2501PC with an integrating sphere and absorption spectra of the photocatalysts were obtained using a conventional double-beam VARIAN spectrophotometer, model Cary-5000. The measurements were conducted over a wavelength range of 250–800 nm with a 1 nm step size. Due to the highly black nature of the ACs and chars, which exhibit strong light absorption across the visible spectrum, characterizing these materials was challenging.

2.7.5 Modelling

2.7.5.1 Linearized Pseudo-First-Order Kinetic Model

The rate of hydrogen production over time can be modelled using a pseudo-homogeneous pseudo-first-order kinetic approach, where the rate of hydrogen evolution is proportional to the remaining hydrogen production potential [161–166]. The linearized form of the pseudo-first-order kinetic model is described in equation 28:

$$\ln(V_{max} - V_t) = -k_{H1} \cdot t + \ln(V_{max}) \quad \text{(Eq. 28)}$$

where V_t is the volume of hydrogen produced at time t (mL), V_{max} is the maximum possible volume of hydrogen that could be produced (mL), k_{H1} is the first-order rate constant (h^{-1}), and t is the reaction time (hours).

By plotting $\ln(V_{max} - V_t)$ against time t, the rate constant k_{H1} can be determined from the slope of the resulting straight line.

2.7.5.2 Non-Linear Pseudo-First-Order Kinetic Model

The non-linear pseudo-homogeneous pseudo-first-order kinetic model for hydrogen production is given by equation 29:

$$V_t = V_{max} \cdot (1 - e^{-k_{H1} \cdot t}) \quad \text{(Eq. 29)}$$

where V_t is the volume of hydrogen produced at time t (mL), V_{max} is the maximum possible volume of hydrogen that could be produced (mL), k_{H1} is the first-order rate constant (h^{-1}), and t is the reaction time (hours)

This model directly relates the hydrogen volume produced to the reaction time, allowing for the determination of the rate constant k_{H1} through non-linear regression techniques. The rate constant k_{H1} characterizes the speed of the reaction, with higher values indicating faster hydrogen production.

The model fitting was performed using the SOLVER plugin for MS Excel using the minimum sum of the least-square method (Eq. 30):

$$Min\left[\sum Least\ squares\right] = Min\left[\sum \left(V_{exp} - V_{teo}\right)^2\right] \quad \text{(Eq. 30)}$$

where V_{exp} is the experimental produced hydrogen volume (mL) and V_{teo} is the theoretical produced hydrogen volume (mL) calculated from the non-linear first-order kinetic model adjusted for H_2 production.

3

SEMI-CONTINUOUS PYROLYSIS CHARS: SINGLE-COMPONENT AND MULTI-COMPONENT SYNTHETIC BATCH ADSORPTION ASSAYS

Chapter 3 delves into the production and characterization of chars derived from the semi-continuous pyrolysis of spent tyre rubber, focusing on their application in single-component and multi-component batch adsorption assays. The objective was to evaluate the adsorption capacity of these chars for REEs such as neodymium and dysprosium. This chapter discusses the results obtained from the experimental procedures used to produce chars via pyrolysis and explores the performance of these chars in adsorbing REEs under controlled batch conditions. The kinetics and adsorption mechanisms involved in these processes are also examined, providing valuable insights into the adsorption of REEs by these carbon-based materials and laying the foundation for the work developed throughout this thesis. The findings from this chapter offer significant insights into the potential of pyrolysis chars as effective adsorbents in the recovery of valuable materials from waste streams.

Part of this section was published, partially or completely, in the following scientific publications:

- M. Nogueira, I. Matos, M. Bernardo, L. Tarelho, A.M. Ferraria, A.M.B. Rego, I. Fonseca., and N. Lapa; Recovery of rare earth elements (Nd^{3+} and Dy^{3+}) by using carbon-based adsorbents from spent tire rubber; *Waste Management*; 2024; doi: 10.1016/j.wasman.2023.12.025
- Bernardo M., Lapa N., Pinto F., Nogueira M., Matos I., Ventura M., Ferraria A.M., do Rego A.M.B., Fonseca I.M. (2023) Valorisation of spent tire rubber as carbon adsorbents for Pb(II) and W(VI) in the framework of a Circular

Economy. *Environmental Science and Pollution Research*, 30 (30), 74820 – 74837. DOI: https://doi.org/10.1007/s11356-023-27689-5

3.1 Pyrolysis Yields

Two pyrolysis temperatures were studied for each precursor (rubber), 450 ºC and 900 ºC. At the lowest process temperatures, the char yields (Table 5) are slightly higher (39.8 % wt. and 38.5 % wt. for A450 and B450, respectively).

Table 5 - Pyrolysis yields obtained at the two temperatures

Rubber	**T** (°C)	**η** (% wt.)		
		Char	Oil	Gas
A	450	39.8 ± 0.23	51.2 ± 0.77	9.07 ± 0.72
	900	37.5 ± 0.13	52.0 ± 0.89	10.5 ± 0.84
B	450	38.5 ± 0.21	52.4 ± 0.36	9.06 ± 0.50
	900	36.7 ± 0.25	52.7 ± 0.26	10.6 ± 0.46

Increasing the temperature, the char yield decreases for an average value of 37.1 %, oil yield and permanent gas yield increase to an average value of 52.4% and to around 10.5%, respectively. These results were expected since it is known that high process temperatures promote a higher thermochemical decomposition of the raw material, resulting in a higher release of volatile matter that is converted into oils and permanent gases, and consequently the char yield decreases [167–169].

3.2 STR samples and Chars

The rubber precursors were characterized by elemental analysis, ash content, TGA, and mineral content. The obtained chars were additionally characterized through FTIR, XRD, SEM-EDX, pHpzc and N_2 adsorption at 77 K.

Both precursors show a similar behaviour under thermal decomposition (Figure 7), with a sharp mass loss in the range temperature of 250 ºC to 450 ºC, being possible to observe that around 39 % wt. of solid fraction remains at the latter temperature. Above 450 ºC there is no significant mass loss, remaining around 36 % wt. of carbonaceous product at 900 ºC. This

behaviour agrees well with the chars' pyrolysis yields (Table 5). Also, it can be concluded that the origin of the samples does not affect the thermal degradation profile.

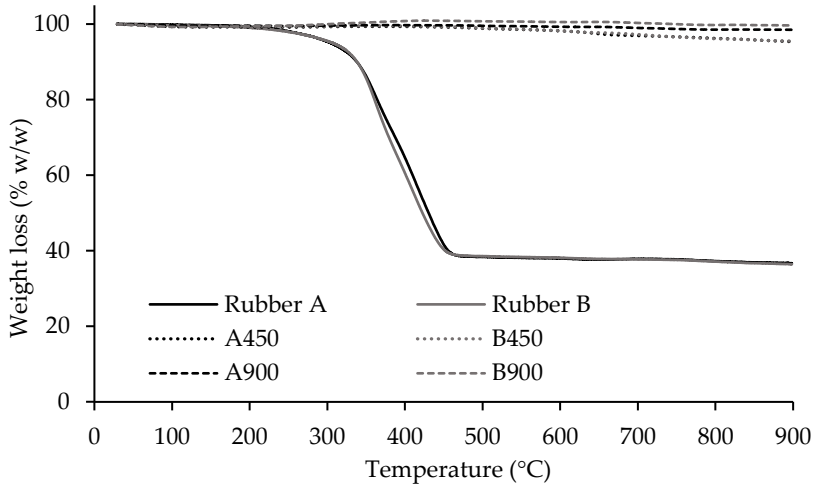

Figure 7 - Thermogravimetric analysis of rubbers A and B and respective char samples produced by pyrolysis

The obtained thermograms reveal a very high thermal stability of the chars produced at 900 ºC. The samples A450 and B450 have a slight weight loss at higher temperatures but are still very stable materials with mass losses lower to 10 % wt. These results confirm the success of the pyrolysis process in removing the volatile compounds present in the rubber precursors.

The elemental analysis (Table 6) of the two precursors shows a very similar composition, presenting a high carbon concentration, and also some sulfur as a result of the rubber vulcanization process [170].

Table 6 - Elemental analysis, ash content and pHpzc of samples (as-received basis)

Sample	C (% w/w)	H (% w/w)	N (% w/w)	S (% w/w)	Ash (% w/w)	pH_{PZC}
Rubber A	79.20	7.07	0.40	1.64	9.50	-
Rubber B	83.39	7.60	0.40	2.04	8.70	-
A450	68.82	0.38	<0.20	2.49	25.9	8.2
B450	75.82	0.42	0.27	3.82	18.4	7.7
A900	80.05	0.13	0.13	2.97	25.1	9.9
B900	75.59	0.13	0.15	3.96	19.2	8.9
CAC	86.3	0.47	<0.20	0.57	5.70	9.1

The resulting chars remain with very high carbon concentration but present a decrease in the nitrogen and hydrogen concentration, corresponding to the thermal decomposition of organic compounds during char formation. The increase in sulfur and ash content is due to a concentration effect promoted by the pyrolysis process, in result of the release of volatile compounds, whereas these compounds are retained in the solid resulting structure. CAC sample presented a much lower ash concentration when compared to the obtained chars, as expected for a commercial activated carbon.

Rubber A is the precursor with the highest ash content and consequently, the resulting chars, A450 and A900, present a higher ash concentration. All the chars as well as the commercial carbon present alkaline behaviour although chars carbonized at 900 ºC show higher pH_{PZC} values than chars obtained at 400 ºC, probably due to the increase of mineral content.

The mineral compositions of the rubbers A and B (Table 7) are very similar, being Zn, Ca, and Fe the major elements since they are present in several vulcanization agents and additives used in the manufacturing of the tyres [170,171]. However, sample B does seem to have higher amounts of Zn and Fe. K, Na, Al, Se, Si, Sn, Cd and Mo were not detected in any of the samples (Table 7), although silica (SiO_2) is commonly used in tires manufacturing.

Table 7 - Mineral concentration of precursor (rubber) samples and respective chars obtained by pyrolysis

(Units: mg g-1; $\bar{X} \pm \sigma$,n=2)

Element	Samples					
	Rubber A	**Rubber B**	**A450**	**B450**	**A900**	**B900**
Zn	29.2 ± 0.19	38.6 ± 5.4	83.9 ± 2.9	116 ± 2.7	50.4 ± 3.5	93.2 ± 6.1
Ca	13.0 ± 3.9	6.38 ± 0.18	28.7 ± 0.7	16.2 ± 0.19	33.0 ± 1.3	17.3 ± 0.8
Fe	2.18 ± 0.55	4.25 ± 0.27	6.08 ± 0.18	11.98 ± 0.82	6.85 ± 0.05	13.3 ± 0.3
Mg	0.815 ± 0.239	0.870 ± 0.105	2.29 ± 0.096	2.47 ± 0.20	2.56 ± 0.17	2.75 ± 0.25
Cu	0.473 ± 0.490	1.02 ± 0.17	0.358 ± 0.025	2.17 ± 0.25	0.748 ± 0.311	2.36 ± 0.08
Ba	0.202 ± 0.215	$<4x10^{-5}$	0.082 ± 0.012	0.002 ± 0.001	$<4x10^{-5}$	0.072 ± 0.102
Pb	0.081 ± 0.027	0.043 ± 0.001	0.112 ± 0.006	0.138 ± 0.014	$<2x10^{-4}$	0.042 ± 0.059
Mn	0.029 ± 0.008	0.025 ± 0.002	0.074 ± 0.008	0.080 ± 0.011	0.080 ± 0.011	0.098 ± 0.008
Ni	0.004 ± 0.000	0.004 ± 0.0001	0.01 ± 0.003	0.022 ± 0.003	0.010 ± 0.003	0.018 ± 0.003
Cr	0.002 ± 0.003	0.006 ± 0.003	0.018 ± 0.003	0.018 ± 0.001	0.012 ± 0.006	0.022 ± 0.008
Ti	0.067 ± 0.009	<0.004	<0.004	0.220 ± 0.175	0.264 ± 0.288	0.318 ± 0.314
K	<0.077	<0.077	<0.077	<0.077	<0.077	<0.077
Na	$<1x10^{-4}$	$<1x10^{-4}$	$<1x10^{-4}$	$<1x10^{-4}$	$<1x10^{-4}$	$<1x10^{-4}$
Al	<0.002	<0.002	<0.002	<0.002	<0.002	<0.002
Se	<0.007	<0.007	<0.007	<0.007	<0.007	<0.007
Si	<0.002	<0.002	<0.002	<0.002	<0.002	<0.002
Sn	<0.001	<0.001	<0.001	<0.001	<0.001	<0.001
Cd	$<4x10^{-4}$	$<4x10^{-4}$	$<4x10^{-4}$	$<4x10^{-4}$	$<4x10^{-4}$	$<4x10^{-4}$
Mo	$<4x10^{-4}$	$<4x10^{-4}$	$<4x10^{-4}$	$<4x10^{-4}$	$<4x10^{-4}$	$<4x10^{-4}$

After pyrolysis, the same elements can be detected in the chars produced, although in higher concentrations due to the concentration effect mentioned above, Zn, Ca, and Fe continuing to be the major contributors.

The chars obtained from precursor B are richer in Zn, making clear the difference already presented between precursors and demonstrating that the source of the spent tires can have an impact on the chemical composition of the obtained chars.

The major elements in the commercial carbon were Si (14.6 ± 0.7 mg g^{-1}), Al (8.78 ± 0.023 mg g^{-1}) and Fe (3.18 ± 0.23 mg g^{-1}) [137].

The textural parameters of the carbon materials were obtained from N_2 adsorption-desorption isotherms (Figure 8). All samples present a similar and low value of surface area (A_{BET}), agreeing with other reported values for this type of materials [172,173]. These results

also agree with the TGA results (Figure 7) that have shown that above 450 °C the release of volatile matter was not significant, thus no further porosity was formed.

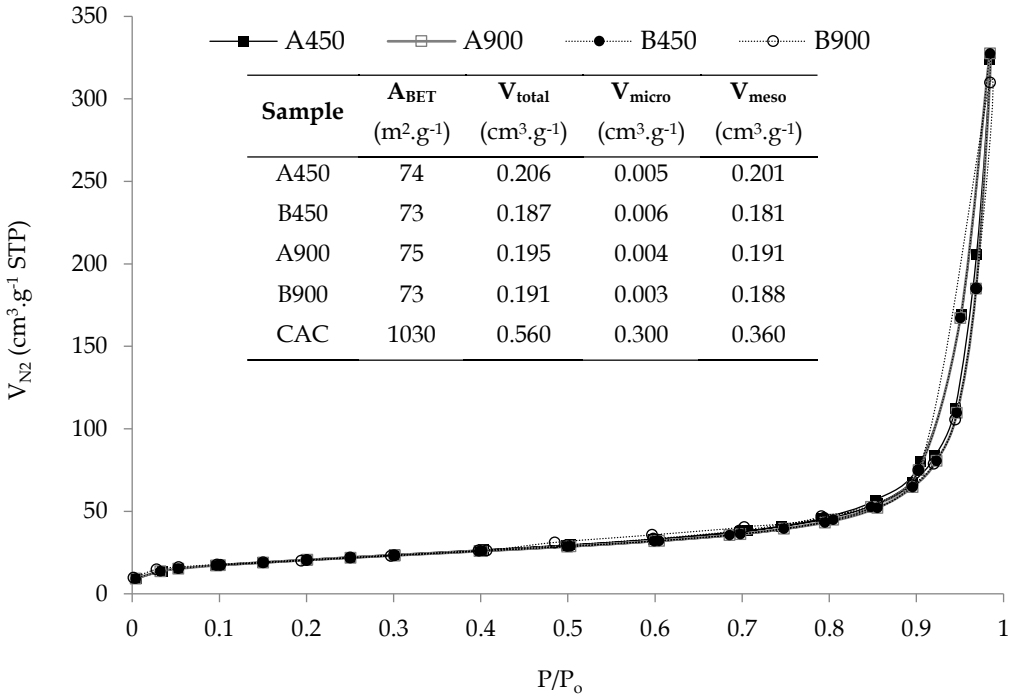

Sample	A_{BET} (m^2.g^{-1})	V_{total} (cm^3.g^{-1})	V_{micro} (cm^3.g^{-1})	V_{meso} (cm^3.g^{-1})
A450	74	0.206	0.005	0.201
B450	73	0.187	0.006	0.181
A900	75	0.195	0.004	0.191
B900	73	0.191	0.003	0.188
CAC	1030	0.560	0.300	0.360

Figure 8 - N_2 adsorption-desorption isotherms of the chars and textural parameters

The chars present a type IV(a) isotherm assigned to mesoporous materials [174]. The commercial carbon CAC has a very high surface area (1030 m²/g) being mainly composed by large micropores and narrow mesopores [137].

Figure 9 presents the XRPD patterns of the produced chars, where it is possible to identify the crystalline mineral phases. There is a broad band ranging from 20° to 30° attributed to the amorphous carbon structure. Most of the remaining peaks can be assigned to zinc sulphide (ZnS), which is a result of the reaction of ZnO, present in the rubber due to the vulcanization process, with the H_2S formed during the rubber degradation in the pyrolysis process [175,176], and/or to a zinc silicate, willenite (Zn_2SiO_4), due to the reaction between ZnO and the SiO_2 also used in tyre manufacture [177].

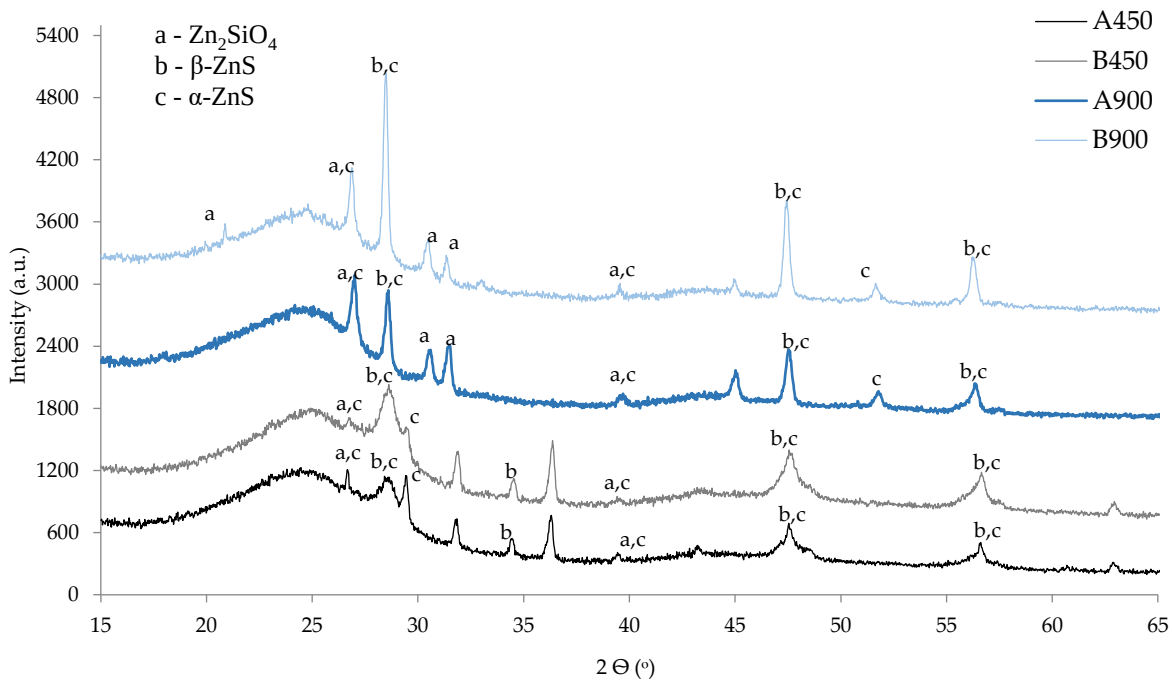

Figure 9 - XRPD spectra of the produced chars

3.3 Single component adsorption assays

The four obtained chars were studied in the adsorption process of Neodymium (Nd^{3+}) and Dysprosium (Dy^{3+}) from synthetic solutions, aiming to determine the possibility of using these materials as adsorbents in the recuperation of these REEs. The studies were performed at room temperature and at the natural pH of the synthetic solutions (6.40 for Nd^{3+} solution and 7.36 for Dy^{3+} solution). The speciation diagram of Nd shows that up pH 8 the dominant species are the free Nd^{3+} and above this pH value, it starts to precipitate as hydroxide. Dy follows the same behaviour [178]. Also, previous works demonstrated no advantage in the removal of the Nd and Dy by decreasing the solution pH [50,179], thus no changes on the medium pH were made.

Figure 10 shows the uptake capacities obtained on the preliminary assays to evaluate the performance of the chars and commercial carbon.

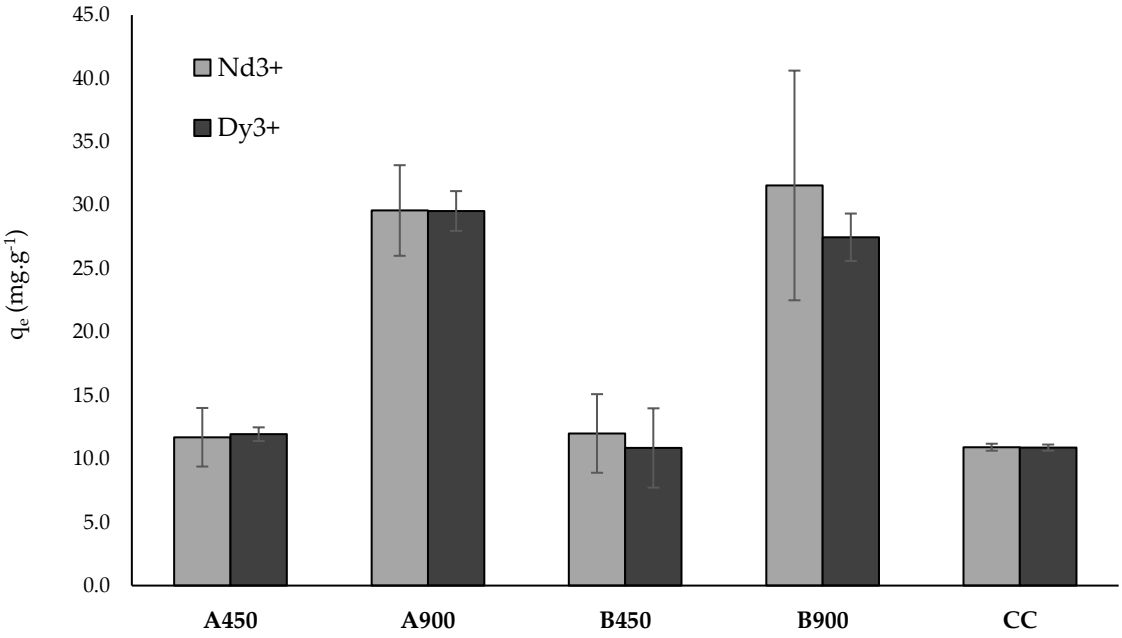

Figure 10 - Nd^{3+} and Dy^{3+} uptake capacities for the produced chars and commercial carbon. Conditions: A450, B450 and CAC mass = 50 mg; A900 and B900 mass = 20 mg; Initial concentration = 100 mg L-1; solution volume = 10 mL; contact time = 72 h.

The chars obtained at 900 ºC are the most efficient adsorbents for both elements with uptake capacities around 30 $mg.g^{-1}$. The chars obtained at 450 ºC presented uptake capacities similar to the commercial carbon (≈ 11 mg g^{-1}). The differences observed between chars A and B are within the error associated to the experiments. Textural properties are not the determinant feature, because the chars obtained at different temperatures presented similar surface areas and CAC sample has a very high surface area. Surface chemistry should be playing the most important role. Looking to the pH_{PZC} of the carbon samples (Table 6), it is possible to observe that the values are above the pH of the REEs solutions, thus it is expected a positively charged surface that repels Nd^{3+} and Dy^{3+} ions, ruling out electrostatic attraction mechanism. The chars obtained at 900 ºC might present a higher availability and accessibility of cations that favour the ion exchange mechanism. This will be further discussed in the next sections.

3.3.1 Kinetic study – influence of contact time

The results of kinetic assays are plotted in Figure 11 for both Nd^{3+} and Dy^{3+} using the different adsorbents.

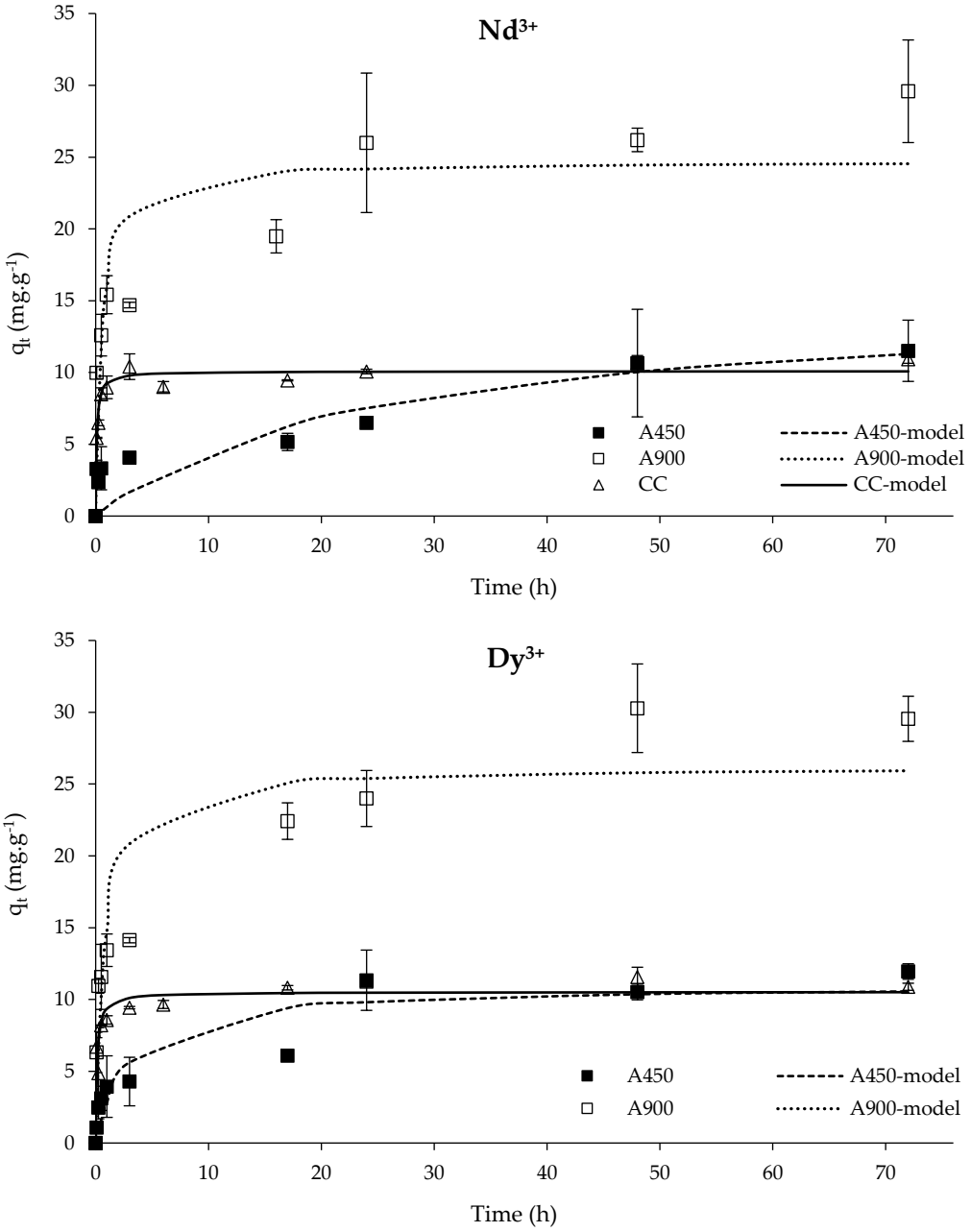

Figure 11 - Adsorption kinetic data of Nd^{3+} and Dy^{3+} for all carbon samples adjusted to PSO kinetic model. Conditions: A450, B450 and CAC mass = 50 mg; A900 and B900 mass = 20 mg; Initial concentration = 100 $mg.L^{-1}$; solution volume = 10 mL.

The PFO and PSO non-linear kinetic models were fitted to the experimental data. The best-fitting model was defined by the higher coefficient of determination (R^2). The nonlinear

fitting plots using the PSO kinetic model are represented in Figure 11. Overall, the fittings obtained with this model presented slightly higher R^2 (Table 8). However, it can be said that both kinetic models were well-fitted to the experimental data (Table 8). It has been widely accepted that these kinetic models are empirical and lack physical meanings, being k_1 and k_2 lumped constants that combine reaction and diffusion effects [180].

Table 8 - Nd^{3+} and Dy^{3+} adsorption kinetic parameters obtained from the PFO and PSO kinetic modelling

		Nd^{3+}					**Dy^{3+}**				
		A450	B450	A900	B900	CAC	A450	B450	A900	B900	CAC
PFO model	**q_e** ($mg.g^{-1}$)	12.3	11.8	23.4	20.4	9.8	10.0	10.6	24.9	22.9	10.3
	k_1 (h^{-1})	0.037	0.070	1.30	0.352	6.03	0.287	0.125	0.888	0.392	4.05
	R^2	0.896	0.965	0.747	0.894	0.920	0.840	0.983	0.806	0.931	0.813
PSO model	**q_e** ($mg.g^{-1}$)	15.1	14.0	24.7	22.0	10.1	11.0	12.1	26.2	24.4	10.5
	k2 ($g.mg^{-1}.h^{-1}$)	0.003	0.006	0.073	0.020	1.07	0.032	0.013	0.049	0.022	0.758
	R^2	0.884	0.965	0.821	0.927	0.961	0.878	0.989	0.872	0.958	0.877

Nevertheless, some authors have made the effort to establish the rate controlling mechanism by using PFO and PSO kinetic models. Hubbe *et al.* [181] assumed that a good fitting to the PSO kinetic model indicates a diffusion-limited mechanism affected by the heterogeneous distribution of pore sizes and the continuous partitioning of solute species between a dissolved state and a fixed state of adsorption. PFO kinetic model has been related to surface reaction as the rate-limiting step [181]. It can be argued that both mechanisms, surface reaction and diffusional constraints, are controlling the sorptive process rate [182]. Other authors suggested that the reaction rate may be dependent on the number of active sites existing on the adsorbent: PFO model represents the condition that a few active sites exist in the adsorbent material, or a few adsorbate ions can interact with the active sites, and the PSO model could represent the conditions in which the adsorbent has abundant active sites [88].

The obtained kinetic parameters from PSO kinetic model confirmed that the higher uptake capacities at equilibrium were obtained with the chars prepared at the highest temperature, A900 and B900. CAC carbon presented the faster uptake, with the highest kinetic constant values, but the uptake capacities were the lowest ones. The chars showed slow

kinetics, with the equilibrium being achieved only at long times (48 - 72 h). The hydrophobic character of these chars originated by the spherical carbon black aggregates in their composition might be the reason behind it [183], as well as their heterogenous matrix. A900 and B900 presented higher kinetic constants than A450 and B450 samples since the higher temperature promoted the cleaning of the chars' surface due to the release of carbonaceous material attached to the carbon black particles, and this decreased their hydrophobicity.

3.3.2 Adsorption isotherms – influence of initial concentration

The adsorption isotherms were fitted to the Langmuir and Freundlich isotherm models. The modelling parameters are summarized in Table 9 and the plots depicting both the experimental points and Langmuir model are presented in Figure 12.

Table 9 - Langmuir and Freundlich parameters obtained from fitting to the experimental data

		Langmuir isotherm model						**Freundlich isotherm model**				
		A450	B450	A900	B900	CAC		A450	B450	A900	B900	CAC
Nd^{3+}	**q_{max}** ($mg.g^{-1}$)	10.0	12.5	32.8	28.2	12.8	**K_F**[a]	7.65	7.14	23.8	16.0	6.67
	K_L ($L.mg^{-1}$)	0.937	0.948	0.763	0.254	0.155	**n**[b]	18.1	6.72	14.5	8.6	7.68
	R^2	0.932	0.856	0.975	0.979	0.998	**R^2**	0.888	0.889	0.973	0.989	0.999
Dy^{3+}	**q_{max}** ($mg.g^{-1}$)	11.7	13.1	34.3	32.8	10.8	**K_F**[a]	7.05	9.22	23.7	19.4	6.71
	K_L ($L.mg^{-1}$)	0.147	0.232	0.656	0.317	0.259	**n**[b]	10.7	15.3	12.4	8.95	10.3
	R^2	0.992	0.957	0.960	0.979	0.992	**R^2**	0.989	0.953	0.952	0.982	0.995

[a] $(mg.g^{-1})(mg.L^{-1})^n$; [b] dimensionless

The Freundlich isotherm model presents a slightly better fitting, indicating that multilayers are being formed. However, it is ambiguous which model better describes the experimental behaviour, and maybe it is a combination of the two models. Additionally, the char's heterogeneity, revealed by the high error bars in the experimental points, might have accounted for the mixed behaviour.

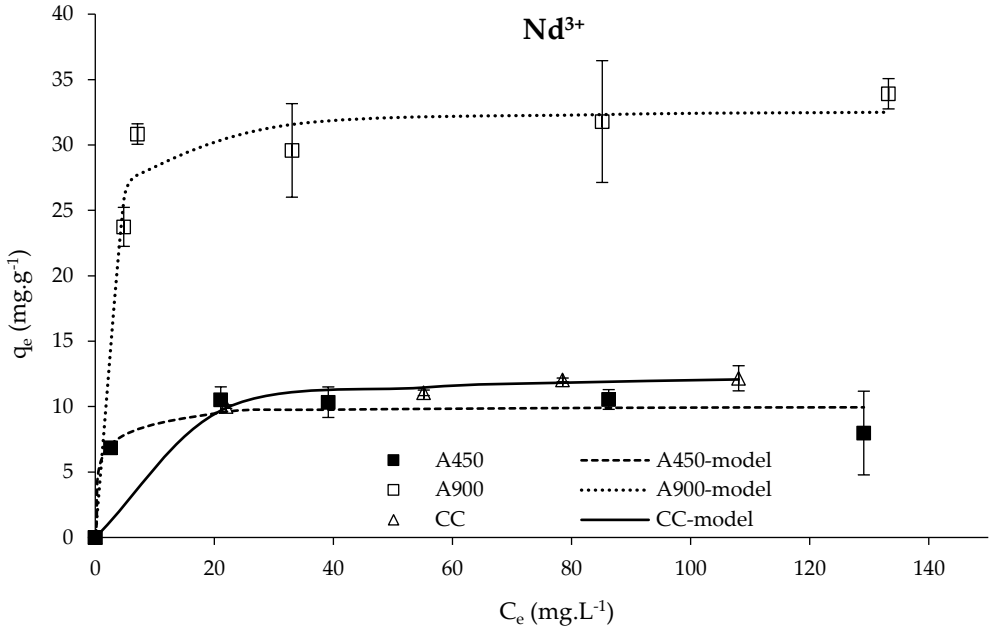
Nd3+
qe (mg.g-1)
Ce (mg.L-1)
A450
A900
CC
A450-model
A900-model
CC-model

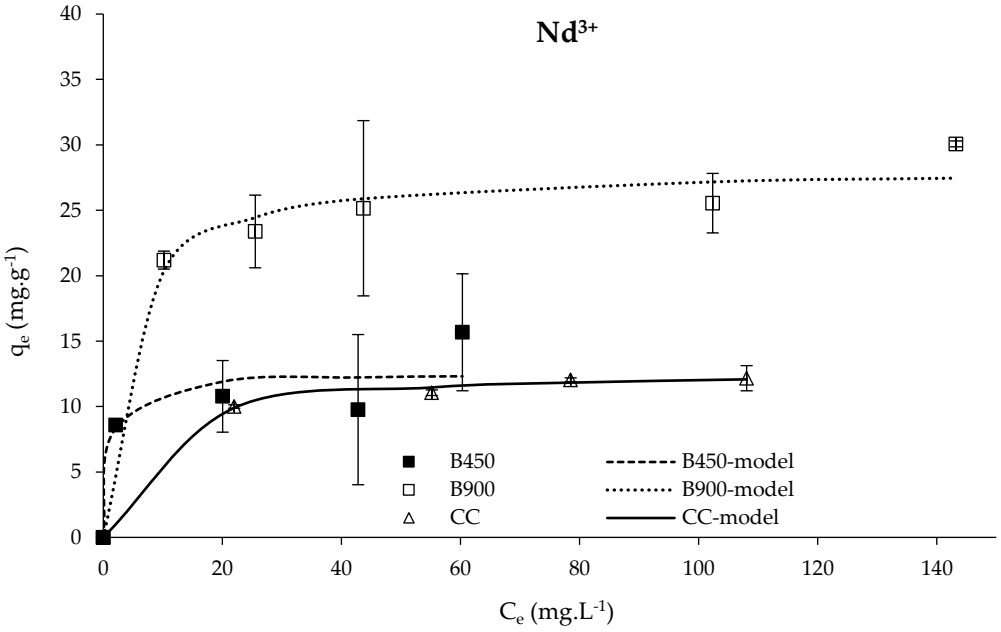
Nd3+
qe (mg.g-1)
Ce (mg.L-1)
B450
B900
CC
B450-model
B900-model
CC-model

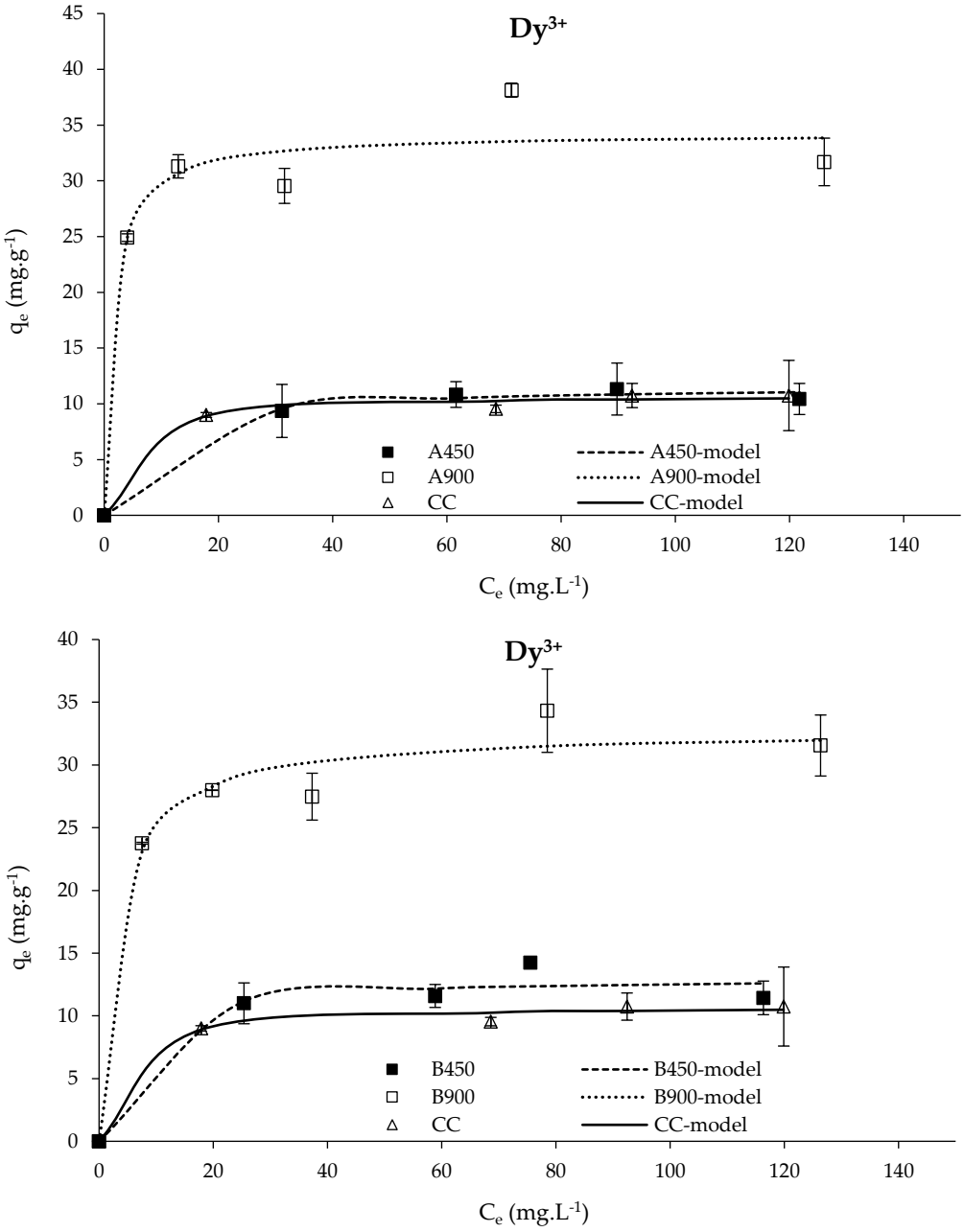

Figure 12 - Adsorption isotherm data of Nd^{3+} and Dy^{3+} for all carbon samples adjusted to Langmuir model. Conditions: A450, B450 and CAC mass = 50 mg; A900 and B900 mass = 20 mg; Equilibrium time = 72 h; solution volume = 10 mL.

These results confirmed the better performance of A900 and B900 chars for Nd^{3+} and Dy^{3+} removal. The uptake capacities obtained with these chars were in the range of 28.2 to 34.3 $mg.g^{-1}$, values that are comparable, or even higher, with others reported in the literature obtained in the adsorption of these REEs by using spent coffee-activated carbons [184], carbon black from recycled tires [185], or pine wood sawdust biochar [186].

There is no significant differences in the uptake of the two ions since they have similar chemical properties.

3.3.3 Nd and Dy removal mechanism

As already mentioned in section 3.3, the textural properties of the carbons were not determinant and electrostatic attraction was excluded. To assess if ion exchange mechanism had a role in the removal of Nd^{3+} and Dy^{3+}, the release of Ca, Fe, Mg, and Zn ions from A450 and A900 chars was determined after single adsorption assays. These tests were performed with 50 mg of A450 char and 20 mg of A900 chars, mixed for 72 h with 10 mL of Nd and Dy solutions with a concentration of 100 $mg.L^{-1}$. A blank test with the chars and ultra-pure water was performed. Cation concentrations were determined by ICP-AES.

Figure 13 shows the amount of REEs adsorbed and released cations, in mmol, per char mass (g). According to the results obtained, Nd and Dy removal mainly occurs through the exchange with Zn ions and there is also a smaller contribution of Ca ions. Thus, it can be assumed that chars obtained at 900 ºC have a higher availability of Zn and Ca ions to exchange.

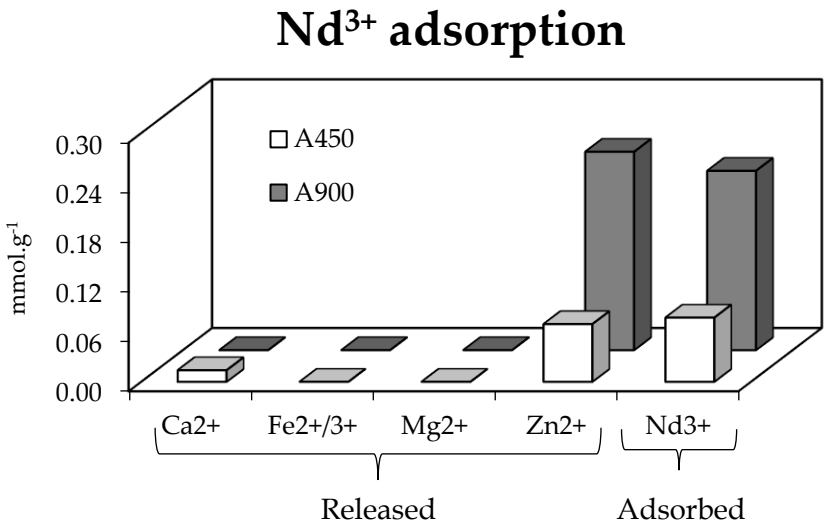

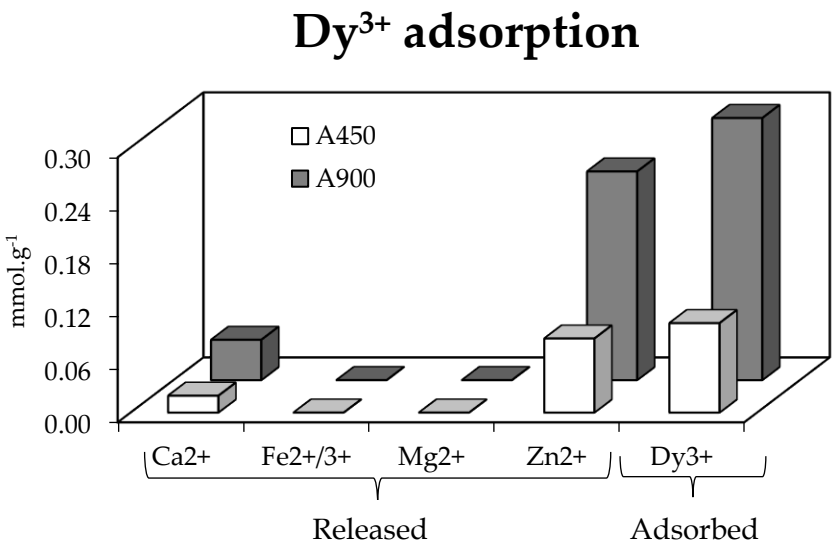

Figure 13 - Nd^{3+} (above) and Dy^{3+} (below) adsorbed and released cations from the A450 and A900 chars. Conditions: A450 mass = 50 mg; A900 mass = 20 mg; contact time = 72 h; solution volume = 10 mL

XPS analysis of char A900 before and after adsorption of Nd and Dy ions was performed. Figure 14 displays the detailed regions for C 1s, O 1s, S 2p, Si 2p, Dy 4d, Nd 4d and Zn $2p_{3/2}$ and Table 10 presents the overall quantification of the studied elements.

Table 10 - XPS atomic concentrations (%) of relevant elements in A900 char before and after Nd (A900Nd) and Dy adsorption (A900Dy)

	A900	A900Dy	A900Nd
C	78.1	83.3	83.3
O	16.5	13.4	11.8
S	0.5	0.4	1.1
Si	4.1	2.6	3.3
Zn	0.8	n.q	n.d
Dy	n.d.	0.3	n.d
Nd	n.d.	n.d	0.6

n.q. – not quantifiable; n.d. – not detected

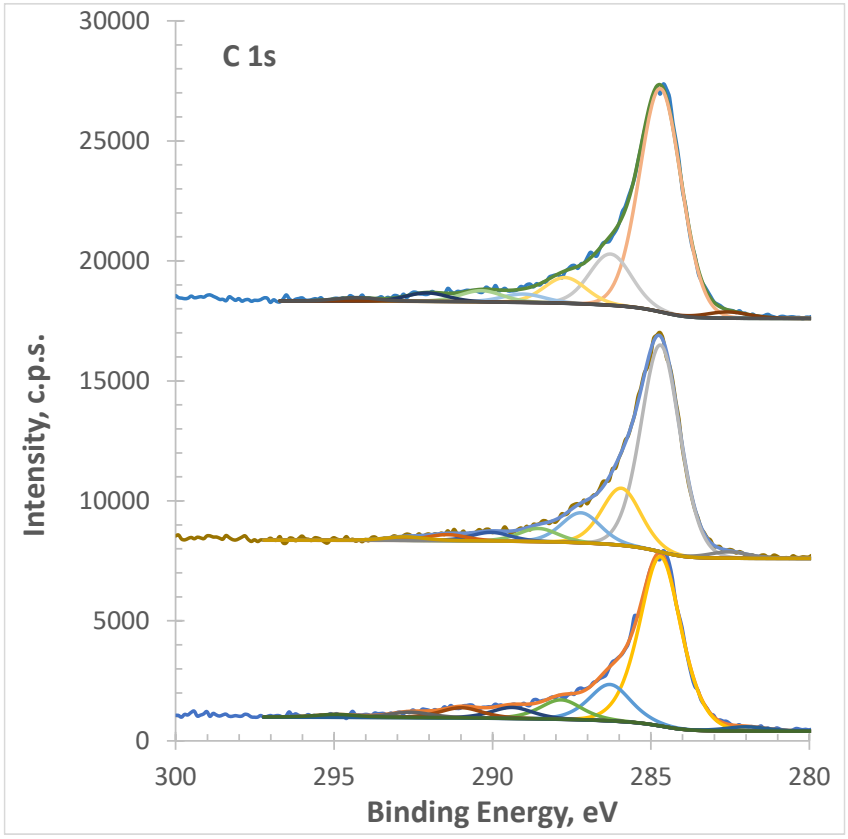
C 1s
30000
25000
20000
15000
10000
5000
0
Intensity, c.p.s.
300
295
290
285
280
Binding Energy, eV

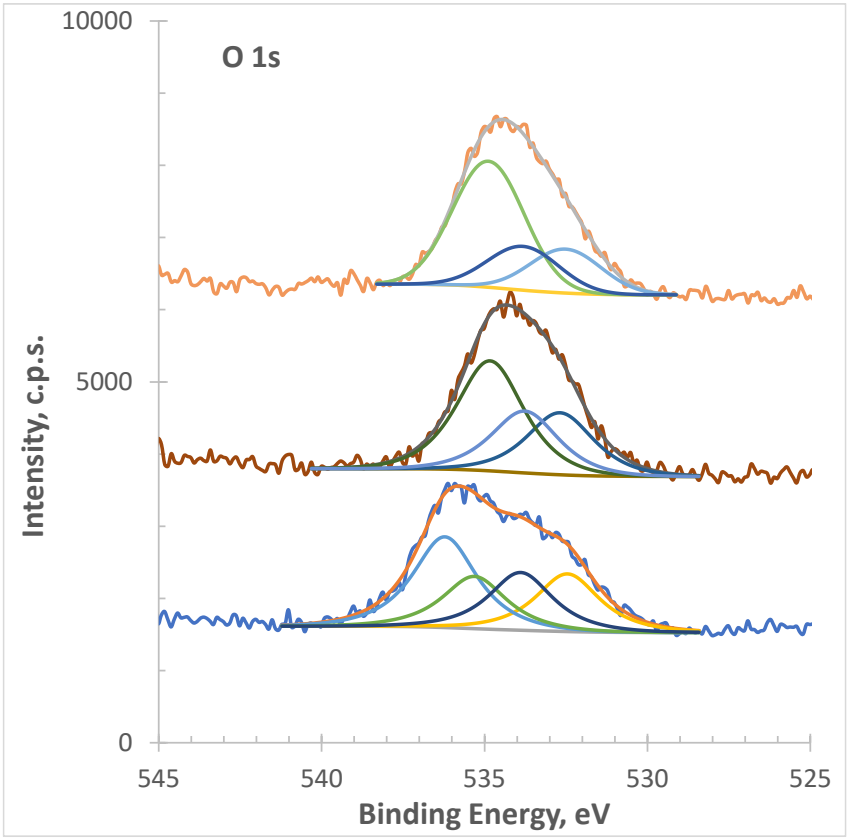
O 1s
10000
5000
0
Intensity, c.p.s.
545
540
535
530
525
Binding Energy, eV

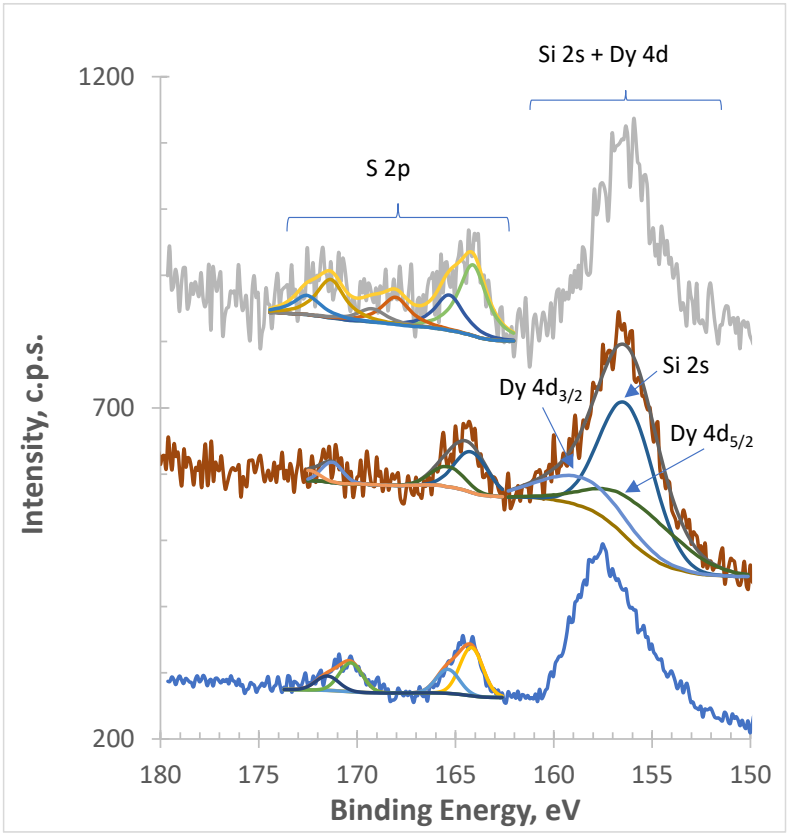
Si 2s + Dy 4d
S 2p
Si 2s
Dy 4d3/2
Dy 4d5/2
Intensity, c.p.s.
1200
700
200
180
175
170
165
160
155
150
Binding Energy, eV

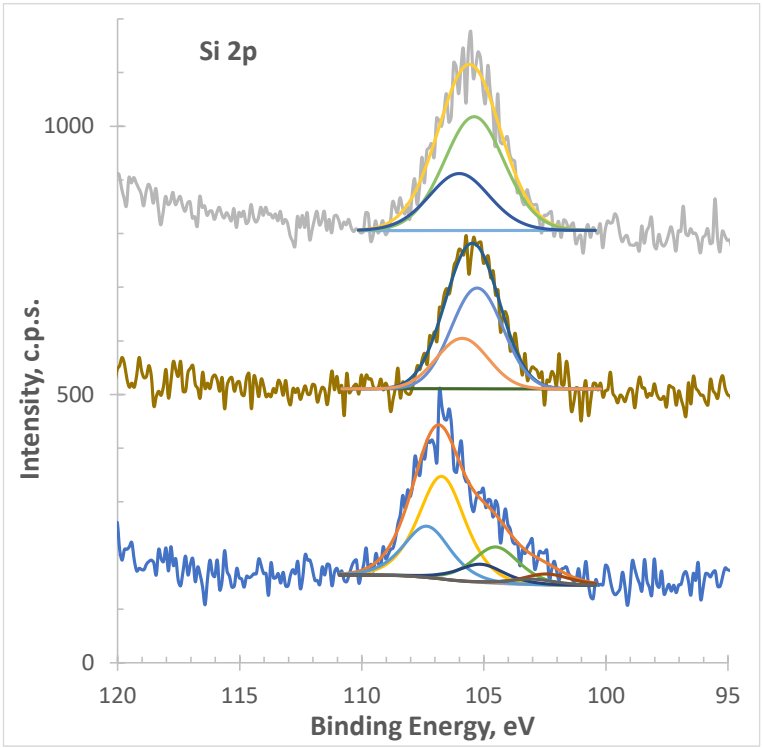
Si 2p
Intensity, c.p.s.
1000
500
0
120
115
110
105
100
95
Binding Energy, eV

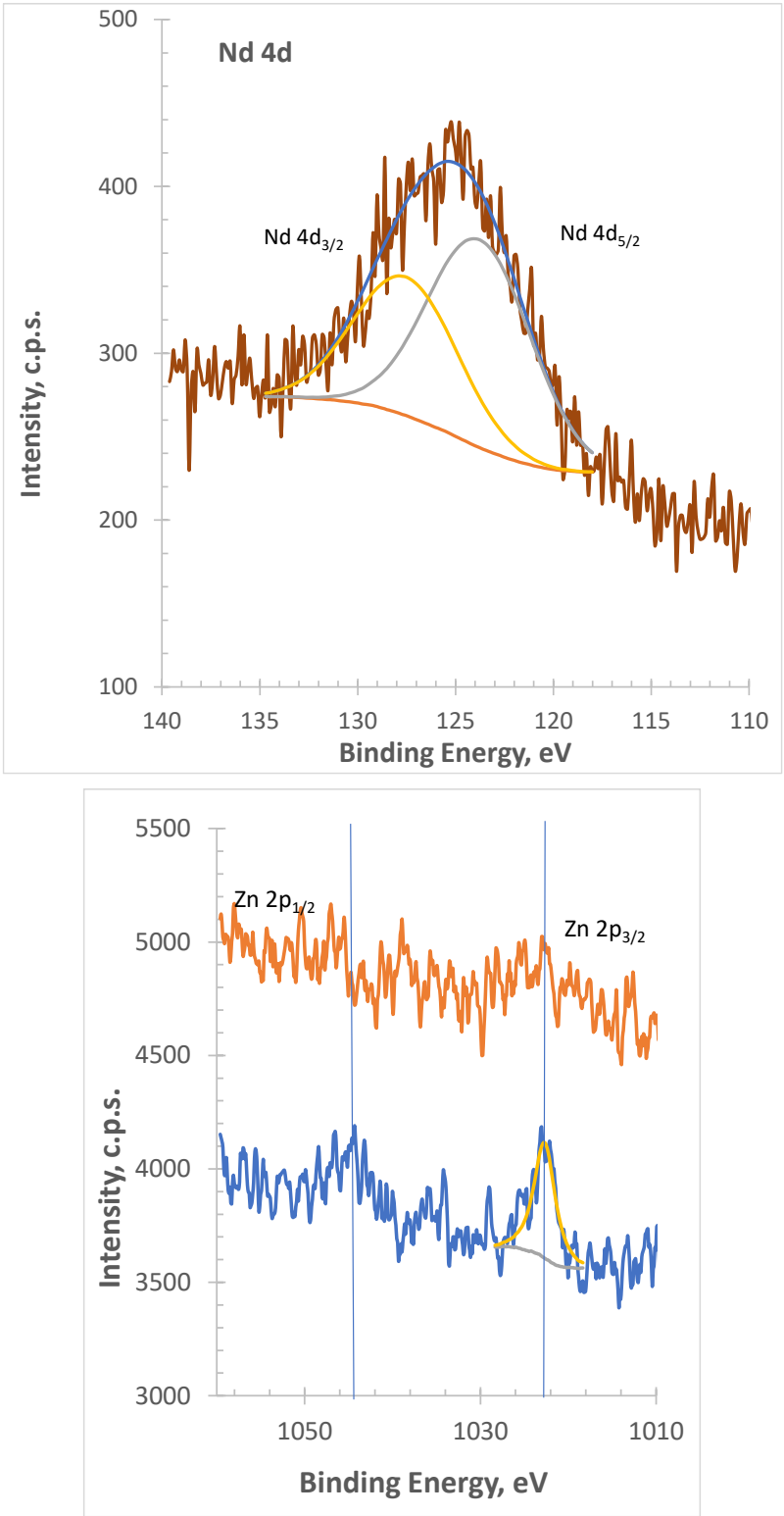

Figure 14 - XPS detailed regions C 1s, O 1s, S 2p, Si 2p, Dy 4d, Nd 4d and Zn 2p3/2. In each spectrum corresponds, from bottom to top, to samples A900, A900Dy, and A900Nd. Zn is not detected in A900Nd

Table 11 contains the details about the peaks fitted to the regions in Figure 14, namely, the peak position, in eV, and the atomic percentage computed from the peak areas and respective sensitivity factors.

Table 11 - XPS atomic concentrations (%) of relevant elements in A900 char before and after Nd (A900Nd) and Dy adsorption (A900Dy)

	A900		**A900Dy**		**A900Nd**		**Assignment**
	BE(eV)	Atomic%	BE(eV)	Atomic%	BE(eV)	Atomic%	
C 1s 1	284.7	55.9	284.7	56.1	284.7	60.3	C sp^3 + C sp^2 (see text)
C 1s 2	286.3	12.1	285.9	15.5	286.3	13.8	
C 1s 3	287.8	6.4	287.2	8.1	287.7	6.9	
C 1s 4	289.4	3.7	288.6	3.5	289.0	2.2	O-C=O
C 1s 5	291.0		290.0		290.4		
C 1s 6	292.6		291.4		292.1		π→π*
C 1s 7	294.9		292.8		294.3		
O 1s 1	532.5	3.7	532.7	3.5	532.5	3.5	C=O
O 1s 2	533.9	3.7	533.8	3.5	533.1	0.4	C-O
O 1s 3	535.3	3.3	534.8	6.3	534.8	7.8	Si-O
O 1s 4	536.2	5.8					Si-O
S $2p_{3/2}$ 1	164.2	0.20	164.2	0.22	164.1	0.37	C-S
S $2p_{1/2}$ 1	165.4	0.10	165.4	0.11	165.3	0.19	
S $2p_{3/2}$ 2					168.0	0.14	SO_4^{2-}
S $2p_{1/2}$ 2					169.2	0.07	
S $2p_{3/2}$ 3	170.3	0.12	171.3	0.07	171.3	0.20	Oxidized S on silicates
S $2p_{1/2}$ 3	171.5	0.06	172.5	0.04	172.5	0.10	
Si $2p_{3/2}$ 1	102.4	0.20					Silicone (see text)
Si $2p_{1/2}$ 1	103.0	0.10					
Si $2p_{3/2}$ 2	104.5	0.67	105.3	1.7	105.4	2.2	
Si $2p_{1/2}$ 2	105.1	0.33	105.9	0.87	106.0	1.1	
Si $2p_{3/2}$ 3	106.7	1.9					
Si $2p_{1/2}$ 3	107.3	0.94					
Dy $4d_{5/2}$			155.5	0.16			Dy^{3+}
Dy $4d_{3/2}$			158.5	0.11			
Nd $4d_{5/2}$					123.8	0.36	Nd^{3+}
Nd $4d_{3/2}$					127.6	0.24	
Zn $2p_{3/2}$	1022.3	0.81					Zn^{2+}

In all the samples, carbon, oxygen, sulfur and silicon were detected. In A900Dy and A900Nd, beyond those elements, dysprosium in the first sample, and neodymium in the second, were also found and in sample A900 Zn was clearly detected.

C 1s region was very similar in the three samples. It was fitted with 8 peaks. The three peaks at highest binding energy (BE) values ranging from 290.0 eV to 295.0 eV are assigned to energy losses due to $\pi \rightarrow \pi^*$ excitations. Around 289.0±0.4 eV there is a peak assignable to the carboxylic/carboxylate group. Quantitative analysis is compatible with the fact that this is the only carbon-based group bonded to oxygen. This leaves the rest of the components being just fitting peaks to yield an asymmetric profile associated to graphitic carbon [187] combined with a component corresponding to aliphatic carbon.

Oxygen was fitted with 3 peaks, excepting the sample A900 where 4 peaks were needed. The peaks at lower BE were constrained to have the same area and, in the three samples, they are centred at 532.6±0.1 eV (assigned to C=O) and at 533.8±0.1 eV (assigned to C-O). Sample A900Nd is an exception, with the "C-O" peak being at 533.1 eV, much closer to the first component, suggesting that a part of the carboxylic group is, in fact, a carboxylate one (where a single peak should occur). The third (and the fourth) components at higher energies are quantitatively compatible with O bonded to silicon. Its high BE value is in line with the equally high value found for silicon (in Si 2p) and a tiny part of sulfur peaks (in S 2p) and is likely due to the positive charge accumulation, during the ejection of photoelectrons, on the non-conductive phase typical of silicate structures. The fact that the Si-O group was significantly affected after the adsorption of Nd and Dy indicates that the REEs were exchanged with the Zn associated to silicate structures that were visible in the XRPD patterns (Figure 9). Although Si was not detected in the char by ICP-AES (Table 7), probably because it was not solubilized in the acidic digestion, XPS confirmed the presence of this element at char's surface. A900 was further analysed by SEM-EDS (Figure 15) and EDS spectrum also showed the presence of Si at char's surface.

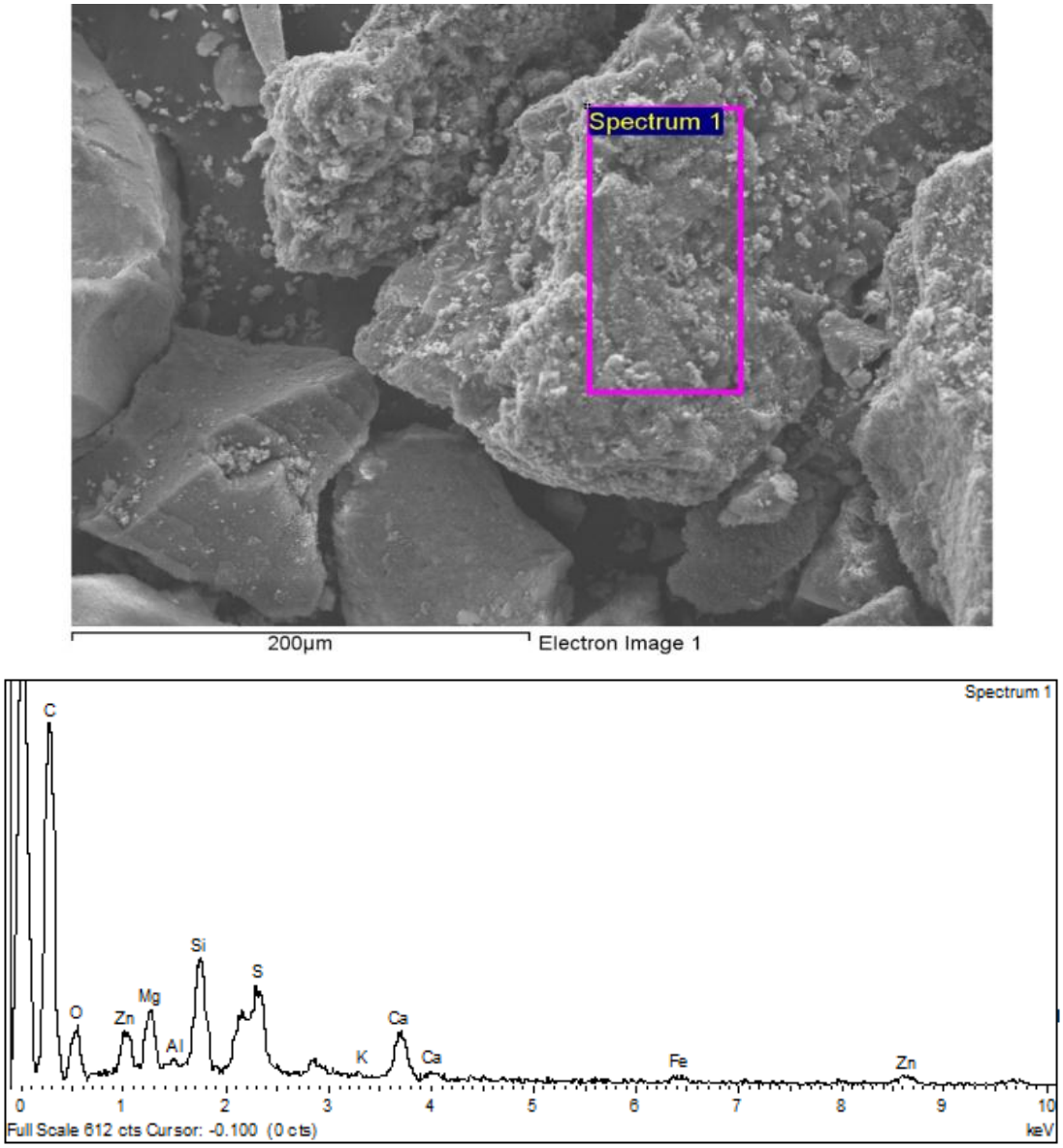

Figure 15 - SEM image of A900 char particles with 300x magnification and the corresponding EDS spectrum of the selected zone

Si 2p and S 2p regions were both fitted with doublets with a spin-orbit split of 0.61 eV and 1.2 eV, respectively. Si 2p shows a single doublet in samples A900Dy and A900Nd, with the main component, Si $2p_{3/2}$ centred at 105.4±0.1 eV. In sample A900 also a vestigial amount of silicon with Si $2p_{3/2}$ centred at 102.4 ±0.1 eV is detected. It is assigned to the silicone existing in the double-sided tape used to hold the powdered sample. It was not observed in the rest of the samples.

The S 2p region presents in all the samples a doublet with the main component S $2p_{3/2}$ centred at 164.2 ±0.1 eV attributed to elemental sulfur or bonded to carbon. In the sample A900Nd a very low intensity doublet with the main component at 168.0 eV may correspond

to a sulphate group. Finally, in all the samples, a doublet having the main component at very high BE (170.3 eV for sample A900 and 171.3 eV for samples A900Dy and A900Nd) denotes the existence of some oxidized sulfur on the surface of silicate structures.

In sample A900, the region Zn 2p, the most intense for this element, displays a peak, Zn $2p_{3/2}$, centred at 1022.3 eV assigned to Zn^{2+} and a lower intensity one corresponding to Zn $2p_{1/2}$ with a spin-orbit split of ~23 eV. In sample A900Dy, it seems to exist a similar doublet but without enough intensity to allow for fitting; therefore, it is not possible to have precise values for the position of the peak and respective area. In sample A900Nd no Zn was detected. The fact that no Zn was detected at char's surface after the adsorption of the REEs confirms the ion exchange mechanism.

Dysprosium has low intensity peaks in the regions Dy 4s and Dy 4p. The region Dy 4d superposes to the peak Si 2s. To extract the information about Dy 4d, it was assumed that the relation between the Si 2p and Si 2s in the samples A900Dy and A900Nd (the Si 2p region is very similar in both) was the same (equal difference BE(Si 2s)-BE(Si 2p) and equal ratio FWHM(Si2s)/FWHM(Si 2p)). The remaining area was fitted with a doublet having an intensity ratio I(Dy $4d_{5/2}$)/ I(Dy $4d_{3/2}$)=1.5 and yielded the main component Dy $4d_{5/2}$ at 155.5 eV, assigned to Dy^{3+} as Dy_2O_3 [188], and a spin-orbit split of 3 eV that was not compared to literature due to lack of available data.

Finally, for neodymium, the regions Nd 3d, Nd 4s, Nd 4p and Nd 4d were acquired. The region Nd 3d superposes the C KKL Auger region when the Mg Kα radiation is used and that is the reason for choosing to present here just the results obtained with the Al Kα radiation. However, even in the absence of spectral superpositions, the region Nd 3d is complicated by several shake-up and shake-down satellites resulting from core-hole screening effects in the final state [189]. This fact renders the quantification a very difficult task. Instead, the fitting of the Nd 4d region is presented in Figure 14 and yielded a doublet with the main component Nd $4d_{5/2}$ centred at 123.8 eV and 3.8 eV of spin-orbit split and assignable to Nd^{3+} as Nd_2O_3 [188,190].

XPS results show that both Nd and Dy were adsorbed as oxides after Zn was released from silicate structures.

3.4 Bicomponent batch adsorption studies

The char with the best performance on the single component adsorption studies, A900, was further selected to be tested with Nd/Dy binary mixtures to assess synergistic, antagonistic and/or non-interaction effects between the two adsorbates. The Nd/Dy concentrations ratio studied were: 100:100, 50:50, 100:50, 100:25, 25:100 and 50:100.

Analysing the results (Figure 16), it is possible to conclude that in the mixtures with equal amounts of the REEs, there is a trend to adsorb a little bit more of Dy^{3+}. A possible explanation is based on the ionic radius which is slightly smaller for Dy^{3+} compared to that of Nd^{3+} [191], which may have favoured its contact with the active sites at chars' surface. It is also interesting to note that the uptake capacity in bicomponent solutions for both Nd and Dy (Nd+Dy) is generally higher than for single component solutions, since there is a higher driving force triggered by the higher concentration gradient.

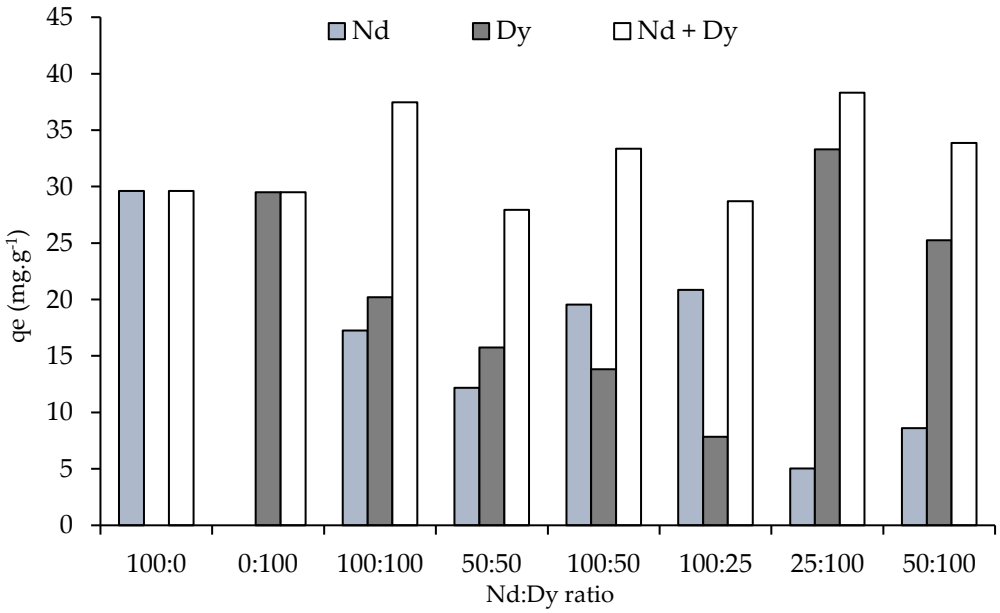

Figure 16 - Nd^{3+} and Dy^{3+} uptake with A900 char from mono and bicomponent solutions at different concentration ratios. Conditions: A900 mass = 20 mg; contact time = 72 h; solution volume = 10 mL

3.5 Conclusions

Two samples of spent tire rubber (STR) from different sources (rubber A and rubber B) were submitted to semi-continuous pyrolysis thermochemical conversion. The obtained chars were denominated A450 and A900 from rubber A obtained at 450ºC and 900ºC, respectively, and

B450 and B900 according to the same reasoning. The char materials were then applied as recovery agents of Nd^{3+} and Dy^{3+} from aqueous solutions in mono and bicomponent solutions, and their performance was benchmarked with a commercial activated carbon.

The chars obtained at 900 ^{o}C were the most efficient adsorbents for both elements with uptake capacities around 30 mg.g^{-1} by using 20 mg of char. The chars obtained at 450 ^{o}C presented uptake capacities similar to the commercial carbon (≈ 11 mg g^{-1}) when using 50 mg of char. A900 and B900 chars presented a higher availability of Zn ions that favoured the ion exchange mechanism. Particularly, it was found that both Nd^{3+} and Dy^{3+} were adsorbed as oxides after Zn was released from silicate structures such as willenite (Zn_2SiO_4). The chars showed slow kinetics, with the equilibrium being achieved only at long times (48 - 72 h).

The char with the best performance on the single component adsorption studies, A900, was further selected to be tested with Nd/Dy binary mixtures and it was found a trend to adsorb a slightly higher amount of Dy^{3+}. The uptake capacity in bicomponent solutions for both Nd and Dy was generally higher than for single component solutions due to the higher driving force triggered by the higher concentration gradient.

Although synthetic solutions of Nd and Dy were used in the present work trying to simulate wastewaters from e-waste recycling industries, an industrial effluent will allow to assess the feasibility of the STR char as recovery agents of these REEs when applied to real samples where the solution chemistry is significantly different. This will be discussed in the following Chapter.

4

BATCH PYROLYSIS CHARS AND ACTIVATED CARBONS: BATCH AND DYNAMIC ADSORPTION ASSAYS ON REAL MAGNET LEACHATES

This chapter builds upon the findings from Chapter 3 by extending the study to include both batch and dynamic adsorption assays using chars and activated carbons derived from batch pyrolysis of spent tire rubber. The focus here is on the adsorption of REEs from real magnet leachates, simulating more realistic conditions than synthetic solutions. This chapter also analyses the performance of the produced chars and ACs, providing a comprehensive assessment of their adsorption capacities and kinetic behaviour in both static and dynamic systems. Additionally, a brief discussion on the dissolution and leaching of REEs from NdFeB magnets is included. The results presented in this chapter contribute to a deeper understanding of the practical applicability of these materials in industrial-scale REE recovery processes.

Part of this section was published, partially or completely, in the following scientific publications:

- M. Nogueira, I. Matos, M. Bernardo, F. Pinto, I. Fonseca., and N. Lapa; Recovery of Nd^{3+} and Dy^{3+} from E-Waste using Adsorbents from Spent Tyre Rubbers: Batch and Column Dynamic Assays; *Molecules;* 2024; doi: 10.3390/molecules30010092
- Bernardo M., Lapa N., Pinto F., Nogueira M., Matos I., Ventura M., Ferraria A.M., do Rego A.M.B., Fonseca I.M. (2023) Valorisation of spent tire rubber as carbon adsorbents for Pb(II) and W(VI) in the framework of a Circular Economy. *Environmental Science and Pollution Research*, 30 (30), 74820 – 74837. DOI: https://doi.org/10.1007/s11356-023-27689-5

4.1 Pyrolysis Assays and Chars' Activation

The pyrolysis parameters used in this work were based on previous studies to maximize the char [131–133].

Table 12 shows that the char yield was 39.8% for A405 and 37.5% for B405. The gas yields were 9.07% and 10.5% and oil yields were 51.2% and 52.0% for char A405 and B405, respectively. It was also possible to conclude that the source of STR does not affect the pyrolysis process as both chars (A405 and B405) presented comparable results even though they come from different sources of tyres.

Table 12 - Batch pyrolysis assays yields and activation burn-off rates

		η (% w/w)		
		Char	**Oil**	**Gas**
Pyrolysis	**A405**	39.8	51.2	9.07
	B405	37.5	52.0	10.5
		Burn-off (% w/w)		
Activation	**A405-CO2**	14.3		
	B405-CO2	16.9		

These results align with expectations from previous studies and literature reviews regarding yields at the chosen temperatures [48,51,54,55].

The activation of chars had a burn-off of 14.3% and 16.9% for A405-CO2 and B405-CO2, respectively. These results are similar to those found in the literature for activation with the same profile and activation agent [4,130,192], although they tend to be on the lower limit of the reported range results [130]. According to Hofman and Pietrzak [193], this could be attributed to the presence of ash in the chars as it can interfere with the activation process and the reactions taking place during this process.

4.2 STR rubber, chars, and activated chars

The thermal degradation profiles of rubbers A and B (Figure 17) are identical in both samples and show a steep mass loss of 61% wt. between 250 °C and 450 °C. Beyond this temperature range, there are no significant additional losses, resulting in a carbonaceous residue comprising 36% wt. at 900 °C. It was also observed that the source of STR does not affect the thermal decomposition process. The thermograms of the produced materials (Figure 17)

revealed that both chars and activated chars have high thermal stability showing a mass loss inferior to 10% wt. at 900 °C. Although all the materials show similar weight losses, the chars A405 and B405 show higher thermal degradations, as would be expected since they were obtained at lower temperatures than the activated chars.

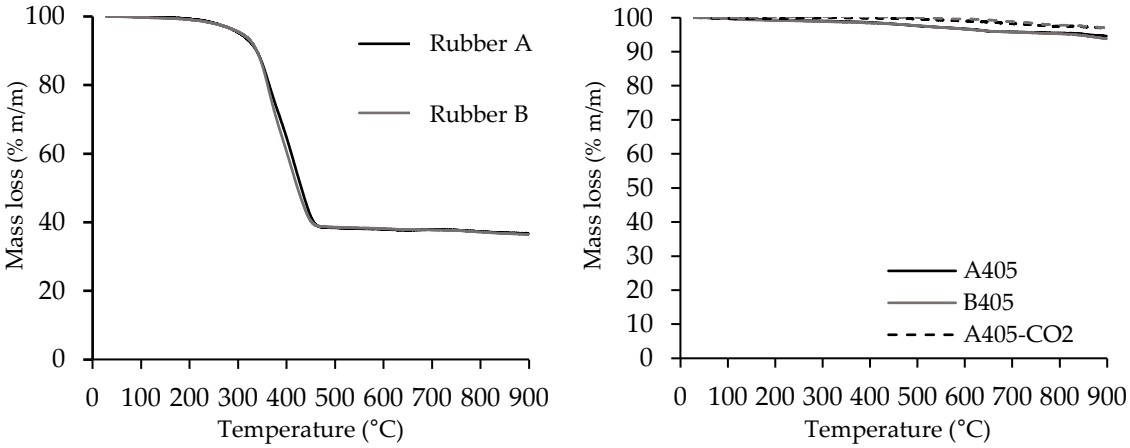

Figure 17 - Thermogravimetric analysis (left – STR precursors; right - chars and activated chars)

The elemental analysis (Table 13) displays an identical composition for both rubber precursors, with high carbon content, as well as a considerable amount of sulfur due to the vulcanisation procedure [194].

Table 13 - Elemental analysis, ash content, and pH_{PZC} of samples (as-received basis)

Sample	**C**	**H**	**N**	**S**	**Ash**	**pH_{PZC}**
	(% w/w)					
Rubber A	79.2	7.07	0.40	1.64	9.50	n.d.
Rubber B	83.4	7.60	0.40	2.04	8.70	n.d.
A405	71.3	0.71	0.28	2.51	36.2	7.4
B405	79.1	0.86	0.33	3.94	31.4	6.7
A405-CO2	70.3	0.16	0.23	2.90	38.8	8.5
B405-CO2	76.3	0.14	0.29	3.70	31.7	7.8
CAC	86.3	0.47	<0.20	0.57	5.70	9.1

n.d.: not determined

The produced chars retained a notably high concentration of carbon, while the levels of hydrogen and nitrogen decreased due to the thermal degradation of organic compounds during the carbonization process. This trend persists in the activated chars; however, there is a further reduction in the concentrations of hydrogen and nitrogen resulting from the activation process. On the contrary, there is an observed increase in sulfur and ash content in both chars and activated chars, attributable to the concentration effect experienced during the pyrolysis process and further accentuated during activation. This phenomenon arises from the release of volatile matter during these processes, while these compounds are retained in the solid matrix of the final products. The CAC sample exhibits a significantly lower ash content compared to the produced materials, as expected from a commercially activated carbon.

With Rubber A (9.50 % w/w) containing the highest concentration of ash among both precursors, it is evident that both materials derived from said rubber (A405 and A405-CO2) have higher ash concentrations when compared to their counterparts. All the carbon samples are characterised by having an alkaline behaviour (Table 13). Nevertheless, the activated chars have higher pH_{PZC} values than their char counterparts, attributed to the increased mineral content and the modification of their surface chemistry during the activation process.

Table 14 - Mineral composition of precursors, chars, and activated carbons ($mg.g^{-1}$; x±σ)

Element	Rubber A	Rubber B	A405	B405	A405-CO2	B405-CO2
Al	<0.002	<0.001	<0.002	<0.002	3.92 ± 0.05	2.93 ± 0.08
Ba	0.202 ± 0.022	$<4*10^{-5}$	$<4*10^{-5}$	$<4*10^{-5}$	0.029 ± 0.001	0.022 ± 0.001
Ca	13.0 ± 3.9	6.38 ± 0.18	21.9 ± 0.5	11.9 ± 0.8	16.56 ± 0.56	5.21 ± 0.19
Cr	0.002 ± 0.001	0.006 ±0.003	0.008 ± 0.001	0.010 ± 0.003	0.013 ± 0.001	0.011 ± 0.001
Cu	0.473 ± 0.049	1.02 ±0.17	0.318 ± 0.014	1.63 ± 0.03	0.23 ± 0.05	0.67 ± 0.03
Fe	2.18 ± 0.55	4.25 ± 0.27	4.96 ± 0.09	8.75 ± 0.15	4.59 ± 0.07	5.87 ± 0.21
K	<0.077	<0.078	<0.08	<0.08	3.15 ± 0.02	0.54 ± 0.01
Mg	0.815 ± 0.239	0.870 ± 0.105	1.79 ± 0.09	1.74 ± 0.01	1.66 ± 0.03	1.15 ± 0.05
Mn	0.029 ± 0.008	0.025 ± 0.002	0.052 ± 0.006	0.059 ± 0.002	0.054 ± 0.002	0.029 ± 0.001
Mo	$<4*10^{-4}$	$<4*10^{-4}$	0.036 ± 0.001	0.120 ± 0.006	0.021 ± 0.003	0.043 ± 0.003
Na	$<1*10^{-4}$	$<1*10^{-4}$	$<1*10^{-4}$	$<1*10^{-4}$	0.010 ± 0.001	$0.001 ± 2*10^{-5}$
Ni	0.004 ± 0.001	0.004 ± 0.001	0.012 ± 0.001	0.016 ± 0.001	0.012 ± 0.001	0.014 ± 0.002
Pb	0.081 ± 0.027	0.043 ± 0.001	0.118 ± 0.003	0.112 ± 0.003	0.041 ± 0.002	0.036 ± 0.001
Si	<0.002	<0.002	<0.002	<0.002	105.0 ± 13.2	39.16 ± 7.18
Zn	29.2 ± 0.2	38.6 ± 5.4	69.6 ± 1.8	93.5 ± 0.8	49.55 ± 0.10	67.54 ± 3.97

The STR samples A and B (Table 14) present a notably similar mineral composition, with both samples containing significant amounts of zinc (Zn), calcium (Ca), and iron (Fe). These elements are commonly found in various vulcanisation agents and are used as additives in the tyre manufacture industry [194,195]. After pyrolysis and activation, these same chemical elements were detected in both chars and activated chars, albeit in higher concentrations attributed to the effect of concentration during pyrolysis. Furthermore, it is notable that Rubber B exhibits a slightly higher concentration of Zn, a characteristic also reflected in the produced materials derived from this precursor. This observation indicates that while the source of STR may not influence the pyrolysis process, its origin does indeed impact the mineral composition of the resulting materials. This variation is likely to influence the adsorption mechanism, as will be further elucidated in this work. An interesting feature is that although silicon (Si) was not detected in the rubbers and raw chars, the corresponding

activated chars presented a high content of this element. A possible assumption is that Si was not solubilized in the acidic digestion, while the activation process of the chars produced a more soluble Si compound able to be quantified.

In the case of CAC, Si, Al, and Fe were its major elements, albeit in lower concentrations when compared to the produced materials, as is evident by its ash concentration [137]. The elements Cd, Se, Sn, and Ti were not detected in the samples.

Textural characteristics of the adsorbents were acquired from N_2 adsorption-desorption isotherms (Table 15 and Figure 18). Both chars exhibit identical surface areas (A_{BET}), which are consistent with the values reported in the literature [16,38,192]. The activated chars A405-CO2 and B405-CO2 demonstrated a slight increase in their A_{BET} and total pore volume in comparison with their char counterparts, attributed to the surface development from the activation with CO_2. The CAC sample is characterised by a high surface area (1030 $m^2.g^{-1}$) with narrow mesopores and large micropores [137].

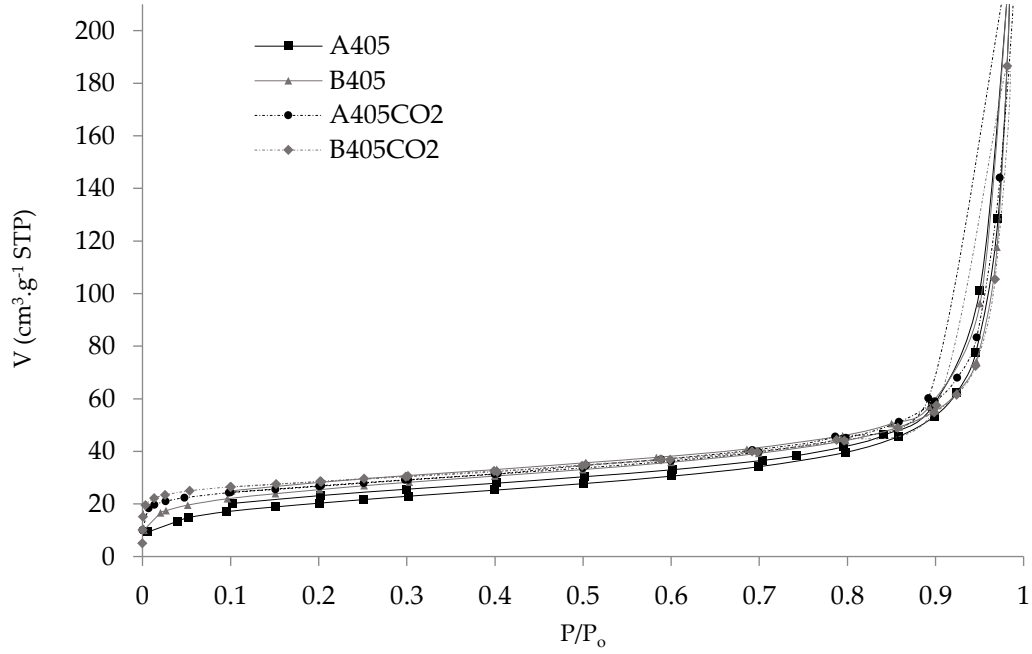

Figure 18 - N_2 adsorption-desorption isotherms for the produced adsorbents

Both the produced chars and activated chars display type IV(a) isotherms [196], typically associated with mesoporous materials. Conversely, the CAC sample demonstrates a mixture of type I(b) and type IV isotherms [196], with its hysteresis linked to slit-shaped pores, a characteristic commonly observed in commercial activated carbons [137].

Table 15 - Textural characteristics of the produced carbons

Sample	A_{BET}	V_{total}	V_{micro}	V_{meso}
	($m^2.g^{-1}$)		($cm^3.g^{-1}$)	
A405	73	0.133	0.008	0.125
B405	90	0.125	0.016	0.109
A405-CO_2	95	0.140	0.020	0.120
B405-CO_2	104	0.123	0.026	0.097
CAC	1030	0.56	0.30	0.26

The XRPD patterns shown in Figure 19 help identify the crystalline mineral phases in the produced materials. The broad peak between 20° and 30° is indicative of the amorphous carbon characteristic of these materials. Most other peaks are attributed to zinc sulphide (ZnS), which forms when ZnO in the rubber (used during vulcanisation) reacts with H_2S produced during pyrolysis [175,176,197]. Zinc silicate (willenite – Zn_2SiO_4) is also detected, which results from ZnO and SiO_2 reaction which is used in tyre manufacturing [177,198]. Furthermore, it is possible to theorise that in the activated chars, a shift from beta-ZnS to alpha-ZnS is observable due to the elevated temperatures applied in the activation process [199,200]. Likewise, a slight increase in ZnO content can be noted, attributed to its reaction with CO_2 [199,201], as described in equations 31 and 32:

$$Zn + CO_2 \leftrightarrow ZnO + CO \quad \text{(Eq. 31)}$$

$$2Zns + CO_2 \rightarrow 2ZnO + C + 2S \quad \text{(Eq. 32)}$$

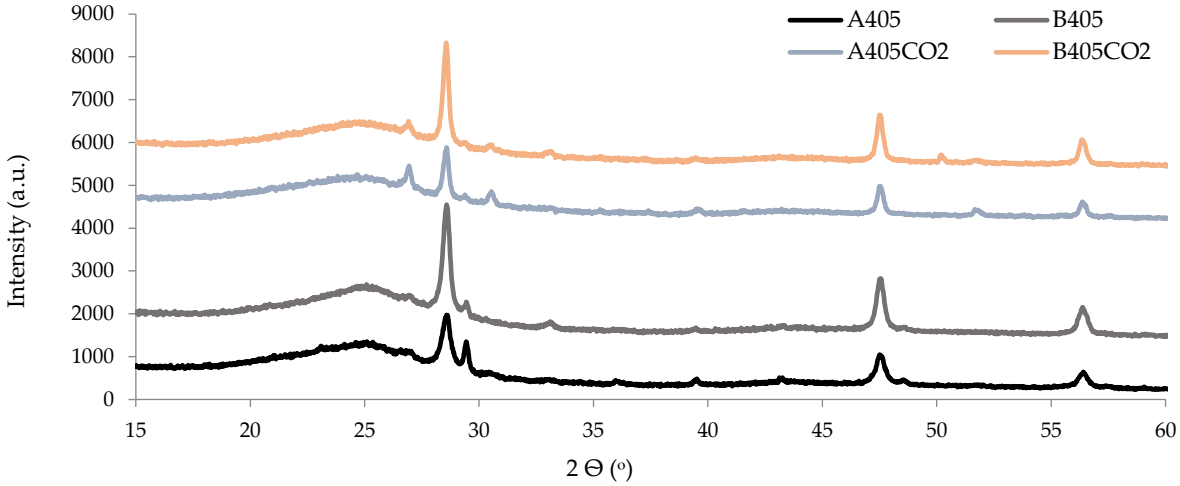

Figure 19 - X-ray powder diffraction patterns of produced materials

4.3 Magnet Leaching

The magnet leaching processes employed in this study followed a comprehensive literature review, and optimized parameters were selected. Initially, aqua regia was selected due to its capability to fully dissolve NdFeB magnets [143,202]. Subsequentially, assays with 3M HNO_3 were performed, due to its selectivity of leaving behind iron in the precipitate [145,203]. Moreover, HNO_3 leaching is a less demanding process in terms of energy and reagent consumption, and the literature suggests that this pathway might be a feasible approach for an industrial process [146].

According to Table 16, Fe constitutes the major element of the magnets (80.6% w/w), forming the bulk matrix. REEs were also present in the magnets, with Nd being the second most abundant element with 18.9% w/w, as it serves as the primary component for imparting magnetic properties.

Table 16 - Magnet composition and 3M HNO_3 leaching efficiency

	Al	**B**	**Co**	**Dy**	**Fe**	**Nd**	**Ni**	**Pr**
Magnet composition (w/w %)	0.41	0.69	0.59	1.21	80.6	18.9	0.03	1.50
3M HNO_3 leaching efficiency (%)	100	100	100	100	70.1	100	100	82.9

Dy (1.21% w/w) and Pr (1.50% w/w) were also detected in the magnet matrix, employed as additives to enhance magnetic properties, particularly by increasing the Curie point of the magnets and enabling them to withstand higher operating temperatures without

losing their capacities. Additionally, Al, B, Co, and Ni were present, albeit in trace amounts compared to REEs and Fe.

The data from the 3M HNO3 leaching efficiency reveals that Fe was not completely dissolved, with only 70.1% leaching. This outcome is viewed positively in the scope of this study, as its partial retention reduces competition during subsequent adsorption processes. Moreover, this partial dissolution offers the potential for recovering some Fe utilized in magnet manufacturing, thus enabling the recovery of an important by-product throughout the process. Additionally, a loss of 17.1% of Pr content from the magnets was recorded.

4.4 Mono-component batch adsorption assays

The four materials produced in this study were investigated in an adsorption study targeting Nd^{3+} and Dy^{3+} ions present in synthetic solutions, aiming to assess their effectiveness as REEs' adsorbents. Mono-component adsorption tests were carried out at the original pH of the synthetic solutions of Nd^{3+} and Dy^{3+} (pH_{Nd}=6.40, pH_{Dy}=7.36). Speciation diagrams for both Nd and Dy indicate that the predominant species are free-Nd^{3+} and free-Dy^{3+} up to pH 8. Beyond this pH, these elements begin to precipitate as hydroxides. However, the final pH recorded after each assay remained below this threshold, ensuring that no precipitation phenomena interfered with the adsorption mechanisms. Furthermore, the decision to maintain the natural pH of the synthetic solution was reinforced by the literature, suggesting that reducing the solution pH does not improve the recovery efficiency of these REEs [50].

Table 17 - Kinetics and isotherm data for the batch adsorption studies; Pseudo first order model, pseudo second order model, Langmuir model, and Freundlich model

		A405	B405	A405-CO2	B405-CO2
		Pseudo First Order			
Nd^{3+}	$q_{e,ajust}$ ($mg.g^{-1}$)	7.04	8.89	17.62	21.26
	$k_{ads\ ajust}$ (h^{-1})	17.79	2.00	0.26	0.10
	R^2	0.71	0.70	0.86	0.92
Dy^{3+}	$q_{e,ajust}$ ($mg.g^{-1}$)	7.04	8.94	18.13	27.29
	$k_{ads\ ajust}$ (h^{-1})	0.42	0.07	1.30	0.24
	R^2	0.98	0.97	0.67	0.85
		Pseudo Second Order			
Nd^{3+}	$q_{e,ajust}$ ($mg.g^{-1}$)	8.56	10.53	18.89	24.07
	$k_{ads\ ajust}$ (h^{-1})	0.26	0.14	0.22	0.01
	R^2	0.91	0.91	0.89	0.94
Dy^{3+}	$q_{e,ajust}$ ($mg.g^{-1}$)	7.67	10.54	18.41	30.97
	$k_{ads\ ajust}$ (h^{-1})	0.07	0.01	0.10	0.01
	R^2	0.99	0.98	0.76	0.92
		Langmuir			
Nd^{3+}	q_{max} ($mg.g^{-1}$)	6.97	7.63	40.91	27.36
	K_L ($L.mg^{-1}$)	0.66	1.68	0.07	0.14
	R^2	0.99	0.98	0.70	0.86
Dy^{3+}	q_{max} ($mg.g^{-1}$)	5.96	19.29	17.33	33.13
	K_L ($L.mg^{-1}$)	4.38	0.02	8.79	7.32
	R^2	0.96	0.93	0.66	0.90
		Freundlich			
Nd^{3+}	K_F ($mg^{1-1/n}.L^{1/n}.g^{-1}$)	5.18	3.97	12.47	13.11
	$1.n^{-1}$	0.06	0.17	0.23	0.13
	R^2	0.95	0.97	0.69	0.95
Dy^{3+}	K_F ($mg^{1-1/n}.L^{1/n}.g^{-1}$)	3.50	0.53	13.02	22.13
	$1.n^{-1}$	0.18	0.77	0.07	0.09
	R^2	0.95	0.93	0.61	0.78

Maximum uptake capacities of the produced materials, kinetic data, and isotherm data are shown in Table 17 and Figure 20 and Figure 21. Several conclusions can be drawn from these data: (i) The uptake capacities of Nd^{3+} and Dy^{3+} for the same type of materials (chars or ACs) are quite similar, with no significant differences observed between both ions. However,

a slightly higher affinity towards Dy^{3+} is noticeable, likely attributed to the difference in the ionic radius of both ions, with Dy^{3+} having slightly better access to the active sites on the materials [204]. (ii) Material B405 exhibits higher uptake capacities for both ions compared to char A405, a trend also observed in their activated counterparts, with B405-CO2 demonstrating superior uptake capacities over A405-CO2. (iii) The CO_2 activation of the materials resulted in an increase in the maximum uptake capacities of both ions, with at least a two-fold improvement observed across both materials. (iv) Among all the produced materials, B405-CO2 displayed the best overall performance, with maximum uptake capacities of 24.7 $mg.g^{-1}$ and 34.4 $mg.g^{-1}$ for Nd^{3+} and Dy^{3+}, respectively.

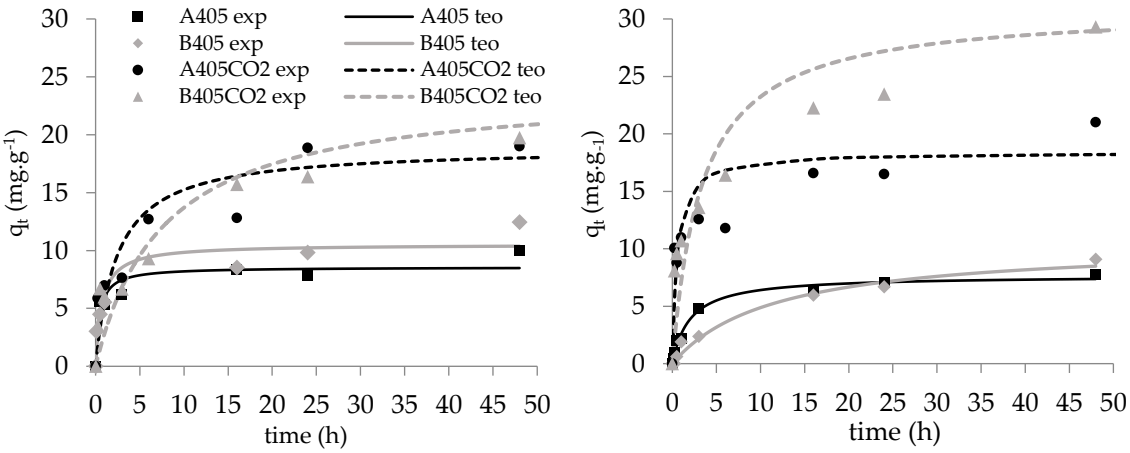

Figure 20 - Kinetic curves for the batch adsorption assays. Left- Dy^{3+} ;Right - Nd^{3+}

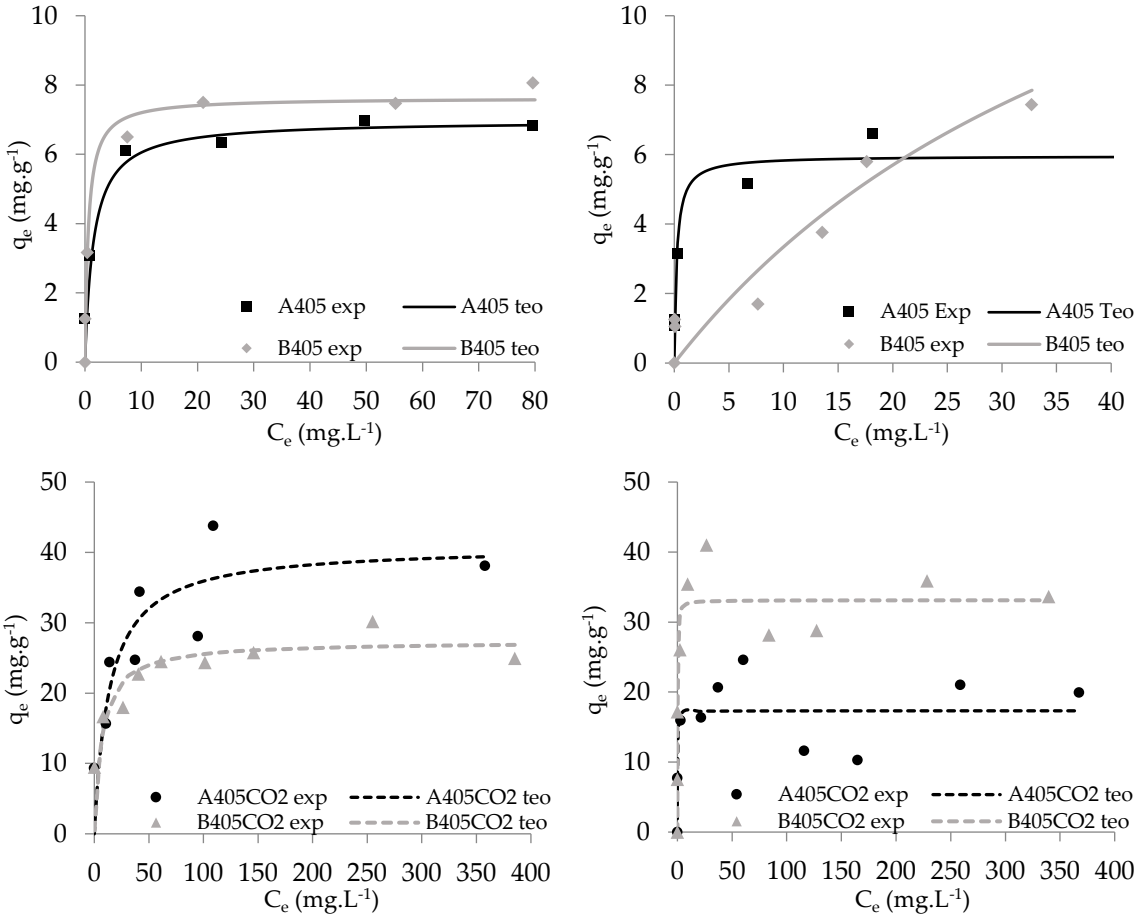

Figure 21 - Isotherms for the batch adsorption studies. Top - chars; Bottom - activated chars; Left - Dy^{3+}; Right - Nd^{3+} ;Points - experimental data; Lines - Langmuir model

In seeking to understand the adsorption mechanisms involved in the adsorption of Nd^{3+} and Dy^{3+}, several factors must be considered. Textural properties alone do not appear to be the determining factor as the activated chars exhibited similar surface areas and textural properties as the chars, and the CAC sample presented a very high surface area that does not correlate with adsorption capacities. This suggests that physisorption is unlikely to be the main adsorption mechanism. Furthermore, the analysis of the pH at the point of zero-charge (pH_{PZC}) reveals that they all exceed the pH of the REE solutions. Consequently, it is anticipated that the positively charged surface of the materials would repel Nd^{3+} and Dy^{3+}, excluding the electrostatic forces as attraction mechanisms. Therefore, it is plausible that the surface chemistry of the produced materials plays a pivotal role in the adsorption mechanisms. A suggested mechanism is a form of chemisorption, specifically an ion exchange mechanism [38]. The previous Chapter of this study delved deeper into these mechanisms using very similar materials. Ionic exchange assays were conducted and XPS was performed on the materials before and after the adsorption of Nd^{3+} and Dy^{3+} (Section 3.3.3). The study found

that Nd and Dy removal from the solution primarily occurred by exchanging with Zn ions present in the materials, and to a lesser extent with Ca ions. XPS analysis indicated that Nd and Dy were adsorbed in oxide form following the release of Zn and Ca.

The adsorption of Nd^{3+} and Dy^{3+} onto the adsorbents A405, B405, A405-CO2, and B405-CO2, was studied by using pseudo-first order, pseudo-second order, Langmuir, and Freundlich models (Table 17). Analysing the data from the kinetic models, it was revealed that the pseudo-second order model offered a superior fit to the experimental data compared to the pseudo-first order model for both ions and all materials investigated. This suggests that the adsorption process is more likely to follow chemisorption mechanisms rather than physical adsorption mechanisms, corroborating our previous findings.

The Langmuir and Freundlich isotherm models were employed to characterise the equilibrium adsorption behaviour of Nd^{3+} and Dy^{3+} ions. The Langmuir model assumes monolayer adsorption onto a homogeneous surface, while the Freundlich model describes heterogeneous adsorption onto a surface with multiple active sites. The results indicate that the Langmuir model provides a better fit to the experimental data than the Freundlich model, implying that the adsorption of Nd^{3+} and Dy^{3+} ions onto the materials studied may occur through monolayer coverage with uniform adsorption sites.

4.5 Column adsorption studies

Since the activated char B405-CO2 exhibited superior performance in the batch studies, it was decided to exclusively subject this material to dynamic adsorption studies. This focused approach allows for a more concentrated investigation into the behaviour and efficiency of this particular adsorbent under dynamic conditions.

Table 18 - Column adsorption assay parameters

	C_0 (mg.L^{-1})		B405CO2	CAC
		Single component		
Nd^{3+}	10	t_r (min)	7.20	-
		t_s (min)	74.6	-
		q_{max} (mg.g^{-1})	2.93	-
	2.5	t_r (min)	40.20	5.4
		t_s (min)	180.7	125.7
		q_{max} (mg.g^{-1})	3.48	1.14
Dy^{3+}	10	t_r (min)	7.90	-
		t_s (min)	102.4	-
		q_{max} (mg.g^{-1})	3.69	-
	2.5	t_r (min)	48.30	23.8
		t_s (min)	113.5	166.3
		q_{max} (mg.g^{-1})	1.87	1.40
		Bicomponent		
Nd^{3+} + Dy^{3+}				
Nd^{3+}	2.5	t_r (min)	11.90	-
		t_s (min)	180.5	-
		q_{max} (mg.g^{-1})	1.98	-
Dy^{3+}	2.5	t_r (min)	12.90	-
		t_s (min)	181.7	-
		q_{max} (mg.g^{-1})	2.30	-
Nd^{3+}	1.25	t_r (min)	30.40	11.9
		t_s (min)	144.2	180.5
		q_{max} (mg.g^{-1})	0.80	0.20
Dy^{3+}	1.25	t_r (min)	31.30	12.8
		t_s (min)	120.5	30.5
		q_{max} (mg.g^{-1})	0.90	0.30
		Real Leachate		
Nd^{3+}	1.25	t_r (min)	35.90	-
		t_s (min)	161.8	-
		q_{max} (mg.g^{-1})	1.36	-

4.5.1 Mono-component assays

The breakthrough curves for Nd^{3+} and Dy^{3+} are depicted in Figure 22 for both B405-CO2 and CAC adsorbents.

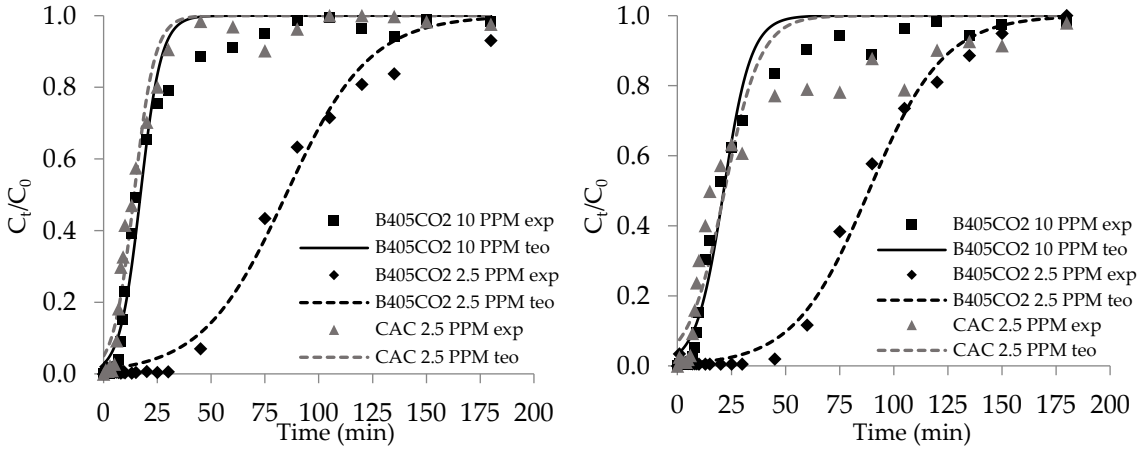

Figure 22 - Column adsorption breakthrough curves; left - Nd^{3+}; right - Dy^{3+}

(points – experimental data; lines – theoretical data from Thomas model)

Analysis of the data from the mono-component assays revealed that the adsorption behaviour was very similar between Nd^{3+} and Dy^{3+} for both adsorbents. Upon examining the different initial concentrations, C_0, it became apparent that reducing C_0 from 10 ppm to 2.5 ppm led to an increase in both the breakthrough and saturation times. For Nd^{3+}, the breakthrough and saturation times improved from 7.2 minutes and 74.6 minutes to 40.2 minutes and 180.7 minutes, respectively, representing a 458% increase for breakthrough and a 142% increase for saturation. Similar behaviour was observed for Dy^{3+}, where the same change in C_0 resulted in a 511% increase in breakthrough time and a 10.9% increase in saturation time. The maximum uptake capacity for Nd^{3+} was 3.5 $mg.g^{-1}$, while for Dy^{3+} was 3.7 $mg.g^{-1}$ (Table 18). These results, compared with the limited literature examples, demonstrate very promising outcomes, as the maximum uptake capacities and breakthrough times of B405-CO2 fall within the higher spectrum of reported results [49,205,206]. All experimental data fitted well with the Thomas model (R^2 values above 0.98 for all assays) (Table 19).

Table 19 - Column adsorption assays data and Thomas model

	C_0 (mg.L^{-1})		B405-CO2	CAC
		Single component		
Nd^{3+}	10	q_0 (mg.g^{-1})	2.24	-
		k_{th} (ml.min^{-1}.mg^{-1})	23.4	-
		R^2	0.98	-
	2.5	q_0 (mg.g^{-1})	2.65	0.43
		k_{th} (ml.min^{-1}.mg^{-1})	24.5	102.9
		R^2	0.99	0.98
Dy^{3+}	10	q_0 (mg.g^{-1})	2.74	-
		k_{th} (ml.min^{-1}.mg^{-1})	18.2	-
		R^2	0.98	-
	2.5	q_0 (mg.g^{-1})	2.54	0.72
		k_{th} (ml.min^{-1}.mg^{-1})	29.7	51.4
		R^2	0.99	0.94
		Bicomponent		
Nd^{3+} + Dy^{3+}				
Nd^{3+}	2.5	q_0 (mg.g^{-1})	0.67	-
		k_{th} (ml.min^{-1}.mg^{-1})	79.0	-
		R^2	0.98	-
Dy^{3+}	2.5	q_0 (mg.g^{-1})	0.74	-
		k_{th} (ml.min^{-1}.mg^{-1})	69.7	-
		R^2	0.98	-
Nd^{3+}	1.25	q_0 (mg.g^{-1})	0.71	0.39
		k_{th} (ml.min^{-1}.mg^{-1})	86.5	189.5
		R^2	0.99	0.99
Dy^{3+}	1.25	q_0 (mg.g^{-1})	0.80	0.48
		k_{th} (ml.min^{-1}.mg^{-1})	77.2	148.5
		R^2	0.99	0.99
		Real Leachate		
Nd^{3+}	1.25	q_0 (mg.g^{-1})	1.28	-
		k_{th} (ml.min^{-1}.mg^{-1})	51.1	-
		R^2	0.99	-

For benchmarking purposes, the CAC adsorbent was also evaluated, revealing that the adsorbent produced in this study exhibits much higher performance compared to the commercial alternative. The CAC adsorbent demonstrated maximum uptake capacities of 1.1 $mg.g^{-1}$ and 1.4 $mg.g^{-1}$ for Nd^{3+} and Dy^{3+}, respectively. This corresponds to a decrease of 68.6% and 62.1% compared to B405-CO2 under the same conditions.

4.5.2 Bicomponent assays

Analysing the data for the breakthrough curves in the bi-component assays (Figure 23), it was evident that when both Nd^{3+} and Dy^{3+} were present in the solution and competing for adsorption sites, no synergistic or antagonistic behaviours were observed.

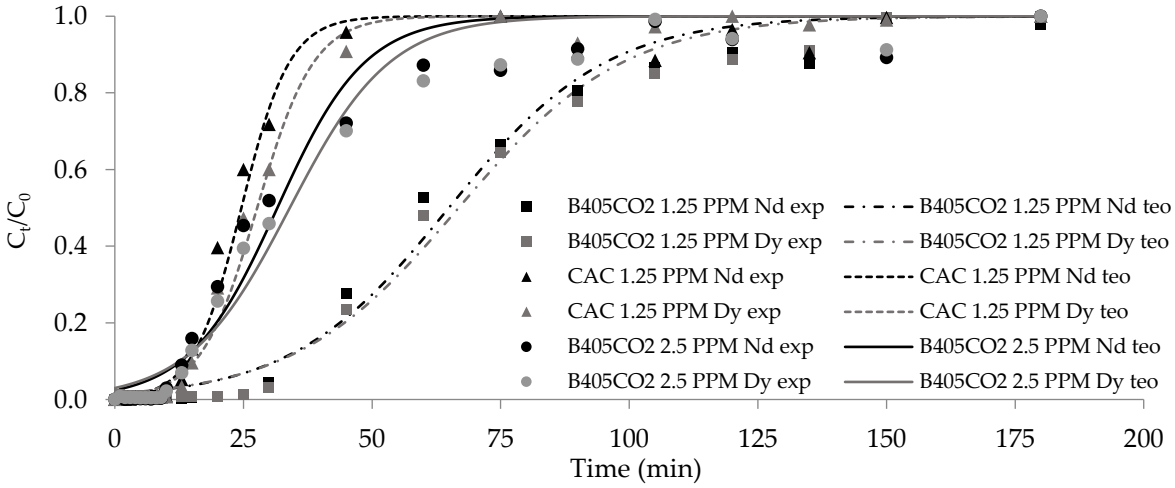

Figure 23 - Column adsorption breakthrough curves for bi-component assays (Nd^{3+} + Dy^{3+})

(points – experimental data; lines – theoretical data from Thomas model)

The adsorptive behaviour of both ions was very similar, although Dy^{3+} exhibited a slight preference. This observation is consistent with the results from the mono-component assays, as well as the discussion on the previous chapter, where the competitive adsorption of the same ions was investigated more extensively [38]. Similar to the mono-component assays, a reduction in the initial C_0 resulted in increases in breakthrough and saturation times. Regarding maximum uptake capacities, B405-CO2 demonstrated a value of 4.3 $mg.g^{-1}$ for both ions, divided into 2.0 for Nd^{3+} and 2.3 for Dy^{3+} (Table 18). This value is slightly higher than that recorded in the mono-component assays, possibly induced by a higher driving force due to a higher availability of adsorbate. These findings led to the conclusion that no adverse effects were observed when both REEs were present in solution, and that the adsorbents did

not exhibit a higher affinity for either ion. Once again, all data fitted well with the Thomas model (R^2 values above 0.98 for all conditions studied) (Table 19). Similarly, the CAC adsorbent displayed lower performance compared to B405-CO2, with maximum uptake capacities of 0.5 $mg.g^{-1}$ against 1.7 $mg.g^{-1}$ for the material produced in this study. This represents a decrease of 70.6% in performance, mirroring the results obtained in the mono-component assays.

4.5.3 Adsorption assay with real leachate

The leachates used in these assays were previously treated as described in section 2.6.2.3 to mimic the conditions used in the bi-component adsorption assays, with the same C_0 for Nd^{3+}, as this element presented a higher concentration in the magnets than Dy.

Analysing Figure 24, which illustrates the breakthrough curves for Nd^{3+} for both the magnet leachates and the synthetic solution, it became apparent that B405-CO2 exhibited a very positive performance in the magnet leachates.

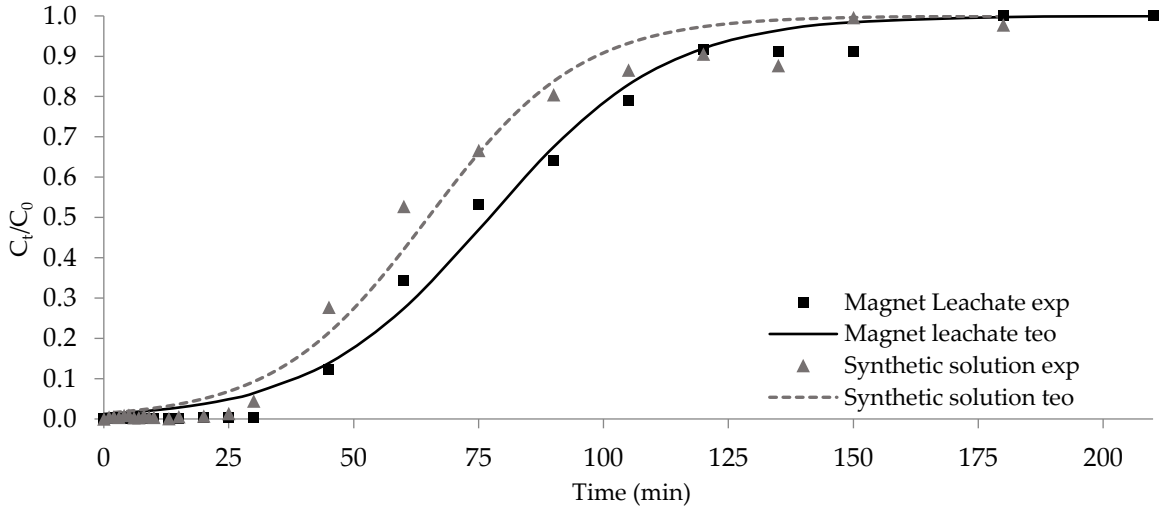

Figure 24 - Column adsorption breakthrough curves; magnet leachates; B405-CO2

(points – experimental data; lines – theoretical data from Thomas model)

Although the results were slightly inferior to those obtained with the synthetic solution, the difference was minimal. This demonstrates that in real-life scenarios, this adsorbent behaves similarly to synthetic scenarios, confirming that it is indeed feasible to use these assays as a method to further study and optimize this process in the laboratory. These results further establish that the adsorbent B405-CO2 works well when applied to real leachates.

The adsorbent B405-CO2 achieved an Nd^{3+} maximum uptake capacity of 1.36 $mg.g^{-1}$ in the magnet leachates (Table 18), a result only 20% lower than that recorded in synthetic solutions. Similarly, breakthrough and saturation times were slightly affected, with values for the magnet leachates of 25 and 129 minutes, respectively, representing a modest decrease of 18% and 10% compared to the synthetic solutions. The experimental data fit well to the Thomas model, with an R^2 value of 0.99 (Table 19).

Overall, these results yield a positive outcome for the scope of this work, demonstrating that this waste-derived adsorbent can perform effectively in real-eluates from magnets. Furthermore, the experimental data obtained in the synthetic assays aligns well with the real-world application, indicating the potential to promote the usage of this material and techniques beyond the laboratory. This transition to real applications could have a significant impact on promoting sustainability in the supply chain of critical raw materials and fostering a circular economy, while simultaneously addressing challenges in waste management.

4.6 Conclusions

This study demonstrates the successful transformation of spent tyre rubbers (STR) into valuable waste-derived adsorbents through pyrolysis and activation processes. The resulting materials exhibited remarkable efficacy in adsorbing rare earth elements (REEs), specifically neodymium (Nd^{3+}) and dysprosium (Dy^{3+}), from both synthetic solutions and real magnet leachates.

The synthesized waste-derived adsorbents, particularly the activated char B405-CO2, displayed superior performance compared to a commercially available activated carbon (CAC), underscoring the potential of STR-derived materials in environmental remediation and resource recovery efforts.

Moreover, dynamic column adsorption studies revealed consistent adsorption behaviour across varying solution compositions and conditions, reaffirming the versatility and robustness of these waste-derived adsorbents. The close correlation between laboratory findings and real-world eluate suggests the scalability and practical applicability of the developed adsorption process.

Moving forward, continued investigation into the potential applications of these materials in the energy production sector is on the horizon. Exploring the unique surface chemistry and adsorption properties of STR-derived adsorbents will be integral to understanding their suitability for catalysing important chemical reactions and processes. This ongoing exploration aligns with the trajectory of this investigation, paving the way for

potential advancements in the use of waste-derived catalysts, as well as providing another application to the produced materials, even after fulfilling their primary application.

In summary, this study highlights the transformative potential of repurposing spent tyre rubber into valuable waste-derived materials for addressing secondary raw materials valorisation and driving innovation across the value chains of tyres and electronic equipment. By valorising STR as a precursor for adsorbent materials, we not only mitigate environmental pollution but also promote sustainable practices and resource utilization, ushering in a more circular and environmentally sustainable future.

5

PHOTOCATALYTIC HYDROGEN PRODUCTION

This chapter presents an exploratory investigation into the potential application of carbon-based photocatalysts derived from spent tyre rubber for hydrogen production through photocatalytic water splitting. These assays represent a preliminary step toward assessing whether this innovative approach could serve as a viable method for further valorisation of the carbon materials, particularly after their use in REE adsorption.

Following the adsorption studies described in previous chapters, which focused on the removal of Nd and Dy from both synthetic and real magnet leachate solutions, it became clear that desorption techniques posed significant challenges. The primary adsorption mechanism was ion exchange with the mineral components present in the adsorbents [38]. Desorption methods, particularly acid stripping, were found to diminish the efficiency of the adsorbents by removing these essential minerals, rendering the materials less effective for subsequent use [207,208]. Recognizing that surface area alone was not the key determinant of REE adsorption capacity, the ion exchange mechanism was identified as the main contributor to the observed adsorption performance [209].

Given these limitations, this chapter explores a novel approach by repurposing these adsorbents post-REE adsorption, as well as pre-adsorption, as photocatalysts for hydrogen production. This initial investigation seeks to evaluate the feasibility of using REE-enriched carbon materials as photocatalysts. The assays conducted are exploratory, aimed at providing a preliminary understanding of the materials' photocatalytic properties, including hydrogen production rates, catalyst reusability, and basic kinetic modelling.

To analyse the results of these preliminary tests, a pseudo-homogeneous pseudo-first-order kinetic model was employed. This model simplifies the complexity of the heterogeneous photocatalytic system by assuming that the reaction occurs uniformly throughout the system, even though the actual process takes place at the surface of the solid catalyst. Additionally, the

model treats the reaction as first-order with respect to one reactant, further simplifying the analysis. While this approach represents a significant simplification of the true nature of the photocatalytic process, it provides a valuable framework for an initial evaluation of the photocatalytic performance and the potential scalability of this method for sustainable hydrogen production.

5.1 H_2 Production

Figure 25 displays the hydrogen production data from the photocatalytic assays performed using the materials B405, B405-CO_2, Nd@B405, and the reference catalyst ZnCdS (Zn:Cd 1:2). The results demonstrate that the photocatalysts produced in this study significantly outperformed the reference catalyst in terms of hydrogen production.

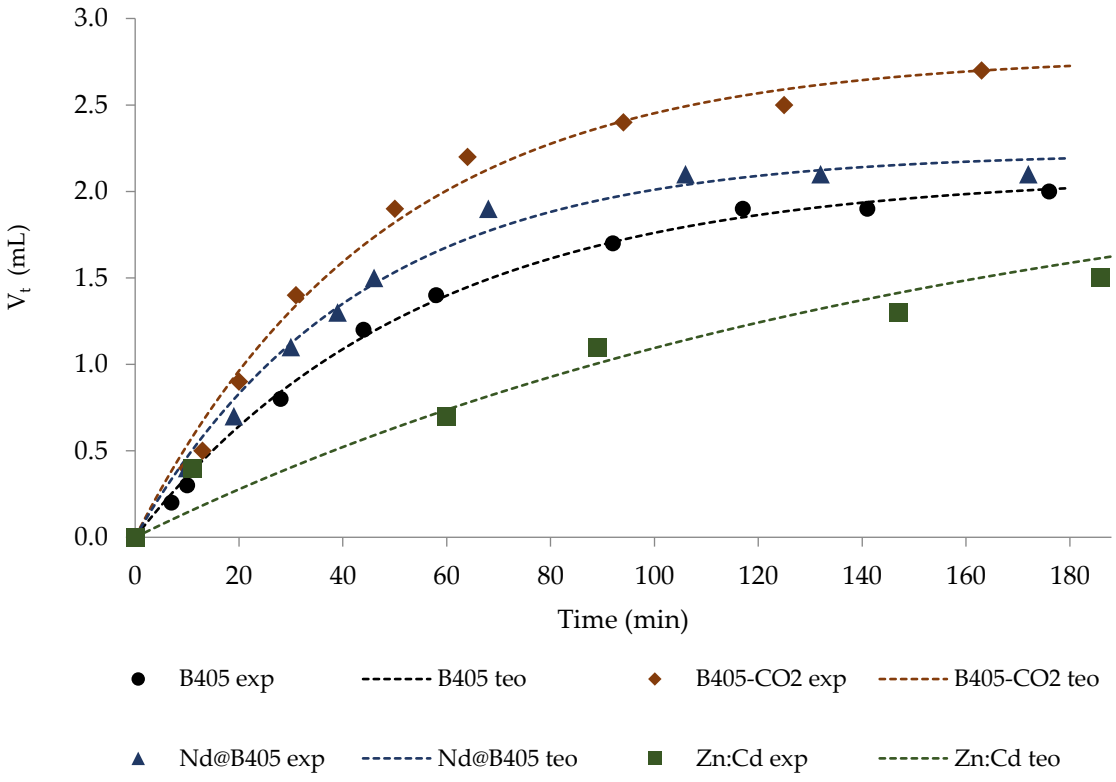

Figure 25 - Photocatalytic hydrogen production assay data (points - experimental data; lines- theoretical data)

The highest hydrogen volume after 120 minutes of light irradiation was achieved with B405-CO2, producing 2.48 mL of H_2, followed by Nd@B405 with 2.10 mL, B405 with 1.90 mL, and the reference catalyst with 1.22 mL. These results highlight the promising potential of the

materials developed in this thesis, as they consistently generated more hydrogen than the established reference photocatalyst [155,210–212].

Expressing these values as hydrogen production rates normalized by the mass of the catalyst, B405-CO2 achieved 24.4 mL $H_2.h^{-1}.g^{-1}$, Nd@B405 produced 20.6 mL $H_2.h^{-1}.g^{-1}$, B405 yielded 18.6 mL $H_2.h^{-1}.g^{-1}$, and the Zn:Cd catalyst produced 12.2 mL $H_2.h^{-1}.g^{-1}$. It is important to consider that in the case of the photocatalysts produced in this thesis, not all of the material is active in the photocatalytic reactions. In contrast, the reference material is entirely active in the process. Therefore, further analysis was conducted by normalizing the hydrogen production data to the mass of the active photocatalytic components.

This analysis was performed using the mineral composition data (Table 14), with specific reference to the Zn content in B405 and B405-CO2, as Zn is the active component in these materials [155,156,158,213]. For Nd@B405, the data was normalized based on the Nd content post-adsorption, excluding Zn due to the observed ion exchange processes during the adsorption of Nd, confirmed by XPS analysis (Section 3.3.3), which showed no detectable Zn post-Nd adsorption [38]. The Nd@B405 material contained 12.2 mg Nd per gram of photocatalyst.

When normalized by the active material, the hydrogen production rates were as follows: 12.2 mL $H_2.h^{-1}.g^{-1}$ for the reference catalyst, 202.9 mL $H_2.h^{-1}.g^{-1}$ for B405, 367.4 mL $H_2.h^{-1}.g^{-1}$ for B405-CO_2, and an impressive 1687.6 mL $H_2.h^{-1}.g^{-1}$ for Nd@B405. These results indicate that the photocatalysts developed in this study outperform the reference catalyst by at least an order of magnitude, with Nd@B405 showing a remarkable 13730% increase in hydrogen production efficiency compared to the ZnCdS catalyst.

The superior performance of B405-CO2, despite its lower Zn content (67.5 $mg.g^{-1}$) compared to B405 (93.5 $mg.g^{-1}$), can be attributed to several factors. The activation process, conducted at high temperatures (900 °C) with CO_2, likely facilitated the removal of residual oils and organic material that remained on the surface of the B405 char after pyrolysis [214]. These residues hinder the effective dispersion of B405 in the aqueous phase, limiting its photocatalytic efficiency. In contrast, the activation process not only reduced the hydrophobicity of B405-CO2 but also increased its porosity, thereby improving the accessibility of active sites and functional groups essential for the photocatalytic reactions [116,117,154,214].

In the case of Nd@B405, the substantial enhancement in hydrogen production relative to B405 and B405-CO2 suggests that neodymium acts as a highly effective photocatalytic component [119]. The ion exchange process, whereby Zn is replaced by Nd during adsorption, results in a material with negligible Zn content but significantly enhanced photocatalytic activity. While precise quantification of the remaining Nd and Zn in Nd@B405 would require

further analysis, such as acid digestion followed by ICP, the preliminary data strongly indicates that Nd plays a critical role in boosting the photocatalytic efficiency of this material.

These findings underscore the dual functionality of the materials produced in this study, serving both as effective adsorbents for rare earth element recovery and as highly efficient photocatalysts for hydrogen production. The exceptional performance of Nd@B405, in particular, demonstrates the potential for post-adsorption utilization of these materials to enhance photocatalytic systems for H_2 production. This multifunctionality aligns with the principles of a circular economy, where waste-derived materials are repurposed for multiple high-value applications.

5.2 Photocatalyst Reusability

The reusability of the photocatalysts is a critical factor in assessing their potential for practical applications, particularly in sustainable energy production [154,210,212]. To evaluate this, the hydrogen production capability of each photocatalyst—B405, B405-CO2, and Nd@B405—was assessed over three consecutive cycles, each lasting 120 minutes. The results are displayed in Figure 26.

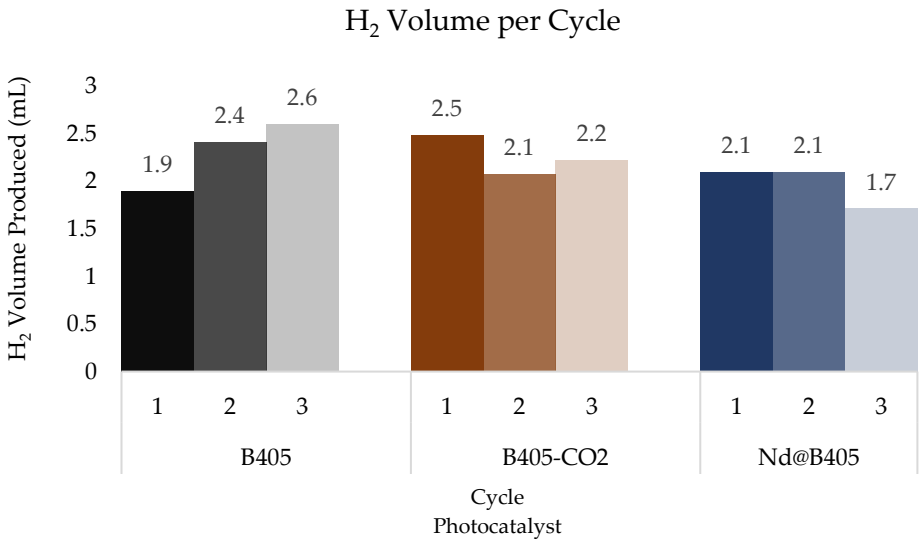

Figure 26 - Produced H_2 volume at 120 minutes for each cycle

The B405 photocatalyst demonstrated an increase in hydrogen production with each subsequent cycle. The volume of hydrogen produced after 120 minutes increased from 1.90 mL in the first cycle to 2.41 mL in the second cycle and reached 2.60 mL in the third cycle.

This trend suggests that the B405 material may undergo an activation process or a gradual enhancement in catalytic efficiency during repeated use. The observed increase in hydrogen production could be attributed to the progressive exposure of more active sites as the surface of the photocatalyst interacts with the sacrificial solution and the removal of any surface-adsorbed species that may initially hinder catalytic activity [157].

In contrast, the B405-CO2 photocatalyst exhibited a slight decline in hydrogen production after the first cycle. The initial hydrogen production of 2.48 mL decreased to 2.08 mL in the second cycle and then increased to 2.23 mL in the third cycle. The decrease in performance after the first cycle could be due to the partial blocking of active sites or the adsorption of reaction intermediates or by-products that reduce the material's catalytic efficiency [210]. However, the slight recovery observed in the third cycle suggests that the photocatalyst may regain some of its activity, potentially due to the desorption of these species or the re-exposure of active sites.

The Nd@B405 photocatalyst showed consistent hydrogen production in the first two cycles, with a stable output of 2.10 mL of hydrogen after 120 minutes. However, in the third cycle, there was a noticeable decline in performance, with hydrogen production decreasing to 1.71 mL. This decline may indicate that the Nd@B405 material undergoes some form of deactivation over time, possibly due to the loss of neodymium from the surface or changes in the surface chemistry that negatively affect its photocatalytic activity. The stability observed in the first two cycles suggests that while the material initially maintains its activity, prolonged use may lead to wear or alteration in its catalytic properties.

The results of the reusability assays reveal distinct behaviours among the three photocatalysts. The B405 material shows improved hydrogen production with each cycle, likely due to gradual activation or exposure of active sites. In contrast, B405-CO_2 exhibits a slight decline after the first cycle, followed by partial recovery, suggesting a balance between deactivation and reactivation processes. Nd@B405 remains stable over the first two cycles but experiences a noticeable drop in the third, indicating potential challenges in maintaining long-term activity, particularly in REE-loaded catalysts. Nevertheless, these results are promising for the reusability of these photocatalysts in subsequent production cycles, especially for applications where consistent performance across multiple cycles is critical.

5.3 Modelling

To better understand the kinetics of hydrogen production in the photocatalytic assays, a Pseudo-Homogeneous Pseudo-First-Order Kinetic Model, modified for H_2 production, was applied to the experimental data. This model was tested in both its linear and non-linear forms to determine the rate constants and the maximum hydrogen production (V_{max}) for each photocatalyst: B405, B405-CO2, Nd@B405, and the ZnCdS reference catalyst. The results of the model fitting are presented in Table 20, and the non-linear theoretical data is represented in Figure 25 by dashed lines.

Table 20 - Pseudo-First-Order Kinetic Model data for the H_2 production assays

	B405	**B405-CO2**	**Nd@B405**	**Zn:Cd**
	Pseudo-First-Order Linear			
$V_{max,ajust}$ (mL)	2.21	2.72	2.16	2.24
$k_{H2\ ajust}$ (h^{-1})	0.988	1.192	1.805	0.643
R^2	0.98	0.98	0.92	0.83
	Pseudo-First-Order Non-Linear			
$V_{max,ajust}$ (mL)	2.1	2.79	2.22	2.33
$k_{H2\ ajust}$ (h^{-1})	1.098	1.1271	1.402	0.38
R^2	0.99	0.99	0.99	0.96

The pseudo-first-order linear model provided a good fit for most of the photocatalysts, with R^2 values ranging from 0.83 to 0.98. Among the tested materials, B405-CO2 exhibited the highest adjusted V_{max} of 2.72 mL, closely followed by the Zn:Cd catalyst at 2.24 mL. The corresponding rate constants ($k_{H2\ ajust}$) indicated that Nd@B405 had the highest rate of hydrogen production with a k_{H2} of 1.805 h^{-1}, which suggests that this material promotes a faster reaction rate, although its V_{max} was slightly lower than that of B405-CO2.

The relatively high R^2 values for B405 and B405-CO2 (both at 0.98) indicate a strong correlation between the model and the experimental data, supporting the suitability of the linear kinetic model for these materials. However, the lower R^2 value of 0.83 for Zn:Cd reference catalyst suggests a less accurate fit, indicating that other kinetic factors might be influencing hydrogen production for this reference catalyst.

The pseudo-first-order non-linear model yielded even higher R^2 values across all materials, with values ranging from 0.96 for Zn:Cd to 0.99 for the other photocatalysts, indicating an excellent fit to the experimental data. This improved fit suggests that the non-

linear approach more accurately captures the complex kinetics of hydrogen production in these systems.

In the non-linear model, B405-CO2 again showed the highest V_{max} at 2.79 mL, confirming its superior hydrogen production capability. Nd@B405 maintained a strong performance with a V_{max} of 2.22 mL and a k_{H2} of 1.402 h^{-1}, albeit slightly lower than in the linear model. Interestingly, the Zn:Cd catalyst showed a higher V_{max} in the non-linear model (2.33 mL) compared to the linear model, along with an R^2 value of 0.96, which suggests that the non-linear model provides a better description of the photocatalytic kinetics for this reference material.

The application of both linear and non-linear pseudo-first-order kinetic models has provided valuable insights into the hydrogen production capabilities and reaction kinetics of the studied photocatalysts. The superior fit of the non-linear model across all materials suggests that the kinetics of photocatalytic hydrogen production in these systems are not strictly linear and may involve more complex reaction dynamics. The results highlight B405-CO2 as the most effective photocatalyst in terms of both hydrogen production capacity and reaction rate, followed closely by Nd@B405.

These findings not only validate the experimental observations but also underscore the importance of selecting appropriate kinetic models when evaluating photocatalytic systems. The differences in the kinetic parameters between the linear and non-linear models also suggest that further refinement and testing of more advanced kinetic models may be warranted to fully capture the behaviour of these materials under various operational conditions [154,161–163,215–217].

5.4 Conclusions

The carbon-based materials derived from spent tyre rubber have demonstrated promising photocatalytic potential for hydrogen production. Their performance in photocatalytic water splitting indicates that these materials could play a significant role in sustainable energy generation. The results suggest that waste-derived carbon materials are not only viable but also effective in promoting hydrogen evolution, marking an important step forward in renewable energy technologies.

Among the various photocatalysts tested, the materials produced in this research exhibited the highest hydrogen production rates compared to the reference catalyst. Specifically, the photocatalysts produced through CO_2 activation methods demonstrated superior activity, achieving hydrogen evolution rates of 24.4 mL $H_2.h^{-1}.g^{-1}$. The REE-enriched

char, Nd@B405, also achieved notable hydrogen production rates, with values reaching 20.6 mL $H_2.h^{-1}.g^{-1}$. Additionally, the reusability of these photocatalysts was confirmed, with minimal loss of activity observed over multiple cycles, underscoring their durability and potential for long-term application.

Overall, these findings highlight the feasibility of using waste-derived carbon materials in photocatalytic applications, offering a scalable and environmentally friendly approach to hydrogen production. This work lays the groundwork for further optimization and large-scale implementation of these materials in sustainable energy systems.

6

GENERAL CONCLUSIONS

This doctoral research thesis addresses critical environmental and technological challenges by exploring innovative methods for valorising spent tyre rubber through the production of porous carbons and utilizing these materials for the recovery of REEs from e-waste, as well as their application in photocatalytic hydrogen production. The integration of these waste streams into a circular economy framework demonstrates the potential for sustainable chemistry to contribute significantly to resource management and energy production. The research not only provides a proof-of-concept for these processes on a laboratory scale but also lays a solid foundation for future industrial applications.

The principal aim of this thesis was to develop processes that could transform waste materials, specifically spent tyre rubber, into valuable resources. By successfully producing waste derived porous carbons, assessing their properties for specific applications, and demonstrating their effectiveness in REE recovery and hydrogen production, this work contributes to the fields of material science, environmental engineering, and sustainable chemistry. The dual focus on resource recovery and energy sustainability aligns with global efforts to transition towards more sustainable industrial practices, making the findings of this research relevant and timely.

The production of porous carbons from spent tyre rubber through pyrolysis and subsequent activation represents a significant achievement in the valorisation of this abundant waste material. Two pyrolysis processes were studied, and the resulting chars were tested in further applications. Both physical and chemical activation techniques were employed, with physical activation, particularly using CO_2, proving to be the most effective in enhancing the properties of the resulting carbon materials.

The porous carbons produced exhibited remarkable properties, with specific surface areas and chemistry that were conducive to high adsorption capacities. The materials were

characterized using a range of analytical techniques, including nitrogen adsorption-desorption isotherms, SEM, XPS and XRPD, which confirmed the potential of these porous and chemically active carbon structures. The successful transformation of spent tyre rubber into such high-value materials underscores the potential for these processes to be scaled up and integrated into industrial waste management systems.

Moreover, the abilities of these carbons offer significant advantages for their application in various fields, including catalysis, adsorption, and energy production. The findings from this research suggest that the use of spent tyre rubber as a precursor for porous carbon production not only provides a sustainable solution for waste management but also opens up new avenues for the development of advanced materials with broad industrial applications.

On the adsorption of REEs, the studies conducted as part of this research demonstrated the effectiveness of the produced porous carbons in recovering neodymium and dysprosium from e-waste leachates. These rare earth elements are critical for various high-tech applications, yet their supply is limited, making their recovery from secondary sources a priority. The porous carbons produced from spent tyre rubber proved to be highly effective adsorbents, with significant uptake capacities for both Nd and Dy.

Batch adsorption assays were initially conducted to evaluate the performance of the carbons under controlled conditions. The results indicated that the physically activated carbons, particularly those activated with CO_2, exhibited superior adsorption capacities compared to their counterparts, achieving maximum adsorption capacities of 24.7 $mg.g^{-1}$ for Nd^{3+} and 34.4 $mg.g^{-1}$ for Dy^{3+}. The adsorption capacities were found to be highly dependent on the surface chemistry of the carbons, with the mineral composition playing a crucial role in enhancing the adsorption of REE ions.

Dynamic adsorption assays, which more closely simulate real-world conditions, were also performed to assess the practical applicability of these materials in continuous systems. These studies confirmed the high efficiency of the porous carbons in REE recovery, demonstrating their potential for use in industrial-scale processes. The dynamic adsorption experiments provided valuable insights into the kinetics of REE adsorption under continuous operation. The material B405-CO2 demonstrated to be the better adsorbent, achieving maximum uptake capacities of 3.48 $mg.g^{-1}$ for Nd^{3+} and 3.69 $mg.g^{-1}$ for Dy^{3+} in the synthetic solutions, and 1.36 $mg.g^{-1}$ for Nd^{3+} in the real magnet leachates.

The adsorption mechanisms were further elucidated through a combination of experimental data and modelling. It was determined that the adsorption of REEs onto the porous carbons occurs mainly via chemisorption, through an ion exchange mechanism. The physical proprieties of the carbon materials, allowed for the initial attraction of REE ions to the carbon surface, while their surface chemistry, ensures the stable attachment of these ions to the adsorbent, involving the formation of stronger chemical bonds. Mainly, an ion exchange mechanism, facilitated by the presence of specific mineral species in the carbon matrix, contributed to the efficient recovery of REEs from solution.

Overall, the research has demonstrated that porous carbons derived from spent tyre rubber are not only effective adsorbents for REE recovery but also offer a sustainable and cost-effective alternative to traditional methods. The success of these materials in capturing REEs from waste streams highlights their potential for broader applications in the recycling of other valuable metals and the purification of industrial effluents.

The application of the produced carbon materials and REE-enriched porous carbons as photocatalysts for hydrogen production represents a novel and promising approach to sustainable energy generation. The photocatalytic assays conducted in this research revealed that these materials are highly effective in photocatalysing the production of hydrogen from water under light irradiation. The integration of REEs into the carbon matrix was found to enhance the photocatalytic performance of these systems, likely due to the unique electronic properties of the REEs, which facilitate charge separation and transfer during the photocatalytic process.

The photocatalytic hydrogen production was investigated with various materials, namely the char B405, the AC B405-CO2, the Nd loaded char Nd@B405, and a reference catalyst, with the results indicating that these carbons materials not only exhibit high catalytic activity but also demonstrate excellent stability and reusability over multiple cycles. This is a crucial advantage for the practical application of these materials, as it suggests that they could be used in long-term processes without significant degradation in performance.

This research has demonstrated that the combination of porous carbons and REEs offers a highly effective and sustainable approach to photocatalytic hydrogen production. The findings contribute to the growing body of knowledge on the use of carbon-based materials in energy applications and suggest that further exploration of these materials could lead to the development of more efficient and scalable hydrogen production technologies.

The specific conclusions drawn from each area of this research converge to illustrate the multi-layered potential of porous carbons derived from waste materials. The successful recovery of REEs, combined with their subsequent use in photocatalytic hydrogen production, exemplifies the principles of green chemistry and the circular economy. By integrating waste valorisation, resource recovery, and energy generation into a cohesive framework, this thesis offers a potential solution to some of the most pressing challenges in sustainable development.

The interconnectedness of the different research areas is particularly evident in the way that the properties of the porous carbons influence their performance in both adsorption and catalysis. The properties and surface chemistry that make these materials effective adsorbents for REEs also contribute to their catalytic activity in hydrogen production. This dual functionality underscores the versatility of porous carbons and highlights their potential for use in a wide range of applications beyond those explored in this thesis.

Furthermore, the research demonstrates that sustainable practices can lead to the development of advanced materials with high-added value. By transforming waste materials into functional products, this work aligns with global efforts to reduce waste, conserve resources, and promote sustainable industrial practices. The findings of this research not only contribute to the scientific understanding of material transformation and application but also provide practical insights that could inform policy and industry practices in the future.

In conclusion, this thesis has successfully demonstrated the viability of using spent tyre rubber as a precursor for high-performance porous carbons and their application in REE recovery and photocatalytic hydrogen production. The research contributes to the growing body of knowledge on sustainable material science and green chemistry, offering new pathways for the valorisation of waste materials and the development of sustainable energy technologies.

The findings of this research have significant implications for the future of waste management and resource recovery. By demonstrating that waste materials can be transformed into valuable resources with broad industrial applications, this work provides a strong case for the adoption of circular economy principles in industrial processes. The positive results obtained in this research underscore the potential for sustainable approaches to address critical challenges in resource management and energy production.

Future research should focus on scaling up these processes and optimizing the operational conditions for industrial applications. This includes exploring the feasibility of using these materials in other catalytic and adsorption processes, as well as investigating the potential for integrating these technologies into existing industrial systems. Additionally, further studies on the environmental and economic impacts of these processes will be essential

to ensure their sustainability and scalability. These topics will be addressed in the next Chapter - Suggestions for Future Work.

Overall, this research represents a significant step forward in the development of sustainable technologies for waste management, resource recovery, and energy production. By bridging the gap between laboratory research and real-world applications, this thesis has the potential to contribute to a more sustainable and resilient future.

7

SUGGESTIONS FOR FUTURE WORK

The research presented in this thesis has laid a solid foundation for the valorisation of spent tyre rubber through the production of porous carbon materials, the recovery of REEs from electronic waste, and their application in photocatalytic hydrogen production. While the findings are promising and demonstrate significant potential for industrial application, several avenues remain unexplored. These future considerations aim to expand the scope of this research, optimize the processes, and explore new applications for the materials and methodologies developed.

Scaling Up and Process Optimization

One future direction for this research is the scaling up of the processes developed during the thesis. While the laboratory-scale experiments provided valuable insights, translating these findings into industrial-scale operations requires further research. This includes the up-scaling to pilot-scale assays to test the feasibility of large-scale production of porous carbons from spent tyre rubber and their subsequent use in REE recovery and photocatalytic hydrogen production.

Process optimization will also be critical in this transition. The pyrolysis, and activation processes in particular, should be optimized to maximize yield, improve energy efficiency, and reduce operational costs. This may involve exploring alternative activation agents, optimizing pyrolysis temperatures, and improving reactor designs to enhance the quality and performance of the resulting carbon materials. Additionally, the optimization of adsorption and photocatalytic processes will be necessary to ensure that these materials perform effectively in real-world applications.

Expanding the Range of Waste Precursors

While spent tyre rubber has been the focus of this research, there is significant potential to explore other waste materials as precursors for the production of porous carbons. Agricultural residues, industrial by-products, other forms of biomass, and various waste products could be investigated as alternative feedstocks. The use of diverse waste materials could enhance the sustainability and versatility of the process, allowing for the production of tailored carbon materials with specific properties suited to various applications.

Exploring different waste precursors will also provide insights into the adaptability of the pyrolysis and activation processes developed in this thesis. By broadening the range of materials that can be valorised, this research could contribute to a more comprehensive circular economy framework, addressing the challenges of waste management across multiple industries.

Advanced Characterization and Functionalization of Porous Carbons

The characterization of porous carbons in this thesis focused on their structural properties, surface area, and chemical composition. Future research should dive deeper into understanding the surface chemistry of these materials, particularly the functional groups that contribute to their adsorption and catalytic properties. Advanced spectroscopic techniques, such as X-ray photoelectron spectroscopy (XPS) and nuclear magnetic resonance (NMR), could be employed to gain a more detailed understanding of the interactions between REEs and the carbon surface.

Additionally, functionalization of the porous carbons could be explored as a means of enhancing their performance. Chemical modification of the carbon surface to introduce specific functional groups could improve the adsorption capacity for REEs and increase the efficiency of photocatalytic processes. Functionalization could also enable the development of carbon materials for new applications, such as environmental remediation, sensing, or energy storage.

Exploring New Applications

The porous carbons developed in this thesis have shown promise in REE recovery and photocatalytic hydrogen production, but their potential extends far beyond these applications. Future research could explore the use of these materials in other areas, such as:

i. Environmental Remediation: The high adsorption capacity and surface reactivity of these carbons could be harnessed for the removal of pollutants from water and air. This includes the adsorption of heavy metals, organic

contaminants, and emerging pollutants such as pharmaceuticals and microplastics.

ii. Energy Storage: The porous structure and surface chemistry of these carbons make them suitable candidates for use in supercapacitors and batteries. Research could focus on optimizing the electrochemical properties of these materials to improve energy storage performance.

iii. Catalysis: Beyond photocatalysis, the carbons could be used as supports for various catalytic processes, including oxidation, reduction, and organic synthesis reactions. Investigating the catalytic activity of these materials in different chemical pathways could open up new industrial applications.

iv. Gas Separation and Storage: The porosity and surface chemistry of these carbons could be applied in gas separation and storage technologies, particularly for gases such as CO_2, H_2, and CH_4. This could contribute to advancements in carbon capture and storage (CCS), hydrogen economy technologies, and biofuel upgrading.

Environmental and Economic Assessment

If the processes developed in this thesis aim to move towards industrial application, it will be essential to conduct comprehensive environmental and economic assessments. Life cycle assessment (LCA) and techno-economic analysis (TEA) should be employed to evaluate the sustainability and economic viability of the processes. These assessments will help identify potential environmental impacts, optimize resource use, and determine the economic feasibility of scaling up the technology.

Additionally, exploring the economic incentives and market opportunities for the materials and processes developed in this research could facilitate their adoption by industry. Understanding the regulatory landscape, potential funding sources, and market demand will be critical for the successful commercialization of these technologies.

8

DISSEMINATION

The research presented in this thesis has significantly contributed to the field of sustainable chemistry, particularly in the areas of waste valorisation and REE recovery. The outcomes of this work have been disseminated through various academic channels to ensure the broadest possible impact and engagement within the scientific community.

This research has yielded four peer-reviewed publications in high-impact journals, each addressing critical aspects of the study, from the development of porous carbons derived from spent tyre rubber to the efficient recovery of neodymium and dysprosium from end-of-life electronic waste. These publications have undergone peer review, underscoring the scientific rigor and innovation embedded in the research.

The findings have also been presented at four international scientific conferences, facilitating the exchange of ideas with leading experts. Additionally, the research was disseminated through a specialized webinar and an academic seminar, both of which provided platforms to engage with a broader audience, including industry professionals and fellow researchers, highlighting the practical applications and potential for future innovations stemming from this work.

This thesis synthesizes these contributions, providing a comprehensive account of the research and its implications, thereby serving as a definitive reference for future studies in sustainable material recovery and circular economy practices.

8.1 Papers

This section lists the peer-reviewed papers published from this research, as follows:

1. Bernardo M., Lapa N., Pinto F., Nogueira M., Matos I., Ventura M., Ferraria A.M., do Rego A.M.B., Fonseca I.M. (2023) Valorisation of spent tire rubber as carbon adsorbents for Pb(II) and W(VI) in the framework of a Circular Economy. *Environmental Science and Pollution Research*, 30 (30), 74820 – 74837. DOI: https://doi.org/10.1007/s11356-023-27689-5
   Candidate's Contribution: Conducted rubber and char characterization, performed leaching assays, and prepared the first draft of the manuscript.

2. Nogueira, M., Matos, I., Bernardo, M., Tarelho, L.A.C., Ferraria, A.M., Botelho do Rego, A.M., Fonseca, I., Lapa, N. (2023) Recovery of rare earth elements (Nd^{3+} and Dy^{3+}) by using carbon-based adsorbents from spent tire rubber. *Waste Management*, 174, 451-461. DOI: https://doi.org/10.1016/j.wasman.2023.12.025
   Candidate's Contribution: Conducted rubber and char characterization, performed all adsorption and leaching assays, organized and processed the experimental data, drafted the manuscript, and managed editing and formatting.

3. M. Nogueira, I. Matos, M. Bernardo, F. Pinto, I. Fonseca., and N. Lapa; Recovery of Nd^{3+} and Dy^{3+} from E-Waste using Adsorbents from Spent Tyre Rubbers: Batch and Column Dynamic Assays; *Molecules;* 2024; doi: 10.3390/molecules30010092
   Candidate's Contribution: Conducted rubber, char, and AC characterization, performed the physical activation of ACs, carried out all adsorption assays, disassembled magnets, performed magnet leaching assays, organized and processed the experimental data, drafted the manuscript, and managed editing and formatting.

4. M. Nogueira, M. Bernardo, M. Ventura, I. Matos, F. Pinto and N. Lapa, (2024) Opportunities and Constraints of the Adsorption of Rare Earth Elements onto Pyrolytic Carbon-Based Materials: A Mini-Review, *Processes*, 12, 2257, doi.org/10.3390/pr12102257
   Candidate's Contribution: Conducted the literature review and search, organized all the data, drafted the manuscript, and handled editing and formatting.

8.2 Conferences

This section highlights the international conferences where the research was presented, as follows:

1. ***Thessaloniki 2021* - 8th International Conference on Sustainable Solid Waste Management** (Thessaloniki, Greece):
   Title: *Recovery of Rare Earth Elements (Nd^{3+} and Dy^{3+}) by Adsorption Using Waste Derived Carbon Adsorbents*
   Authors: M. Nogueira, N. Lapa, I. Matos, M. Bernardo, F. Pinto, I. Fonseca
   Candidate's Contribution: Wrote the abstract, prepared the presentation, and delivered the oral presentation.

2. ***Wastes* 2023 - Solutions, Treatments & Opportunities** (Coimbra, Portugal):
   Title: *Adsorption of Rare Earth Elements onto Spent Tyre Rubber Adsorbents: A Sustainable Approach for Critical Element Recovery*
   Authors: M. Nogueira, I. Matos, M. Bernardo, L. Tarelho, A.M. Ferraria, A.M.B. Rego, I. Fonseca, N. Lapa
   Candidate's Contribution: Wrote the abstract, prepared the presentation, and delivered the oral presentation.

3. ***ChemPor* 2023 - 14th International Chemical and Biological Engineering Conference** (Bragança, Portugal):
   Title: *Waste-Derived Carbon Materials for Adsorptive Recovery of Rare Earth Elements*
   Authors: M. Nogueira, M. Bernardo, F. Pinto, I. Fonseca, N. Lapa, I. Matos
   Candidate's Contribution: Wrote the abstract, prepared the presentation, and delivered the oral presentation.

4. ***Rhodes 2024* – 11th International Conference on Sustainable Solid Waste Management** (Rhodes, Greece):
   Title: *Recovery of Rare Earth Elements from E-Waste using Tire Rubber-Derived Carbon Adsorbents*
   Authors: Nogueira, M., Bernardo, M., Pinto, F., Fonseca, I., Lapa, N., Matos, I.
   Candidate's Contribution: Wrote the abstract, prepared the presentation, and delivered the oral presentation.

8.3 Webinars and Seminars

This section covers the webinars and seminars where the research was discussed, as follows:

1. **Webinar LAQV** (Laboratório Associado para a Química Verde) **2023** (NOVA FCT, Monte de Caparica, Portugal):

   Title: *Recovery of Rare Earth Elements (Nd^{3+} and Dy^{3+}) by Using Waste-Derived Carbon Adsorbents*

   Authors: M. Nogueira, I. Matos, M. Bernardo, F. Pinto, L. Tarelho, I. Fonseca, N. Lapa

   Candidate's Contribution: Wrote the abstract, prepared the presentation, and delivered the oral presentation.

2. **1st Seminar on *Impacts and Valorization of E-Waste 2023*** (Universidade de Aveiro, Portugal):

   Title: *Recovery of rare earth elements through adsorption within a circular economy approach*

   Authors: M. Nogueira, I. Matos, M. Bernardo, F. Pinto, L. Tarelho, I. Fonseca, N. Lapa

   Candidate's Contribution: Wrote the abstract, prepared the presentation, and delivered the oral presentation.

BIBLIOGRAPHY

1. Valorpneu *RELATÓRIO ANUAL DE ATIVIDADES 2021*; 2021;
2. Arabiourrutia, M.; Lopez, G.; Artetxe, M.; Alvarez, J.; Bilbao, J.; Olazar, M. Waste Tyre Valorization by Catalytic Pyrolysis – A Review. *Renewable and Sustainable Energy Reviews* **2020**, *129*, 109932, doi:10.1016/j.rser.2020.109932.
3. Okoye, C.O.; Jones, I.; Zhu, M.; Zhang, Z.; Zhang, D. Manufacturing of Carbon Black from Spent Tyre Pyrolysis Oil – A Literature Review. *J Clean Prod* **2021**, *279*, 123336, doi:10.1016/j.jclepro.2020.123336.
4. Saleh, T.A.; Gupta, V.K. Processing Methods, Characteristics and Adsorption Behavior of Tire Derived Carbons: A Review. *Adv Colloid Interface Sci* **2014**, *211*, 93–101, doi:10.1016/J.CIS.2014.06.006.
5. Sudame, A.M.; Ugale, M.; Raut, E.R.; Kapgate, B. Adsorbent from Waste Tires as Activated Carbon for Removal of Heavy Metals from Waste Water-A Review. *J Phys Conf Ser* **2021**, *1913*, 012088, doi:10.1088/1742-6596/1913/1/012088.
6. Oboirien, B.O.; North, B.C. A Review of Waste Tyre Gasification. *J Environ Chem Eng* **2017**, *5*, 5169–5178, doi:10.1016/J.JECE.2017.09.057.
7. Jones, I.; Zhu, M.; Zhang, J.; Zhang, Z.; Preciado-Hernandez, J.; Gao, J.; Zhang, D. The Application of Spent Tyre Activated Carbons as Low-Cost Environmental Pollution Adsorbents: A Technical Review. *J Clean Prod* 2021, *312*.
8. Zhang, J.; Jones, I.; Zhu, M.; Zhang, Z.; Preciado-Hernandez, J.; Zhang, D. Pore Development During CO2 and Steam Activation of a Spent Tyre Pyrolysis Char. *Waste Biomass Valorization* **2021**, *12*, 2097–2108, doi:10.1007/s12649-020-01165-4.
9. Danish, M.; Ahmad, T. A Review on Utilization of Wood Biomass as a Sustainable Precursor for Activated Carbon Production and Application. *Renewable and Sustainable Energy Reviews* **2018**, *87*, 1–21, doi:10.1016/j.rser.2018.02.003.
10. Yahya, M.A.; Al-Qodah, Z.; Ngah, C.W.Z. Agricultural Bio-Waste Materials as Potential Sustainable Precursors Used for Activated Carbon Production: A Review. *Renewable and Sustainable Energy Reviews* **2015**, *46*, 218–235, doi:10.1016/j.rser.2015.02.051.

11. Ioannidou, O.; Zabaniotou, A. Agricultural Residues as Precursors for Activated Carbon Production-A Review. *Renewable and Sustainable Energy Reviews* **2007**, *11*, 1966–2005, doi:10.1016/j.rser.2006.03.013.
12. Akhir, M.F.M.; Saad, N.A.; Zakaria, N.A. Potential of Coconut Shell Activated Carbon (CSAC) in Removing Contaminants for Water Quality Improvement: A Critical Review. *AIP Conf Proc* **2017**, *1892*, doi:10.1063/1.5005723.
13. Heidari, A.; Khaki, E.; Younesi, H.; Lu, H.R. Evaluation of Fast and Slow Pyrolysis Methods for Bio-Oil and Activated Carbon Production from Eucalyptus Wastes Using a Life Cycle Assessment Approach. *J Clean Prod* **2019**, *241*, 118394, doi:10.1016/j.jclepro.2019.118394.
14. Godinho, D.; Nogueira, M.; Bernardo, M.; Dias, D.; Lapa, N.; Fonseca, I.; Pinto, F. Recovery of Cr(III) by Using Chars from the Co-Gasification of Agriculture and Forestry Wastes. *Environmental Science and Pollution Research* **2019**, doi:10.1007/s11356-019-05609-w.
15. European Commission *Study on the Review of the List of Critical Raw Materials*; 2017;
16. Nogueira; Matos; Bernardo; Pinto; Lapa; Surra; Fonseca Char from Spent Tire Rubber: A Potential Adsorbent of Remazol Yellow Dye. *C — Journal of Carbon Research* **2019**, *5*, 76, doi:10.3390/c5040076.
17. Thompson, K.A.; Shimabuku, K.K.; Kearns, J.P.; Knappe, D.R.U.; Summers, R.S.; Cook, S.M. Environmental Comparison of Biochar and Activated Carbon for Tertiary Wastewater Treatment. *Environ Sci Technol* **2016**, *50*, 11253–11262, doi:10.1021/acs.est.6b03239.
18. Omodara, L.; Pitkäaho, S.; Turpeinen, E.M.; Saavalainen, P.; Oravisjärvi, K.; Keiski, R.L. Recycling and Substitution of Light Rare Earth Elements, Cerium, Lanthanum, Neodymium, and Praseodymium from End-of-Life Applications - A Review. *J Clean Prod* **2019**, *236*, 117573, doi:10.1016/J.JCLEPRO.2019.07.048.
19. Yang, Y.; Walton, A.; Sheridan, R.; Güth, K.; Gauß, R.; Gutfleisch, O.; Buchert, M.; Steenari, B.M.; Van Gerven, T.; Jones, P.T.; et al. REE Recovery from End-of-Life NdFeB Permanent Magnet Scrap: A Critical Review. *Journal of Sustainable Metallurgy* **2017**, *3*, 122–149, doi:10.1007/s40831-016-0090-4.
20. Rademaker, J.H.; Kleijn, R.; Yang, Y. Recycling as a Strategy against Rare Earth Element Criticality: A Systemic Evaluation of the Potential Yield of NdFeB Magnet Recycling. *Environ Sci Technol* **2013**, *47*, 10129–10136, doi:10.1021/es305007w.
21. Balde, C.P.; Forti, V.; Gray, V.; Kuehr, R.; Stegmann, P. *The Global E-Waste Monitor 2017*; 2017; ISBN 9789280845556.

22. European Commission *Study on the Review of the List of Critical Raw Materials. Non-Critical Raw Materials Factsheets.*; 2017; ISBN 978-92-79-47937-3.
23. Bijina, V.; Jandas, P.J.; Joseph, S.; Gopu, J.; Abhitha, K.; John, H. Recent Trends in Industrial and Academic Developments of Green Tyre Technology. *Polymer Bulletin* 2022.
24. European Commission *Study on the Critical Raw Materials for the EU 2023 – Final Report*; 2023;
25. USA Department of Energy *USA Department of Energy Critical Materials Report - 2023*; 2023;
26. European Commission *Study on the Review of the List of Critical Raw Materials. Non-Critical Raw Materials Factsheets.*; 2017; ISBN 978-92-79-47937-3.
27. Balaram, V. Rare Earth Elements: A Review of Applications, Occurrence, Exploration, Analysis, Recycling, and Environmental Impact. *Geoscience Frontiers* **2019**, *10*, 1285–1303, doi:10.1016/J.GSF.2018.12.005.
28. Cardoso, C.E.D.; Almeida, J.C.; Lopes, C.B.; Trindade, T.; Vale, C.; Pereira, E. Recovery of Rare Earth Elements by Carbon-Based Nanomaterials—a Review. *Nanomaterials* **2019**, *9*, 1–35, doi:10.3390/nano9060814.
29. Binnemans, K.; Jones, P.T.; Blanpain, B.; Van Gerven, T.; Yang, Y.; Walton, A.; Buchert, M. Recycling of Rare Earths: A Critical Review. *J Clean Prod* 2013, *51*, 1–22.
30. Buchert, M. Manhart, A., Bleher, D., Pingel, D. Recycling Critical Raw Materials from Waste Electronic Equipment Commissioned by the North Rhine- Westphalia State Agency for Nature , Environment and Consumer Protection Authors : **2012**, *49*, 30–40.
31. Massari, S.; Ruberti, M. Rare Earth Elements as Critical Raw Materials: Focus on International Markets and Future Strategies. *Resources Policy* **2013**, *38*, 36–43, doi:10.1016/j.resourpol.2012.07.001.
32. Jowitt, S.M.; Werner, T.T.; Weng, Z.; Mudd, G.M. Recycling of the Rare Earth Elements. *Curr Opin Green Sustain Chem* **2018**, *13*, 1–7, doi:10.1016/J.COGSC.2018.02.008.
33. Balaram, V. Potential Future Alternative Resources for Rare Earth Elements: Opportunities and Challenges. *Minerals 2023, Vol. 13, Page 425* **2023**, *13*, 425, doi:10.3390/MIN13030425.
34. European Commission *Critical Raw Materials Resilience: Charting a Path towards Greater Security and Sustainability*; 2021;
35. Jin, H.; Afiuny, P.; Dove, S.; Furlan, G.; Zakotnik, M.; Yih, Y.; Sutherland, J.W. Life Cycle Assessment of Neodymium-Iron-Boron Magnet-to-Magnet Recycling for Electric Vehicle Motors. *Environ Sci Technol* **2018**, *52*, 3796–3802, doi:10.1021/acs.est.7b05442.

36. Prakash, V.; Sun, Z.H.I.; Sietsma, J.; Yang, Y. Electrochemical Recovery of Rare Earth Elements From Magnet Scraps - a Theoretical Analysis. *European Rare Earth Resources Conference* **2014**, 163–170.
37. Panayotova, M.; Panayotov, V. REVIEW OF METHODS FOR THE RARE EARTH METALS RECYCLING Marinela Panayotova , Vladko Panayotov Introduction - Rare Earth Elements Criticality. *Annual of the University of Mining and Geology, "St Ivan Rilski"* **2012**, *55*, 142–147.
38. Nogueira, M.; Matos, I.; Bernardo, M.; Tarelho, L.A.C.; Ferraria, A.M.; Botelho do Rego, A.M.; Fonseca, I.; Lapa, N. Recovery of Rare Earth Elements (Nd3+ and Dy3+) by Using Carbon-Based Adsorbents from Spent Tire Rubber. *Waste Management* **2024**, *174*, 451–461, doi:10.1016/J.WASMAN.2023.12.025.
39. Iftekhar, S.; Heidari, G.; Amanat, N.; Zare, E.N.; Asif, M.B.; Hassanpour, M.; Lehto, V.P.; Sillanpaa, M. Porous Materials for the Recovery of Rare Earth Elements, Platinum Group Metals, and Other Valuable Metals: A Review. *Environmental Chemistry Letters 2022 20:6* **2022**, *20*, 3697–3746, doi:10.1007/S10311-022-01486-X.
40. Arena, N.; Lee, J.; Clift, R. Life Cycle Assessment of Activated Carbon Production from Coconut Shells. *J Clean Prod* **2016**, *125*, 68–77, doi:10.1016/j.jclepro.2016.03.073.
41. Kumar Mishra, R.; Singh, B.; Acharya, B. A Comprehensive Review on Activated Carbon from Pyrolysis of Lignocellulosic Biomass: An Application for Energy and the Environment. *Carbon Resources Conversion* **2024**, *7*, 100228, doi:10.1016/J.CRCON.2024.100228.
42. Heidarinejad, Z.; Dehghani, M.H.; Heidari, M.; Javedan, G.; Ali, I.; Sillanpää, M. Methods for Preparation and Activation of Activated Carbon: A Review. *Environmental Chemistry Letters 2020 18:2* **2020**, *18*, 393–415, doi:10.1007/S10311-019-00955-0.
43. Kumar, A.; Saini, K.; Bhaskar, T. Hydochar and Biochar: Production, Physicochemical Properties and Techno-Economic Analysis. *Bioresour Technol* **2020**, *310*, 123442, doi:10.1016/J.BIORTECH.2020.123442.
44. Wang, K.; Remón, J.; Jiang, Z.; Ding, W. Recent Advances in the Preparation and Application of Biochar Derived from Lignocellulosic Biomass: A Mini Review. *Polymers 2024, Vol. 16, Page 851* **2024**, *16*, 851, doi:10.3390/POLYM16060851.
45. Perreault, L.L.; Giret, S.; Gagnon, M.; Florek, J.; Larivière, D.; Kleitz, F. Functionalization of Mesoporous Carbon Materials for Selective Separation of Lanthanides under Acidic Conditions. *ACS Appl Mater Interfaces* **2017**, *9*, 12003–12012, doi:10.1021/ACSAMI.6B16650/ASSET/IMAGES/LARGE/AM-2016-16650Z_0012.JPEG.

46. Marwani, H.M.; Albishri, H.M.; Jalal, T.A.; Soliman, E.M. Study of Isotherm and Kinetic Models of Lanthanum Adsorption on Activated Carbon Loaded with Recently Synthesized Schiff's Base. *Arabian Journal of Chemistry* **2017**, *10*, S1032–S1040, doi:10.1016/J.ARABJC.2013.01.008.
47. Gad, H.M.H.; Awwad, N.S. Factors Affecting on the Sorption/Desorption of Eu (III) Using Activated Carbon. *Sep Sci Technol* **2007**, *42*, 3657–3680, doi:10.1080/01496390701626495.
48. Anastopoulos, I.; Bhatnagar, A.; Lima, E.C. Adsorption of Rare Earth Metals: A Review of Recent Literature. *J Mol Liq* **2016**, *221*, 954–962, doi:10.1016/j.molliq.2016.06.076.
49. Asadollahzadeh, M.; Torkaman, R.; Torab-Mostaedi, M. Extraction and Separation of Rare Earth Elements by Adsorption Approaches: Current Status and Future Trends. *Separation & Purification Reviews* **2021**, 1–28, doi:10.1080/15422119.2020.1792930.
50. Saha, D.; Akkoyunlu, S.D.; Thorpe, R.; Hensley, D.K.; Chen, J. Adsorptive Recovery of Neodymium and Dysprosium in Phosphorous Functionalized Nanoporous Carbon. *J Environ Chem Eng* **2017**, *5*, 4684–4692, doi:10.1016/j.jece.2017.09.009.
51. Alcaraz, L.; Escudero, M.E.; Alguacil, F.J.; Llorente, I.; Urbieta, A.; Fernández, P.; López, F.A. Dysprosium Removal Fromwater Using Active Carbons Obtained from Spent Coffee Ground. *Nanomaterials* **2019**, *9*, doi:10.3390/nano9101372.
52. Qadeer, R. Adsorption of Neodymium Ions on Activated Charcoal from Aqeous Solutions. *J Radioanal Nucl Chem* **2005**, *265*, 377–381, doi:10.1007/s10967-005-0836-0.
53. Zheng, X.; Zhang, Y.; Bian, T.; Zhang, Y.; Li, Z.; Pan, J. Oxidized Carbon Materials Cooperative Construct Ionic Imprinted Cellulose Nanocrystals Films for Efficient Adsorption of Dy(III). *Chemical Engineering Journal* **2020**, *381*, 122669, doi:10.1016/j.cej.2019.122669.
54. Komnitsas, K.; Zaharaki, D.; Bartzas, G.; Alevizos, G. Adsorption of Scandium and Neodymium on Biochar Derived after Low-Temperature Pyrolysis of Sawdust. *Minerals* **2017**, *7*, 200, doi:10.3390/min7100200.
55. Smith, Y.R.; Bhattacharyya, D.; Willhard, T.; Misra, M. Adsorption of Aqueous Rare Earth Elements Using Carbon Black Derived from Recycled Tires. *Chemical Engineering Journal* **2016**, *296*, 102–111, doi:10.1016/j.cej.2016.03.082.
56. Babu, C.M.; Binnemans, K.; Roosen, J. Ethylenediaminetriacetic Acid-Functionalized Activated Carbon for the Adsorption of Rare Earths from Aqueous Solutions. *Ind Eng Chem Res* **2018**, *57*, 1487–1497, doi:10.1021/acs.iecr.7b04274.
57. Chen, S.; Xiao, M.; Lu, D.; Zhan, X. Carbon Nanofibers as Solid-Phase Extraction Adsorbent for the Preconcentration of Trace Rare Earth Elements and Their

Determination by Inductively Coupled Plasma Mass Spectrometry. *Anal Lett* **2007**, *40*, 2105–2115, doi:10.1080/00032710701567113.

58. Ramasamy, D.L.; Puhakka, V.; Doshi, B.; Iftekhar, S.; Sillanpää, M. Fabrication of Carbon Nanotubes Reinforced Silica Composites with Improved Rare Earth Elements Adsorption Performance. *Chemical Engineering Journal* **2019**, *365*, 291–304, doi:10.1016/J.CEJ.2019.02.057.
59. Haggag, E.S.A.; Embaby, M.A.; El-Sheikh, A.S.; Fathy, N.A.; El-Kady, A.A. High Efficiency Simultaneous Adsorption of Rare Earth Elements from Aqueous Solutions Using Carbon Xerogel-Chitosan Composite. *Int J Environ Anal Chem* **2024**, doi:10.1080/03067319.2024.2324064.
60. Younis, A.M.; Kolesnikov, A. V.; Desyatov, A. V. Efficient Removal of La(III) and Nd(III) from Aqueous Solutions Using Carbon Nanoparticles. *Am J Analyt Chem* **2014**, *05*, 1273–1284, doi:10.4236/AJAC.2014.517133.
61. EL-Masry, E.H.; Ibrahim, H.A.; Abdel Moamen, O.A.; Zaher, W.F. Sorption of Some Rare Earth Elements from Aqueous Solutions Using Copolymer/Activated Carbon Composite: Multivariate Optimization Approach. *Advanced Powder Technology* **2022**, *33*, 103467, doi:10.1016/J.APT.2022.103467.
62. Kano, N.; Pang, M.; Deng, Y.; Imaizumi, H. Adsorption of Rare Earth Elements (REEs) onto Activated Carbon Modified with Potassium Permanganate (KMnO 4). *Journal of Applied Solution Chemistry and Modeling* **2017**, *6*, 51–61.
63. Gismondi, P.; Kuzmin, A.; Unsworth, C.; Rangan, S.; Khalid, S.; Saha, D. Understanding the Adsorption of Rare-Earth Elements in Oligo-Grafted Mesoporous Carbon. *Langmuir* **2022**, *38*, 203–210, doi:10.1021/ACS.LANGMUIR.1C02403/ASSET/IMAGES/LARGE/LA1C02403_0009.JPEG.
64. Sun, Y.; Wang, Q.; Chen, C.; Tan, X.; Wang, X. Interaction between Eu(III) and Graphene Oxide Nanosheets Investigated by Batch and Extended X-Ray Absorption Fine Structure Spectroscopy and by Modeling Techniques. *Environ Sci Technol* **2012**, *46*, 6020–6027, doi:10.1021/ES300720F/SUPPL_FILE/ES300720F_SI_001.PDF.
65. Kilian, K.; Pyrzyńska, K.; Pęgier, M. Comparative Study of Sc(III) Sorption onto Carbon-Based Materials. *Solvent Extraction and Ion Exchange* **2017**, *35*, 450–459, doi:10.1080/07366299.2017.1354580.
66. Saha, D.; Bhasin, V.; Khalid, S.; Smeriglio, N.; Cuka, S.; Bhattacharyya, D.; Rodgers, J.; Panja, P.; Deo, M.; Apple, T. Adsorption of Rare Earth Elements in Carboxylated Mesoporous Carbon. *Sep Purif Technol* **2023**, *314*, 123583, doi:10.1016/J.SEPPUR.2023.123583.

67. Pinheiro, R.F.; Grimm, A.; Oliveira, M.L.S.; Vieillard, J.; Silva, L.F.O.; De Brum, I.A.S.; Lima, É.C.; Naushad, M.; Sellaoui, L.; Dotto, G.L.; et al. Adsorptive Behavior of the Rare Earth Elements Ce and La on a Soybean Pod Derived Activated Carbon: Application in Synthetic Solutions, Real Leachate and Mechanistic Insights by Statistical Physics Modeling. *Chemical Engineering Journal* **2023**, *471*, 144484, doi:10.1016/J.CEJ.2023.144484.
68. dos Reis, G.S.; Schnorr, C.E.; Dotto, G.L.; Vieillard, J.; Netto, M.S.; Silva, L.F.O.; De Brum, I.A.S.; Thyrel, M.; Lima, É.C.; Lassi, U. Wood Waste-Based Functionalized Natural Hydrochar for the Effective Removal of Ce(III) Ions from Aqueous Solution. *Environmental Science and Pollution Research* **2023**, *30*, 64067–64077, doi:10.1007/S11356-023-26921-6/FIGURES/8.
69. He, Q.; Chen, J.; Gan, L.; Gao, M.; Zan, M.; Xiao, Y. Insight into Leaching of Rare Earth and Aluminum from Ion Adsorption Type Rare Earth Ore: Adsorption and Desorption. *Journal of Rare Earths* **2023**, *41*, 1398–1407, doi:10.1016/J.JRE.2022.08.009.
70. Yang, X.; Wan, Y.; Zheng, Y.; He, F.; Yu, Z.; Huang, J.; Wang, H.; Ok, Y.S.; Jiang, Y.; Gao, B. Surface Functional Groups of Carbon-Based Adsorbents and Their Roles in the Removal of Heavy Metals from Aqueous Solutions: A Critical Review. *Chemical Engineering Journal* **2019**, *366*, 608–621, doi:10.1016/J.CEJ.2019.02.119.
71. Raninga, M.; Mudgal, A.; Patel, V.K.; Patel, J.; Kumar Sinha, M. Modification of Activated Carbon-Based Adsorbent for Removal of Industrial Dyes and Heavy Metals: A Review. *Mater Today Proc* **2023**, *77*, 286–294, doi:10.1016/J.MATPR.2022.11.358.
72. Goswami, L.; Kushwaha, A.; Kafle, S.R.; Kim, B.S. Surface Modification of Biochar for Dye Removal from Wastewater. *Catalysts 2022, Vol. 12, Page 817* **2022**, *12*, 817, doi:10.3390/CATAL12080817.
73. Badsha, M.A.H.; Khan, M.; Wu, B.; Kumar, A.; Lo, I.M.C. Role of Surface Functional Groups of Hydrogels in Metal Adsorption: From Performance to Mechanism. *J Hazard Mater* **2021**, *408*, 124463, doi:10.1016/J.JHAZMAT.2020.124463.
74. Miloudi, W.A.; Oukebdane, K.; Abderrahim, O. Hyper-Branched Phosphonated Polyethyleneimine Composite for the Removal of Samarium(III) Ions from Aqueous Solutions: Effect of Process Parameters. *Desalination Water Treat* **2023**, *303*, 181–192, doi:10.5004/DWT.2023.29761.
75. Wang, J. Adsorption of Aqueous Neodymium, Europium, Gadolinium, Terbium, and Yttrium Ions onto NZVI-Montmorillonite: Kinetics, Thermodynamic Mechanism, and the Influence of Coexisting Ions. *Environmental Science and Pollution Research* **2018**, *25*, 33521–33537, doi:10.1007/S11356-018-3296-0/FIGURES/11.

76. Sazali, N.; Harun, Z.; Sazali, N. A Review on Batch and Column Adsorption of Various Adsorbent Towards the Removal of Heavy Metal. *Journal of Advanced Research in Fluid Mechanics and Thermal Sciences Journal homepage* **2020**, *67*, 66–88.
77. Malbenia John, M.; Benettayeb, A.; Belkacem, M.; Ruvimbo Mitchel, C.; Hadj Brahim, M.; Benettayeb, I.; Haddou, B.; Al-Farraj, S.; Alkahtane, A.A.; Ghosh, S.; et al. An Overview on the Key Advantages and Limitations of Batch and Dynamic Modes of Biosorption of Metal Ions. *Chemosphere* **2024**, *357*, 142051, doi:10.1016/J.CHEMOSPHERE.2024.142051.
78. Brandani, S. Kinetics of Liquid Phase Batch Adsorption Experiments. *Adsorption* **2021**, *27*, 353–368, doi:10.1007/S10450-020-00258-9/FIGURES/11.
79. Patel, H.; In, C. Comparison of Batch and Fixed Bed Column Adsorption: A Critical Review. *International Journal of Environmental Science and Technology 2021 19:10* **2021**, *19*, 10409–10426, doi:10.1007/S13762-021-03492-Y.
80. Patel, H. Fixed-Bed Column Adsorption Study: A Comprehensive Review. *Applied Water Science 2019 9:3* **2019**, *9*, 1–17, doi:10.1007/S13201-019-0927-7.
81. Myers, T.G.; Cabrera-Codony, A.; Valverde, A. On the Development of a Consistent Mathematical Model for Adsorption in a Packed Column (and Why Standard Models Fail). *Int J Heat Mass Transf* **2023**, *202*, 123660, doi:10.1016/J.IJHEATMASSTRANSFER.2022.123660.
82. Foo, K.Y.; Hameed, B.H. Insights into the Modeling of Adsorption Isotherm Systems. *Chemical Engineering Journal* **2010**, *156*, 2–10, doi:10.1016/j.cej.2009.09.013.
83. Chen, X.; Hossain, M.F.; Duan, C.; Lu, J.; Tsang, Y.F.; Islam, M.S.; Zhou, Y. Isotherm Models for Adsorption of Heavy Metals from Water - A Review. *Chemosphere* **2022**, *307*, 135545, doi:10.1016/J.CHEMOSPHERE.2022.135545.
84. Musah, M.; Azeh, Y.; Mathew, J.; Umar, M.; Abdulhamid, Z.; Muhammad, A. Adsorption Kinetics and Isotherm Models: A Review. *Caliphate Journal of Science and Technology* **2022**, *4*, 20–26, doi:10.4314/CAJOST.V4I1.3.
85. Al-Ghouti, M.A.; Da'ana, D.A. Guidelines for the Use and Interpretation of Adsorption Isotherm Models: A Review. *J Hazard Mater* **2020**, *393*, 122383, doi:10.1016/J.JHAZMAT.2020.122383.
86. Qiu, H.; Lv, L.; Pan, B.; Zhang, Q.; Zhang, W.; Zhang, Q. Critical Review in Adsorption Kinetic Models. *Journal of Zhejiang University SCIENCE A* **2009**, *10*, 716–724, doi:10.1631/jzus.A0820524.
87. Revellame, E.D.; Fortela, D.L.; Sharp, W.; Hernandez, R.; Zappi, M.E. Adsorption Kinetic Modeling Using Pseudo-First Order and Pseudo-Second Order Rate Laws: A Review. *Clean Eng Technol* **2020**, *1*, 100032, doi:10.1016/J.CLET.2020.100032.

88. Wang, J.; Guo, X. Adsorption Kinetic Models: Physical Meanings, Applications, and Solving Methods. *J Hazard Mater* **2020**, *390*, 122156, doi:10.1016/J.JHAZMAT.2020.122156.
89. Langmuir, I. The Constitution and Fundamental Properties of Solids and Liquids. II. Liquids. *J Am Chem Soc* **1917**, *39*, 1848–1906, doi:10.1021/JA02254A006/ASSET/JA02254A006.FP.PNG_V03.
90. Freundlich, H. Über Die Adsorption in Lösungen. *Zeitschrift für Physikalische Chemie* **1907**, *57U*, 385–470, doi:10.1515/ZPCH-1907-5723.
91. De Vargas Brião, G.; Ali, M.; Khim, H.&; Chu, H.; Hashim, A.; Chu, K.H. The Sips Isotherm Equation: Often Used and Sometimes Misused. *Sep Sci Technol* **2023**, *58*, 884–892, doi:10.1080/01496395.2023.2167662.
92. Tseng, R.L.; Wu, F.C.; Juang, R.S. Characteristics and Applications of the Lagergren's First-Order Equation for Adsorption Kinetics. *J Taiwan Inst Chem Eng* **2010**, *41*, 661–669, doi:10.1016/J.JTICE.2010.01.014.
93. Ho, Y.S. Review of Second-Order Models for Adsorption Systems. *J Hazard Mater* **2006**, *136*, 681–689, doi:10.1016/J.JHAZMAT.2005.12.043.
94. Tseng, R.L.; Tran, H.N.; Juang, R.S. Revisiting Temperature Effect on the Kinetics of Liquid–Phase Adsorption by the Elovich Equation: A Simple Tool for Checking Data Reliability. *J Taiwan Inst Chem Eng* **2022**, *136*, 104403, doi:10.1016/J.JTICE.2022.104403.
95. Debord, J.; Harel, M.; Bollinger, J.C.; Chu, K.H. The Elovich Isotherm Equation: Back to the Roots and New Developments. *Chem Eng Sci* **2022**, *262*, 118012, doi:10.1016/J.CES.2022.118012.
96. Obradovic, B. Guidelines for General Adsorption Kinetics Modeling. *Hem. Ind* **2020**, *74*, 65–70, doi:10.2298/HEMIND200201006O.
97. WeberJr., W.J.; Morris, J.C. Kinetics of Adsorption on Carbon from Solution. *Journal of the Sanitary Engineering Division* **1963**, *89*, 31–59, doi:10.1061/JSEDAI.0000430.
98. Shirzad, K.; Viney, C. A Critical Review on Applications of the Avrami Equation beyond Materials Science. *J R Soc Interface* **2023**, *20*, doi:10.1098/RSIF.2023.0242.
99. Whitaker, S.; González-López, M.E.; Laureano-Anzaldo, C.M.; Pérez-Fonseca, A.A.; Arellano, M.; Robledo-Ortíz, J.R. A Discussion on Linear and Non-Linear Forms of Thomas Equation for Fixed-Bed Adsorption Column Modeling Discusión Sobre Las Formas Lineal y No-Lineal Del Modelo de Thomas Para El Modelado de Curvas de Ruptura. **2021**, *20*, 875–884, doi:10.24275/rmiq/Fen2337.
100. Thomas, H.C. Heterogeneous Ion Exchange in a Flowing System. *J Am Chem Soc* **1944**, *66*, 1664–1666, doi:10.1021/JA01238A017/ASSET/JA01238A017.FP.PNG_V03.

101. Chu, K.H.; Hashim, M.A. Comparing Different Versions of the Yoon–Nelson Model in Describing Organic Micropollutant Adsorption within Fixed Bed Adsorbers. *Environmental Science and Pollution Research* **2024**, *31*, 21136–21143, doi:10.1007/S11356-024-32450-7/FIGURES/5.
102. Yoon, Y.H.; Nelson, J.H. Application of Gas Adsorption Kinetics I. A Theoretical Model for Respirator Cartridge Service Life. *Am Ind Hyg Assoc J* **1984**, *45*, 509–516, doi:10.1080/15298668491400197.
103. Chu, K.H. Breakthrough Curve Analysis by Simplistic Models of Fixed Bed Adsorption: In Defense of the Century-Old Bohart-Adams Model. *Chemical Engineering Journal* **2020**, *380*, 122513, doi:10.1016/J.CEJ.2019.122513.
104. Bohart, G.S.; Adams, E.Q. Some Aspects of the Behavior of Charcoal with Respect to Chlorine. *J Am Chem Soc* **1920**, *42*, 523–544, doi:10.1021/JA01448A018/ASSET/JA01448A018.FP.PNG_V03.
105. Wang, J.; Guo, X. Adsorption Isotherm Models: Classification, Physical Meaning, Application and Solving Method. *Chemosphere* **2020**, *258*, 127279, doi:10.1016/J.CHEMOSPHERE.2020.127279.
106. Shan, X. quan; Lian, J.; Wen, B. Effect of Organic Acids on Adsorption and Desorption of Rare Earth Elements. *Chemosphere* **2002**, *47*, 701–710, doi:10.1016/S0045-6535(02)00032-2.
107. Gao, W.; Wen, D.; Ho, J.C.; Qu, Y. Incorporation of Rare Earth Elements with Transition Metal–Based Materials for Electrocatalysis: A Review for Recent Progress. *Mater Today Chem* **2019**, *12*, 266–281, doi:10.1016/J.MTCHEM.2019.02.002.
108. Liang, Z.; Yin, L.; Yin, H.; Yin, Z.; Du, Y. Rare Earth Element Based Single-Atom Catalysts: Synthesis, Characterization and Applications in Photo/Electro-Catalytic Reactions. *Nanoscale Horiz* **2021**, *7*, 31–40, doi:10.1039/D1NH00459J.
109. Gong, Z.; Wang, J.; Zhang, K.; Li, B.; Wu, W. Complex Rare-Earth Oxides Leached from the Rare-Earth Concentrate to Prepare the Catalyst for Selective Catalytic Reduction of NO with NH3. *Miner Eng* **2020**, *146*, 106135, doi:10.1016/J.MINENG.2019.106135.
110. El-Khouly, S.M.; Mohamed, G.M.; Fathy, N.A.; Fagal, G.A. Effect of Nanosized CeO2 or ZnO Loading on Adsorption and Catalytic Properties of Activated Carbon. *Adsorption Science and Technology* **2017**, *35*, 774–788, doi:10.1177/0263617417698704/ASSET/IMAGES/LARGE/10.1177_0263617417698704-FIG8.JPEG.
111. Chu, T.; Xie, M.; Yang, D.; Ming, P.; Li, B.; Zhang, C. Highly Active and Durable Carbon Support Pt-Rare Earth Catalyst for Proton Exchange Membrane Fuel Cell. *Int J Hydrogen Energy* **2020**, *45*, 27291–27298, doi:10.1016/J.IJHYDENE.2020.07.134.

112. Yu, Y.; Yu, L.; Koh, K.Y.; Wang, C.; Chen, J.P. Rare-Earth Metal Based Adsorbents for Effective Removal of Arsenic from Water: A Critical Review. *Crit Rev Environ Sci Technol* **2018**, *48*, 1127–1164, doi:10.1080/10643389.2018.1514930.
113. Yu, Y.; Zhang, C.; Yang, L.; Paul Chen, J. Cerium Oxide Modified Activated Carbon as an Efficient and Effective Adsorbent for Rapid Uptake of Arsenate and Arsenite: Material Development and Study of Performance and Mechanisms. *Chemical Engineering Journal* **2017**, *315*, 630–638, doi:10.1016/J.CEJ.2016.09.068.
114. Chowdhury, N.A.; Deng, S.; Jin, H.; Prodius, D.; Sutherland, J.W.; Nlebedim, I.C. Sustainable Recycling of Rare-Earth Elements from NdFeB Magnet Swarf: Techno-Economic and Environmental Perspectives. *ACS Sustain Chem Eng* **2021**, *9*, 15915–15924, doi:10.1021/ACSSUSCHEMENG.1C05965/ASSET/IMAGES/LARGE/SC1C05965_0005.JPEG.
115. Jha, M.K.; Kumari, A.; Panda, R.; Rajesh Kumar, J.; Yoo, K.; Lee, J.Y. Review on Hydrometallurgical Recovery of Rare Earth Metals. *Hydrometallurgy* **2016**, *165*, 2–26, doi:10.1016/J.HYDROMET.2016.01.035.
116. Lopes, J.L.; Martins, M.J.; Nogueira, H.I.S.; Estrada, A.C.; Trindade, T. Carbon-Based Heterogeneous Photocatalysts for Water Cleaning Technologies: A Review. *Environmental Chemistry Letters 2021 19:1* **2021**, *19*, 643–668, doi:10.1007/S10311-020-01092-9.
117. Cao, S.; Yu, J. Carbon-Based H2-Production Photocatalytic Materials. *Journal of Photochemistry and Photobiology C: Photochemistry Reviews* **2016**, *27*, 72–99, doi:10.1016/J.JPHOTOCHEMREV.2016.04.002.
118. Khan, M.E. State-of-the-Art Developments in Carbon-Based Metal Nanocomposites as a Catalyst: Photocatalysis. *Nanoscale Adv* **2021**, *3*, 1887–1900, doi:10.1039/D1NA00041A.
119. An, J.; Qu, Y.; Wang, G. The Multiple Roles of Rare Earth Elements in the Field of Photocatalysis. *Inorg Chem Front* **2023**, *11*, 11–28, doi:10.1039/D3QI02006A.
120. Khan, H.; Lofland, S.E.; Ramanujachary, K. V.; Alhokbany, N.; Ahmad, T. Bifunctional Multiferroic GdCrO3 Nanoassemblies for Sustainable H2 Production Using Electro- and Photocatalysis. *ACS Appl Energy Mater* **2023**, *6*, 8102–8110, doi:10.1021/ACSAEM.3C01210/SUPPL_FILE/AE3C01210_SI_001.PDF.
121. Yan, Z.; Yin, K.; Xu, M.; Fang, N.; Yu, W.; Chu, Y.; Shu, S. Photocatalysis for Synergistic Water Remediation and H2 Production: A Review. *Chemical Engineering Journal* **2023**, *472*, 145066, doi:10.1016/J.CEJ.2023.145066.
122. Shi, Z.J.; Ma, M.G.; Zhu, J.F. Recent Development of Photocatalysts Containing Carbon Species: A Review. *Catalysts 2019, Vol. 9, Page 20* **2018**, *9*, 20, doi:10.3390/CATAL9010020.

123. Kandy, M.M. Carbon-Based Photocatalysts for Enhanced Photocatalytic Reduction of CO2 to Solar Fuels. *Sustain Energy Fuels* **2020**, *4*, 469–484, doi:10.1039/C9SE00827F.
124. Ge, J.; Zhang, Y.; Park, S.J. Recent Advances in Carbonaceous Photocatalysts with Enhanced Photocatalytic Performances: A Mini Review. *Materials 2019, Vol. 12, Page 1916* **2019**, *12*, 1916, doi:10.3390/MA12121916.
125. Mehtab, A.; Ahmed, J.; Alshehri, S.M.; Mao, Y.; Ahmad, T. Rare Earth Doped Metal Oxide Nanoparticles for Photocatalysis: A Perspective. *Nanotechnology* **2022**, *33*, 142001, doi:10.1088/1361-6528/AC43E7.
126. Saqib, N. us; Adnan, R.; Shah, I. A Mini-Review on Rare Earth Metal-Doped TiO2for Photocatalytic Remediation of Wastewater. *Environmental Science and Pollution Research* **2016**, *23*, 15941–15951, doi:10.1007/S11356-016-6984-7/TABLES/2.
127. Kumaravel, V.; Imam, M.D.; Badreldin, A.; Chava, R.K.; Do, J.Y.; Kang, M.; Abdel-Wahab, A. Photocatalytic Hydrogen Production: Role of Sacrificial Reagents on the Activity of Oxide, Carbon, and Sulfide Catalysts. *Catalysts 2019, Vol. 9, Page 276* **2019**, *9*, 276, doi:10.3390/CATAL9030276.
128. Zhang, T.; Lu, S. Sacrificial Agents for Photocatalytic Hydrogen Production: Effects, Cost, and Development. *Chem Catalysis* **2022**, *2*, 1502–1505, doi:10.1016/j.checat.2022.06.023.
129. Godinho, D.; Dias, D.; Bernardo, M.; Lapa, N.; Fonseca, I.; Lopes, H.; Pinto, F. Adding Value to Gasification and Co-Pyrolysis Chars as Removal Agents of Cr3+. *J Hazard Mater* **2017**, *321*, 173–182, doi:10.1016/j.jhazmat.2016.09.006.
130. Mui, E.L.K.; Ko, D.C.K.; McKay, G. Production of Active Carbons from Waste Tyres––a Review. *Carbon N Y* **2004**, *42*, 2789–2805, doi:10.1016/J.CARBON.2004.06.023.
131. Miranda, M.; Cabrita, I.; Pinto, F.; Gulyurtlu, I. Mixtures of Rubber Tyre and Plastic Wastes Pyrolysis: A Kinetic Study. *Energy* **2013**, *58*, 270–282, doi:10.1016/j.energy.2013.06.033.
132. Miranda, M.; Pinto, F.; Gulyurtlu, I.; Cabrita, I. Pyrolysis of Rubber Tyre Wastes: A Kinetic Study. *Fuel* **2013**, *103*, 542–552, doi:10.1016/j.fuel.2012.06.114.
133. Pinto, F.; Paradela, F.; Gulyurtlu, I.; Ramos, A.M. Prediction of Liquid Yields from the Pyrolysis of Waste Mixtures Using Response Surface Methodology. *Fuel Processing Technology* **2013**, *116*, 271–283, doi:10.1016/j.fuproc.2013.07.012.
134. Ju, J.; Wang, H.; Xing, X.; Liu, M.; Zhao, G.; Jiang, X. Occurrence Form of Potassium Vapor in Sinter and Its Effect on Reduction Degradation Indexes. *Metals 2023, Vol. 13, Page 1010* **2023**, *13*, 1010, doi:10.3390/MET13061010.

135. Li, K.; Zhang, J.; Liu, Z.; Ning, X.; Wang, T. Gasification of Graphite and Coke in Carbon–Carbon Dioxide–Sodium or Potassium Carbonate Systems. *Ind Eng Chem Res* **2014**, *53*, 5737–5748, doi:10.1021/IE4039955.
136. European Committee for Standardization EN 15290 - Solid Biofuels - Determination of Major Elements - Al, Ca, Fe, Mg, P, K, Si, Na and Ti 2011.
137. Dias, D.; Lapa, N.; Bernardo, M.; Ribeiro, W.; Matos, I.; Fonseca, I.; Pinto, F. Cr(III) Removal from Synthetic and Industrial Wastewaters by Using Co-Gasification Chars of Rice Waste Streams. *Bioresour Technol* **2018**, *266*, 139–150, doi:10.1016/j.biortech.2018.06.054.
138. Rego, R.; Ferraria, A.M.; Botelho do Rego, A.M.; Oliveira, M.C. Development of PdP Nano Electrocatalysts for Oxygen Reduction Reaction. *Electrochim Acta* **2013**, *87*, 73–81, doi:10.1016/j.electacta.2012.08.107.
139. Ferraria, A.M.; Carapeto, A.P.; Botelho do Rego, A.M. X-Ray Photoelectron Spectroscopy: Silver Salts Revisited. *Vacuum* **2012**, *86*, 1988–1991, doi:10.1016/j.vacuum.2012.05.031.
140. Beamson, G.; D. Briggs *High Resolution XPS of Organic Polymers: The Scienta ESCA300 Database.*; Wiley, Ed.; Wiley: Chichester, UK, 1992; ISBN 0-471-93592-1.
141. Sprecher, B.; Kleijn, R.; Kramer, G.J. Recycling Potential of Neodymium: The Case of Computer Hard Disk Drives. *Environ Sci Technol* **2014**, *48*, 9506–9513, doi:10.1021/es501572z.
142. München, D.D.; Veit, H.M. Neodymium as the Main Feature of Permanent Magnets from Hard Disk Drives (HDDs). *Waste Management* 2017, *61*, 372–376.
143. Zhang, Y.; Gu, F.; Su, Z.; Liu, S.; Anderson, C.; Jiang, T. Hydrometallurgical Recovery of Rare Earth Elements from Ndfeb Permanent Magnet Scrap: A Review. *Metals (Basel)* 2020, *10*, 1–34.
144. Kumari, A.; Sinha, M.K.; Pramanik, S.; Sahu, S.K. Recovery of Rare Earths from Spent NdFeB Magnets of Wind Turbine: Leaching and Kinetic Aspects. *Waste Management* **2018**, *75*, 486–498, doi:10.1016/j.wasman.2018.01.033.
145. Padhan, E.; Nayak, A.K.; Sarangi, K. Recovery of Neodymium and Dysprosium from NdFeB Magnet Swarf. *Hydrometallurgy* **2017**, *174*, 210–215, doi:10.1016/j.hydromet.2017.10.015.
146. Vander Hoogerstraete, T.; Blanpain, B.; Van Gerven, T.; Binnemans, K. From NdFeB Magnets towards the Rare-Earth Oxides: A Recycling Process Consuming Only Oxalic Acid. *RSC Adv* **2014**, *4*, 64099–64111, doi:10.1039/c4ra13787f.
147. Walton, A.; Yi, H.; Rowson, N.A.; Speight, J.D.; Mann, V.S.J.; Sheridan, R.S.; Bradshaw, A.; Harris, I.R.; Williams, A.J. The Use of Hydrogen to Separate and Recycle

Neodymium-Iron-Boron-Type Magnets from Electronic Waste. *J Clean Prod* **2015**, *104*, 236–241, doi:10.1016/j.jclepro.2015.05.033.

148. Yamada, E.; Murakami, H.; Nishihama, S.; Yoshizuka, K. Separation Process of Dysprosium and Neodymium from Waste Neodymium Magnet. *Sep Purif Technol* **2018**, *192*, 62–68, doi:10.1016/j.seppur.2017.09.062.
149. Behera, S.S.; Panda, S.K.; Mandal, D.; Parhi, P.K. Ultrasound and Microwave Assisted Leaching of Neodymium from Waste Magnet Using Organic Solvent. *Hydrometallurgy* **2019**, *185*, 61–70, doi:10.1016/j.hydromet.2019.02.003.
150. Retegan, T.; Ravaux, C.; Gergoric, M.; Espegren, F.; Steenari, B.-M. Leaching and Recovery of Rare-Earth Elements from Neodymium Magnet Waste Using Organic Acids. *Metals (Basel)* **2018**, *8*, 721, doi:10.3390/met8090721.
151. Ni'am, A.C.; Wang, Y.F.; Chen, S.W.; You, S.J. Recovery of Rare Earth Elements from Waste Permanent Magnet (WPMs) via Selective Leaching Using the Taguchi Method. *J Taiwan Inst Chem Eng* **2019**, 1–9, doi:10.1016/j.jtice.2019.01.006.
152. El-Maghrabi, H.H.; Barhoum, A.; Nada, A.A.; Moustafa, Y.M.; Seliman, S.M.; Youssef, A.M.; Bechelany, M. Synthesis of Mesoporous Core-Shell CdS@TiO2 (0D and 1D) Photocatalysts for Solar-Driven Hydrogen Fuel Production. *J Photochem Photobiol A Chem* **2018**, *351*, 261–270, doi:10.1016/J.JPHOTOCHEM.2017.10.048.
153. Cui, H.; Li, B.; Zhang, Y.; Zheng, X.; Li, X.; Li, Z.; Xu, S. Constructing Z-Scheme Based CoWO4/CdS Photocatalysts with Enhanced Dye Degradation and H2 Generation Performance. *Int J Hydrogen Energy* **2018**, *43*, 18242–18252, doi:10.1016/J.IJHYDENE.2018.08.050.
154. Corredor, J.; Rivero, M.J.; Rangel, C.M.; Gloaguen, F.; Ortiz, I. Comprehensive Review and Future Perspectives on the Photocatalytic Hydrogen Production. *Journal of Chemical Technology & Biotechnology* **2019**, *94*, 3049–3063, doi:10.1002/JCTB.6123.
155. Antoniadou, M.; Daskalaki, V.M.; Balis, N.; Kondarides, D.I.; Kordulis, C.; Lianos, P. Photocatalysis and Photoelectrocatalysis Using (CdS-ZnS)/TiO2 Combined Photocatalysts. *Appl Catal B* **2011**, *107*, 188–196, doi:10.1016/J.APCATB.2011.07.013.
156. Xing, R.; Tong, L.; Liu, X.; Ren, Y.; Liu, B.; Ochiai, T.; Feng, C.; Chong, R.; Liu, S. CdS/ZnS Heterostructured Porous Composite with Enhanced Visible Light Photocatalysis. *J Nanosci Nanotechnol* **2018**, *18*, 6913–6918, doi:10.1166/JNN.2018.15523.
157. Qutub, N.; Pirzada, B.M.; Umar, K.; Mehraj, O.; Muneer, M.; Sabir, S. Synthesis, Characterization and Visible-Light Driven Photocatalysis by Differently Structured CdS/ZnS Sandwich and Core–Shell Nanocomposites. *Physica E Low Dimens Syst Nanostruct* **2015**, *74*, 74–86, doi:10.1016/J.PHYSE.2015.06.023.

158. Nadikatla, S.K.; Chintada, V.B.; Gurugubelli, T.R.; Koutavarapu, R. Review of Recent Developments in the Fabrication of ZnO/CdS Heterostructure Photocatalysts for Degradation of Organic Pollutants and Hydrogen Production. *Molecules 2023, Vol. 28, Page 4277* **2023**, *28*, 4277, doi:10.3390/MOLECULES28114277.
159. Koca, A.; Sahin, M. Photocatalytic Hydrogen Production by Direct Sunlight: A Laboratory Experiment. *J Chem Educ* **2003**, *80*, 1314–1315, doi:10.1021/ED080P1314.
160. A New Sensitive Chemical Actinometer - II. Potassium Ferrioxalate as a Standard Chemical Actinometer. *Proc R Soc Lond A Math Phys Sci* **1956**, *235*, 518–536, doi:10.1098/RSPA.1956.0102.
161. Kumaravel, V.; Mathew, S.; Bartlett, J.; Pillai, S.C. Photocatalytic Hydrogen Production Using Metal Doped TiO2: A Review of Recent Advances. *Appl Catal B* **2019**, *244*, 1021–1064, doi:10.1016/J.APCATB.2018.11.080.
162. Boshagh, F.; Rostami, K.; van Niel, E.W.J. Application of Kinetic Models in Dark Fermentative Hydrogen Production–A Critical Review. *Int J Hydrogen Energy* **2022**, *47*, 21952–21968, doi:10.1016/J.IJHYDENE.2022.05.031.
163. Clarizia, L.; Somma, I. Di; Onotri, L.; Andreozzi, R.; Marotta, R. Kinetic Modeling of Hydrogen Generation over Nano-Cu(s)/TiO2 Catalyst through Photoreforming of Alcohols. *Catal Today* **2017**, *281*, 117–123, doi:10.1016/J.CATTOD.2016.05.053.
164. Somma, I. Di; Clarizia, L.; Russo, D.; Andreozzi, R.; Marotta, R. Hydrogen Evolution over Nano-Cu/TiO2 Catalyst through Photoreforming of Alcohols: A Kinetic Investigation.
165. Peterson, A.; Wilson, W.; Mukherjee, B.; (Ravi) Subramanian, V. Simultaneous Photodegradation and Hydrogen Production with TiO2/Pt/CdS Using UV–Visible Light in the Presence of a Sacrificial Agent and a Pollutant. **2014**, 153–171, doi:10.1007/978-1-4939-1628-3_8.
166. Balgude, S.D.; Sethi, Y.A.; Kale, B.B.; Munirathnam, N.R.; Amalnerkar, D.P.; Adhyapak, P. V. Nanostructured Layered Sn3O4 for Hydrogen Production and Dye Degradation under Sunlight. *RSC Adv* **2016**, *6*, 95663–95669, doi:10.1039/C6RA20058C.
167. Rowhani, A.; Rainey, T. Scrap Tyre Management Pathways and Their Use as a Fuel—A Review. *Energies (Basel)* **2016**, *9*, 888, doi:10.3390/en9110888.
168. dos Santos, R.G.; Rocha, C.L.; Felipe, F.L.S.; Cezario, F.T.; Correia, P.J.; Rezaei-Gomari, S. Tire Waste Management: An Overview from Chemical Compounding to the Pyrolysis-Derived Fuels. *J Mater Cycles Waste Manag* **2020**, *22*, 628–641, doi:10.1007/S10163-020-00986-8/TABLES/7.

169. Nisar, J.; Ali, G.; Ullah, N.; Awan, I.A.; Iqbal, M.; Shah, A.; Sirajuddin; Sayed, M.; Mahmood, T.; Khan, M.S. Pyrolysis of Waste Tire Rubber: Influence of Temperature on Pyrolysates Yield. *J Environ Chem Eng* **2018**, *6*, 3469–3473, doi:10.1016/j.jece.2018.05.021.
170. Costa, S.M.R.; Fowler, D.; Carreira, G.A.; Portugal, I.; Silva, C.M. Production and Upgrading of Recovered Carbon Black from the Pyrolysis of End-of-Life Tires. *Materials* **2022**, *15*, 2030, doi:10.3390/ma15062030.
171. Cardona, N.; Campuzano, F.; Betancur, M.; Jaramillo, L.; Martínez, J.D. Possibilities of Carbon Black Recovery from Waste Tyre Pyrolysis to Be Used as Additive in Rubber Goods -a Review-. *IOP Conf Ser Mater Sci Eng* **2018**, *437*, 012012, doi:10.1088/1757-899X/437/1/012012.
172. Yu, J.; Xu, J.; Li, Z.; He, W.; Huang, J.; Xu, J.; Li, G. Upgrading Pyrolytic Carbon-Blacks (CBp) from End-of-Life Tires: Characteristics and Modification Methodologies. *Front Environ Sci Eng* **2020**, *14*, 19, doi:10.1007/s11783-019-1198-0.
173. Doja, S.; Pillari, L.K.; Bichler, L. Processing and Activation of Tire-Derived Char: A Review. *Renewable and Sustainable Energy Reviews* **2022**, *155*, 111860, doi:10.1016/j.rser.2021.111860.
174. Thommes, M.; Kaneko, K.; Neimark, A. V.; Olivier, J.P.; Rodriguez-Reinoso, F.; Rouquerol, J.; Sing, K.S.W. Physisorption of Gases, with Special Reference to the Evaluation of Surface Area and Pore Size Distribution (IUPAC Technical Report). *Pure and Applied Chemistry* **2015**, *87*, 1051–1069, doi:10.1515/pac-2014-1117.
175. Seng-eiad, S.; Jitkarnka, S. Untreated and HNO3-Treated Pyrolysis Char as Catalysts for Pyrolysis of Waste Tire: In-Depth Analysis of Tire-Derived Products and Char Characterization. *J Anal Appl Pyrolysis* **2016**, *122*, 151–159, doi:10.1016/j.jaap.2016.10.004.
176. López, F.A.; Centeno, T.A.; Rodríguez, O.; Alguacil, F.J. Preparation and Characterization of Activated Carbon from the Char Produced in the Thermolysis of Granulated Scrap Tyres. *J Air Waste Manage Assoc* **2013**, *63*, 534–544, doi:10.1080/10962247.2013.763870.
177. López, F.A.; Centeno, T.A.; Alguacil, F.J.; Lobato, B.; López-Delgado, A.; Fermoso, J. Gasification of the Char Derived from Distillation of Granulated Scrap Tyres. *Waste Management* **2012**, *32*, 743–752, doi:10.1016/j.wasman.2011.08.006.
178. Lewis, A.; Guéguen, C. Using Chemometric Models to Predict the Biosorption of Low Levels of Dysprosium by Euglena Gracilis. *Environmental Science and Pollution Research* **2022**, *29*, 58936–58949, doi:10.1007/S11356-022-19918-0/TABLES/4.

179. Ahmed, I.; Bhattacharjee, S.; Lee, C.-S.; Kang, K.-K.; Ahn, J.-W.; Ahn, W.-S. Aqueous Nd3+ Capture Using a Carboxyl-Functionalized Porous Carbon Derived from ZIF-8. *J Colloid Interface Sci* **2021**, *594*, 702–712, doi:10.1016/j.jcis.2021.03.036.
180. Tan, K.L.; Hameed, B.H. Insight into the Adsorption Kinetics Models for the Removal of Contaminants from Aqueous Solutions. *J Taiwan Inst Chem Eng* **2017**, *74*, 25–48, doi:10.1016/j.jtice.2017.01.024.
181. Hubbe, M.; Azizian, S.; Douven, S. Implications of Apparent Pseudo-Second-Order Adsorption Kinetics onto Cellulosic Materials: A Review. *Bioresources* **2019**, *14*, 7582–7626, doi:10.15376/biores.14.3.7582-7626.
182. Vareda, J.P. On Validity, Physical Meaning, Mechanism Insights and Regression of Adsorption Kinetic Models. *J Mol Liq* **2023**, *376*, 121416, doi:10.1016/j.molliq.2023.121416.
183. Martínez, J.D.; Cardona-Uribe, N.; Murillo, R.; García, T.; López, J.M. Carbon Black Recovery from Waste Tire Pyrolysis by Demineralization: Production and Application in Rubber Compounding. *Waste Management* **2019**, *85*, 574–584, doi:10.1016/j.wasman.2019.01.016.
184. Alcaraz, L.; Escudero, M.E.; Alguacil, F.J.; Llorente, I.; Urbieta, A.; Fernández, P.; López, F.A. Dysprosium Removal from Water Using Active Carbons Obtained from Spent Coffee Ground. *Nanomaterials* **2019**, *9*, 1372, doi:10.3390/nano9101372.
185. Smith, Y.R.; Bhattacharyya, D.; Willhard, T.; Misra, M. Adsorption of Aqueous Rare Earth Elements Using Carbon Black Derived from Recycled Tires. *Chemical Engineering Journal* **2016**, *296*, 102–111, doi:10.1016/j.cej.2016.03.082.
186. Komnitsas, K.; Zaharaki, D.; Bartzas, G.; Alevizos, G. Adsorption of Scandium and Neodymium on Biochar Derived after Low-Temperature Pyrolysis of Sawdust. *Minerals* **2017**, *7*, 200, doi:10.3390/min7100200.
187. Bundaleska, N.; Henriques, J.; Abrashev, M.; Botelho do Rego, A.M.; Ferraria, A.M.; Almeida, A.; Dias, F.M.; Valcheva, E.; Arnaudov, B.; Upadhyay, K.K.; et al. Large-Scale Synthesis of Free-Standing N-Doped Graphene Using Microwave Plasma. *Sci Rep* **2018**, *8*, 12595, doi:10.1038/s41598-018-30870-3.
188. Naumkin, A. V.; Kraut-Vass, A.; Stephen W. Gaarenstroom, C.J.P. NIST X-Ray Photoelectron Spectroscopy Database Available online: https://srdata.nist.gov/xps/ (accessed on 28 November 2022).
189. Baltrus, J.P.; Keller, M.J. Rare Earth Oxides Eu2O3 and Nd2O3 Analyzed by XPS. *Surface Science Spectra* **2019**, *26*, 014001, doi:10.1116/1.5085768.

190. Mefoued, A. Neodymium-Coated PECVD-Designed Silicon Nanostructures: A Comprehensive Structural, Morphological and Spectroscopic Investigation. **2022**, doi:10.21203/RS.3.RS-1902627/V1.
191. Aide, M.T.; Aide, C. Rare Earth Elements: Their Importance in Understanding Soil Genesis. *ISRN Soil Science* **2012**, *2012*, 1–11, doi:10.5402/2012/783876.
192. Doja, S.; Pillari, L.K.; Bichler, L. Processing and Activation of Tire-Derived Char: A Review. *Renewable and Sustainable Energy Reviews* **2022**, *155*, 111860, doi:10.1016/J.RSER.2021.111860.
193. Hofman, M.; Pietrzak, R. Adsorbents Obtained from Waste Tires for NO2 Removal under Dry Conditions at Room Temperature. *Chemical Engineering Journal* **2011**, *170*, 202–208, doi:10.1016/J.CEJ.2011.03.054.
194. Costa, S.M.R.; Fowler, D.; Carreira, G.A.; Portugal, I.; Silva, C.M. Production and Upgrading of Recovered Carbon Black from the Pyrolysis of End-of-Life Tires. *Materials* 2022, *15*.
195. Formela, K. Sustainable Development of Waste Tires Recycling Technologies – Recent Advances, Challenges and Future Trends. *Advanced Industrial and Engineering Polymer Research* **2021**, *4*, 209–222, doi:10.1016/J.AIEPR.2021.06.004.
196. Thommes, M.; Kaneko, K.; Neimark, A. V.; Olivier, J.P.; Rodriguez-Reinoso, F.; Rouquerol, J.; Sing, K.S.W. Physisorption of Gases, with Special Reference to the Evaluation of Surface Area and Pore Size Distribution (IUPAC Technical Report). *Pure and Applied Chemistry* **2015**, *87*, 1051–1069, doi:10.1515/pac-2014-1117.
197. Preciado-Hernandez, J.; Zhang, J.; Jones, I.; Zhu, M.; Zhang, Z.; Zhang, D. An Experimental Study of Gasification Kinetics during Steam Activation of a Spent Tyre Pyrolysis Char. *J Environ Chem Eng* **2021**, *9*, doi:10.1016/j.jece.2021.105306.
198. Zhang, J.; Zhu, M.; Jones, I.; Okoye, C.O.; Zhang, Z.; Zhang, D. The Transformation and Fate of Sulphur during CO2gasification of a Spent Tyre Pyrolysis Char. In Proceedings of the Proceedings of the Combustion Institute; Elsevier Ltd, 2021; Vol. 38, pp. 3891–3898.
199. Jones, I.; Preciado-Hernandez, J.; Zhu, M.; Zhang, J.; Zhang, Z.; Zhang, D. Utilisation of Spent Tyre Pyrolysis Char as Activated Carbon Feedstock: The Role, Transformation and Fate of Zn. *Waste Management* **2021**, *126*, 549–558, doi:10.1016/j.wasman.2021.03.031.
200. Zhang, J.; Jones, I.; Zhu, M.; Zhang, Z.; Preciado-Hernandez, J.; Zhang, D. Pore Development During CO2 and Steam Activation of a Spent Tyre Pyrolysis Char. *Waste Biomass Valorization* **2021**, *12*, 2097–2108, doi:10.1007/s12649-020-01165-4.

201. Weibel, D.; Jovanovic, Z.R.; Gálvez, E.; Steinfeld, A. Mechanism of Zn Particle Oxidation by H2O and CO2 in the Presence of ZnO. *Chemistry of Materials* **2014**, *26*, 6486–6495, doi:10.1021/cm503064f.
202. Akcil, A.; Ibrahim, Y.A.; Meshram, P.; Panda, S.; Abhilash Hydrometallurgical Recycling Strategies for Recovery of Rare Earth Elements from Consumer Electronic Scraps: A Review. *Journal of Chemical Technology & Biotechnology* **2021**, *96*, 1785–1797, doi:10.1002/JCTB.6739.
203. Espinosa, R.; Bertuol, D.A.; Barbosa, A.; Junior, B.; Efstratiadis, V.S.; Michailidis, N. Sustainable Recovery, Recycle of Critical Metals and Rare Earth Elements from Waste Electric and Electronic Equipment (Circuits, Solar, Wind) and Their Reusability in Additive Manufacturing Applications: A Review. *Metals 2022, Vol. 12, Page 794* **2022**, *12*, 794, doi:10.3390/MET12050794.
204. Faur-Brasquet, C.; Kadirvelu, K.; Le Cloirec, P. Removal of Metal Ions from Aqueous Solution by Adsorption onto Activated Carbon Cloths: Adsorption Competition with Organic Matter. *Carbon N Y* **2002**, *40*, 2387–2392, doi:10.1016/S0008-6223(02)00117-3.
205. Park, H.J.; Tavlarides, L.L. Adsorption of Neodymium(III) from Aqueous Solutions Using a Phosphorus Functionalized Adsorbent. *Ind Eng Chem Res* **2010**, *49*, 12567–12575, doi:10.1021/IE100403B.
206. Demey, H.; Lapo, B.; Ruiz, M.; Fortuny, A.; Marchand, M.; Sastre, A.M. Neodymium Recovery by Chitosan/Iron(III) Hydroxide [ChiFer(III)] Sorbent Material: Batch and Column Systems. *Polymers 2018, Vol. 10, Page 204* **2018**, *10*, 204, doi:10.3390/POLYM10020204.
207. Renu; Sithole, T. A Review on Regeneration of Adsorbent and Recovery of Metals: Adsorbent Disposal and Regeneration Mechanism. *S Afr J Chem Eng* **2024**, *50*, 39–50, doi:10.1016/J.SAJCE.2024.07.006.
208. Gupta, N.K.; Gupta, A. 2D and 3D Carbon-Based Adsorbents for an Efficient Removal of HgII Ions: A Review. *FlatChem* **2018**, *11*, 1–14, doi:10.1016/J.FLATC.2018.11.002.
209. Nogueira, M.; Bernardo, M.; Ventura, M.; Matos, I.; Pinto, F.; Lapa, N. Opportunities and Constraints of the Adsorption of Rare Earth Elements onto Pyrolytic Carbon-Based Materials: A Mini-Review. *Processes 2024, Vol. 12, Page 2257* **2024**, *12*, 2257, doi:10.3390/PR12102257.
210. Yang, Q.; Yu, L.; Zhao, X.; Wang, Y.; Zhu, H.; Zhang, Y. Highly Stable γ-NiOOH/ZnCdS Photocatalyst for Efficient Hydrogen Evolution. *Int J Hydrogen Energy* **2022**, *47*, 27516–27526, doi:10.1016/J.IJHYDENE.2022.06.093.
211. Dong, J.; Fang, W.; Yuan, H.; Xia, W.; Zeng, X.; Shangguan, W. Few-Layered MoS2/ZnCdS/ZnS Heterostructures with an Enhanced Photocatalytic Hydrogen

Evolution. *ACS Appl Energy Mater* **2022**, *5*, 4893–4902, doi:10.1021/ACSAEM.2C00301/ASSET/IMAGES/LARGE/AE2C00301_0011.JPEG.

212. Song, L.; Zhang, S.; Liu, D.; Sun, S.; Wei, J. High-Performance Hydrogen Evolution of NiB/ZnCdS under Visible Light Irradiation. *Int J Hydrogen Energy* **2020**, *45*, 8234–8242, doi:10.1016/J.IJHYDENE.2020.01.029.
213. Lee, G.J.; Wu, J.J. Recent Developments in ZnS Photocatalysts from Synthesis to Photocatalytic Applications — A Review. *Powder Technol* **2017**, *318*, 8–22, doi:10.1016/J.POWTEC.2017.05.022.
214. Bernardo, M.; Lapa, N.; Pinto, F.; Nogueira, M.; Matos, I.; Ventura, M.; Ferraria, A.M.; do Rego, A.M.B.; Fonseca, I.M. Valorisation of Spent Tire Rubber as Carbon Adsorbents for Pb(II) and W(VI) in the Framework of a Circular Economy. *Environmental Science and Pollution Research* **2023**, *30*, 74820–74837, doi:10.1007/S11356-023-27689-5/FIGURES/12.
215. Kheira, Z.; Mayouf, S.; Bennabi, S.; Fadia, M.; Cherifa, M.D. The Study of the Photocatalytic Degradation of Orange II Dye with Wastewater Using New Pyrochlore Solid Solutions Bi1.5Sb1.5Zn1–XCuxO7 as Photocatalysts. *Journal of Water Chemistry and Technology 2024 46:5* **2024**, *46*, 436–448, doi:10.3103/S1063455X24050114.
216. Rani, M.; Murtaza, M.; Amjad, A.; Zahra, M.; Waseem, A.; Alhodaib, A. NiSe2/Ag3PO4 Nanocomposites for Enhanced Visible Light Photocatalysts for Environmental Remediation Applications. *Catalysts 2023, Vol. 13, Page 929* **2023**, *13*, 929, doi:10.3390/CATAL13060929.
217. Deymeh, F.; Ahmadpour, A.; Allahresani, A.; Arami-Niya, A. Collaborative Adsorption and Photocatalytic Degradation of High Concentration Pharmaceutical Pollutants in Water Using a Novel Dendritic Fibrous Nano-Silica Modified with Chitosan and UiO-66. *Int J Biol Macromol* **2024**, *275*, 133534, doi:10.1016/J.IJBIOMAC.2024.133534.

2024

Miguel Filipe da Costa Nogueira

TYRE4REECYCLE - RECOVERY OF RARE EARTH ELEMENTS FROM NDFEB MAGNETS BY USING POROUS CARBONS PRODUCED FROM RUBBER OF SPENT TYRES